



HAL
open science

Quantum-classical hybrid algorithms for quantum many-body physics

Pauline Besserve

► **To cite this version:**

Pauline Besserve. Quantum-classical hybrid algorithms for quantum many-body physics. Strongly Correlated Electrons [cond-mat.str-el]. Institut Polytechnique de Paris, 2023. English. NNT : 2023IP-PAX086 . tel-04639453

HAL Id: tel-04639453

<https://theses.hal.science/tel-04639453v1>

Submitted on 9 Jul 2024

HAL is a multi-disciplinary open access archive for the deposit and dissemination of scientific research documents, whether they are published or not. The documents may come from teaching and research institutions in France or abroad, or from public or private research centers.

L'archive ouverte pluridisciplinaire **HAL**, est destinée au dépôt et à la diffusion de documents scientifiques de niveau recherche, publiés ou non, émanant des établissements d'enseignement et de recherche français ou étrangers, des laboratoires publics ou privés.



INSTITUT
POLYTECHNIQUE
DE PARIS

NNT : 2023IPPAX086

Thèse de doctorat



Hybrid quantum-classical algorithms for the quantum many-body problem

Thèse de doctorat de l'Institut Polytechnique de Paris
préparée à Ecole Polytechnique

École doctorale n°626 Institut Polytechnique de Paris (EDIPP)
Spécialité de doctorat : Physique

Thèse présentée et soutenue à Paris, le 06/10/2023, par

PAULINE BESSERVE

Composition du Jury :

Laurent Sanchez-Palencia Directeur de recherche, Centre de Physique Théorique, Palaiseau	Président
Serge Florens Directeur de recherche, Institut Néel (CNRS/UGA), Grenoble	Rapporteur
Ivan Rungger <i>Senior Research Scientist</i> , National Physical Laboratory, Teddington	Rapporteur
Sophia Economou Professeure, Virginia Tech, Blacksburg	Examinatrice
Michel Ferrero Chargé de recherche, Centre de Physique Théorique, Palaiseau	Co-directeur de thèse
Thomas Ayrat Ingénieur de recherche, Eviden Quantum Laboratory, Les Clayes-sous-Bois	Co-directeur de thèse

Abstract

Strongly-correlated materials feature electronic phases with high potential for application, such as high-temperature superconductivity. Nevertheless, these systems are notoriously difficult to describe, as they escape standard mean-field methods.

This thesis investigates the possibility to leverage noisy quantum computation within the flagship algorithm for strong correlations, the dynamical mean-field theory (DMFT). It aims to take advantage of the first quantum computing devices, despite their imperfections imputable to a still-limited degree of experimental control. Firstly, an improved version of the variational method for preparing the ground state of the impurity model is proposed. It consists in carrying out updates of the single-particle basis in which the impurity Hamiltonian is described. These updates are interwoven with variational optimizations of the state, and guided by the one-particle density matrix of the current optimized variational state. This algorithm has enabled us to carry out the first noisy hybrid implementation of a DMFT-like scheme with a two-impurity auxiliary system. Also, we show on several examples that this method is capable of increasing the ability of a given variational circuit to represent the target state. Finally, we propose to combine single-particle basis updates with an adaptive variational algorithm, which builds the circuit iteratively. We show that this approach can reduce the number of gates in the circuit for a given precision in the energy of the attained state.

Secondly, we propose to take advantage of the dissipation affecting the qubits to alleviate the effect of bath truncation onto the fit of the DMFT hybridization. We confirm that a reduction in the count of bath sites is within the reach of such a method. However, we make the assumption of a dissipative process which is not realistic: the method therefore still needs to be studied via a model closer to experimental conditions.

Résumé

Les matériaux à fortes corrélations présentent des phases électroniques à haut potentiel applicatif, telles que la supraconductivité à haute température critique. Néanmoins, ces systèmes sont notoirement difficiles à décrire car ils échappent aux méthodes de champ moyen standard.

Cette thèse étudie l'apport du calcul quantique bruité pour l'algorithme phare des fortes corrélations, la théorie du champ moyen dynamique (DMFT). Elle vise à mettre à profit les premiers dispositifs de calcul quantique, malgré leurs imperfections liées à un degré de contrôle expérimental encore limité.

Dans un premier temps, une version améliorée de la méthode variationnelle de préparation de l'état fondamental du modèle d'impureté est proposée. Elle consiste en la réalisation de mises à jour de la base à une particule dans laquelle est décrit le Hamiltonien d'impureté. Ces mises à jour sont entrelacées avec des optimisations variationnelles de l'état, et guidées par la matrice densité à une particule de l'état variationnel optimisé courant. Cet algorithme nous a permis de réaliser la première implémentation hybride bruitée d'un schéma assimilé à la DMFT avec un système auxiliaire à deux impuretés. Aussi, nous montrons sur plusieurs exemples que cette méthode est capable d'augmenter la capacité d'un circuit variationnel donné à représenter l'état cible. Enfin, nous proposons de combiner les mises à jour de la base à une particule avec un algorithme variationnel dit adaptatif, qui construit le circuit itérativement. Nous montrons que cette approche permet de réduire, à précision donnée sur l'énergie de l'état optimisé, le nombre de portes du circuit.

Dans un second temps, nous proposons de mettre à profit la dissipation qui impacte les qubits afin de diminuer les effets de la troncation du bain sur l'ajustement de l'hybridation du bain à celle de la DMFT. Nous montrons qu'une réduction en termes de sites de bain est bien à portée d'une telle méthode. Cependant, nous faisons l'hypothèse d'un processus dissipatif qui n'est pas réaliste: la méthode doit donc encore être étudiée via un modèle plus proche des conditions expérimentales.

Résumé substantiel

Cette thèse porte sur l'étude des matériaux à fortes corrélations électroniques, modélisés par le modèle de Fermi-Hubbard, par le biais d'une implémentation hybride de l'algorithme de la théorie du champ moyen dynamique (DMFT). Cette théorie consiste à trouver itérativement une représentation sous forme de modèle dit d'impureté de l'instance de modèle de Hubbard considérée. Contrairement au modèle de Hubbard, qui décrit un réseau de sites tous porteurs de corrélation, le modèle d'impureté consiste en deux types de sites ; un petit nombre de sites corrélés et un nombre supposément infini de sites dits de bain, sans interaction, avec lesquels les sites corrélés s'hybrident. En dehors de certains cas limite, cette représentation offre une description de la physique du matériau considéré limitée par le nombre de sites d'impuretés et par le nombre de sites de bain. Alors, la levée de cette limitation par des moyens de calcul classiques nécessite un nombre exponentiel de ressources en l'un ou les deux de ces nombres, selon le solveur d'impureté mis en œuvre. Or, des méthodes basées sur le calcul sur machines quantiques ont été proposées pour lever cette barrière exponentielle, si bien que l'étude des matériaux corrélés, ainsi que de manière connexe la chimie quantique, sont considérés comme des candidats parmi les plus prometteurs à une avancée significative apportée par un ordinateur quantique. Cependant, il n'existe pour le moment pas d'ordinateur quantique, mais seulement des prototypes à petit nombre d'unités de calcul – appelées qubits – sur lesquels peuvent être réalisés des calculs dits bruités, en ce qu'ils sont fortement affectés par la décohérence, laquelle efface le caractère quantique des qubits.

L'objectif de cette thèse est d'évaluer l'apport du calcul quantique bruité dans une implémentation hybride de la DMFT, où seule une portion de l'algorithme est déléguée à un petit prototype d'ordinateur quantique imparfait. Les résultats de cette thèse sont basés sur l'émulation classique du comportement bruité de la portion quantique de l'implémentation de la DMFT. Il est choisi de se focaliser sur un modèle de bruit spécifique, le modèle dépolarisant, qui rend compte de l'effet multiplicatif sur le taux d'erreur du nombre d'opérations appliquées au registre quantique et correspond au bruit intrinsèque, et ce dans des proportions importantes, en vigueur dans les prototypes actuels. Des propositions sont faites d'une part pour être en mesure d'augmenter le nombre de sites d'impuretés, et d'autre part, pour limiter les effets de troncation du bain inhérents au faible nombre de qubits dans l'approche traditionnelle de la DMFT hybride.

Dans un premier temps, l'implémentation de la DMFT basée sur la préparation d'état par méthode variationnelle sur ordinateur quantique (Variational Quantum Eigensolver – VQE) est considérée. Dans l'état de l'art antérieur, seule la DMFT à deux sites, un site d'impureté et un site de bain – soit, avec la dégénérescence en spin, quatre qubits – avait été implémentée avec succès en présence de bruit dans le dispositif quantique. Nous proposons une variante de l'algorithme VQE permettant de considérer deux impuretés et deux sites de bain, impliquant huit qubits. La méthode, inspirée de la chimie quantique, consiste à mettre à profit une base à une particule spécifique, la base d'orbitales naturelles relative à un état quantique donné. Cette base est associée à une compacité maximale de l'état, c'est-à-dire un nombre de déterminants de Slater minimal lorsque l'état est exprimé dans l'espace de Fock sous-tendu par cette base. Nous observons, pour différents types de circuits variationnels, que l'état fondamental du modèle d'impureté peut être approché avec une meilleure précision en termes d'énergie dans sa base d'orbitales naturelles. Néanmoins, ces tests sont basés sur la connaissance de l'état fondamental, qui peut être calculé facilement sur ce petit modèle d'impureté. Nous proposons donc un algorithme itératif (Natural-Orbitalization – NOization) permettant de déterminer et mettre à profit une approximation de la base naturelle de l'état cible pour améliorer les performances de la VQE. Cet algorithme consiste à alterner des étapes de VQE avec des mises à jour de la base à une particule. Plus précisément, après une première étape de VQE, nous effectuons une mise à jour de la base à une particule en faveur de la base d'orbitales naturelles de l'état optimal atteint et répétons le processus. Nous montrons qu'après un petit nombre de mises à jour de la base, de l'ordre de quatre, les performances associées à la base d'orbitales naturelles sont reproduites. Nous testons la méthode sur le modèle de Hubbard à deux et quatre sites à différentes valeurs de corrélation, pour différents circuits variationnels, avec et sans bruit dépolarisant. La méthode est utilisée pour résoudre le modèle d'impureté dans le cadre d'une variante de la DMFT, la méthode du boson esclave rotationnellement invariant (Rotationally Invariant Slave Boson - RISB), qui permet d'obtenir une approximation à basse énergie de la self-énergie en mettant en correspondance via un corrélateur statique le modèle de Hubbard avec un modèle d'impureté dont le nombre de sites de bain est égal au nombre de sites d'impuretés. Cette méthode permet de considérer un modèle à deux impuretés en évitant de devoir effectuer une évolution temporelle sur l'état fondamental, laquelle nécessite des circuits quantiques très profonds, incompatibles avec les niveaux de bruit actuels. Nous mettons en évidence la convergence de la boucle RISB lorsque nous mettons en œuvre la NOization sur un circuit que nous proposons, ainsi qu'une résolution spatiale des effets de corrélation. Ce circuit est constitué d'une routine basée sur la porte de simulation fermionique qui préserve le nombre d'excitations, appliquée sur un état multi-référence. Les performances à faible corrélation sont cependant faibles eu égard de l'intrication limitée des états fondamentaux associés. Nous proposons donc une variante adaptative de la NOization, baptisée Natural-Orbitalizing Adaptive VQE (NOA-VQE), basée non pas sur la VQE mais sur l'algorithme ADAPT-VQE, qui construit le circuit à partir d'un pool d'opérateurs donnés. Nous appliquons cet algorithme au modèle de Hubbard demi-rempli à quatre sites sur un réseau carré à différents niveaux d'interaction,

avec et sans bruit dépolarisant, et observons à précision donnée une diminution de la profondeur de circuit requise.

Dans un second temps, nous considérons le problème de la troncation du bain en adoptant une approche dissipative. Nous considérons un solveur d'impureté basé sur des sites de bains chacun linéairement couplé avec un réservoir markovien de fermions. Nous considérons de mettre à profit des sites de bains dont les fermions peuvent être absorbés (respectivement émis) pour ajuster la partie greater de l'hybridation du modèle d'impureté à celle associée au réseau en interaction dans le cadre de la DMFT (respectivement la partie lesser). Nous montrons sur des hybridations prototypiques à l'équilibre, à différentes valeurs de l'interaction Coulombienne U et à différentes températures inverses β que cette approche fournit de meilleures approximations de l'hybridation que l'approche non dissipative à nombre de sites de bain donné. Cela ouvre la voie à une implémentation hybride de la DMFT qui mettrait à profit la décohérence sur un nombre de qubits intermédiaire pour le bain, et utiliserait un petit nombre de qubits corrigés en erreur pour les impuretés. Cependant, le modèle de bruit considéré ne reflète pas la décohérence à l'œuvre dans les qubits. Nous montrons sur un exemple en utilisant l'encodage de Jordan-Wigner que cette dernière correspond cependant qualitativement à la première, avec une dynamique amortie.

Acknowledgments

First, I would like to thank all the members of my jury panel for having accepted to review my work. Special appreciation is extended to Serge Florens and Ivan Rungger for going through the trouble of a careful reading of this manuscript and pointing out a few misprints that I could correct for the definitive version. It was a pleasure engaging in discussions with all of you during the defense.

Thank you Thomas and Michel for supervising my thesis. I admire you both for your rigor, your insightfulness and your patience. Thomas, your readiness to offer assistance and guidance despite your busy schedule, as well as the opportunities you have provided me with, were genuinely appreciated.

Additionally I would like to express my deepest gratitude to all the passion-driven teachers and researchers who strive to get knowledge in shape and at hand, whether it be through classes, articles, books, or open-source tools.

This thesis journey was significantly enriched by individuals who were integral to my daily life, whether in the lab or the company. Corentin, I am so glad you joined Atos – and my street in Versailles! – during my PhD. I deeply appreciated having you onboard to move forward with the dissipative impurity solving scheme. Maxime R. and Fabrice, we all started as 2019 interns at the Atos Quantum Lab and I am very pleased we were given the possibility to pursue a Cifre PhD with the company. Thank you Cyril for the trust you put in me and in my fabulous co-PhD students. Arthur, it was a pleasure to meet you in or around the Collège de France either over coffee or lunch and I also hope we can continue sharing our viewpoints about interpersonal relationships. Arnaud, I would like to acknowledge your timely dealing with bugs I have been faced with, and your unwavering enthusiasm for afterwork gatherings. Simon, I have always been super impressed by the extent of your knowledge in quantum computing, and pictures of Poupoune never failed to amaze me. Maxime O., I enjoyed seeing your eagerness to learn and try new things, and the way you juggled between playful and deep conversation modes. I will never forget the car conversation we had with Tristan, whose filterless honesty made me laugh more than once. All in all I had many great times with the Atos team, and I leave with my head filled with happy memories with all of you mentioned previously, but also Grigori, Océane, Cyprien... On the lab front, my gratitude goes first to Renaud,

with whom I shared the PhD journey and a desk. Our joint care for the pilea clique brought a touch of life to the office. I also enjoyed the time spent together running across Paris during the Run my City tour. Liam, it was a pleasure to get to know you better at the Jouvence summer school, and to be at the first row to hear your where-does-he-get-that-from random facts. Sid, I will miss the daily wonder of your delicious-looking homemade meals, as well as your wise, curious and benevolent mindset.

Finally, but certainly not least, a heartfelt note to my family and friends. Maman, merci de m'avoir laissée mettre à profit ta curiosité infinie pour satisfaire la mienne et pour tous les instants de perplexité que j'ai pu vivre à parcourir tes grilles de mots croisés sept étoiles. Papa, merci de m'avoir transmis ta philosophie de vie, dans le souci et l'amour des autres et de la nature. À mes trois grandes soeurs, je dois nombre de mes traits de caractère et je les remercie de m'avoir accompagnée dans mon chemin de vie en me soutenant et en me sensibilisant très jeune à l'importance de l'épanouissement professionnel. Mention spéciale à Candice pour m'avoir grandement aidée avec le pot de thèse. Laura, merci pour tous les moments passés ensemble, que ce soit à Lyon, Paris, Bath, Brest, Tokyo ou Edimbourg, et pour ton froncement de sourcils salutaire quand j'ai émis l'idée de ne pas me présenter à l'oral de l'ENS. François, merci pour les fous rires et les discussions parfois complètement loufoques que nous avons partagés, depuis les bancs de l'amphi en M2 jusqu'à aujourd'hui. Por último, Andrés, no puedo agradecer aquí por todo el amor, el apoyo y la alegría que me has dado, ¡pero ya sabes que te amo con todo mi corazón!

List of acronyms, abbreviations and conventions for notation

The following acronyms and abbreviations are thoroughly used in this manuscript:

ARPES: Angle-Resolved Photo-Electronic Spectroscopy
DFT: Density Functional Theory
DMFT: Dynamical Mean-Field Theory
DOS: Density of States
ED: Exact Diagonalization
FLT: Fermi Liquid Theory
fSim: fermionic simulation
GF: Green's function
HEA: Hardware-Efficient Ansatz
JW: Jordan-Wigner
LDCA: Low-Depth Circuit Ansatz
MR: Multi-Reference
MREP: Multi-Reference Excitation-Preserving
NISQ: Noisy Intermediate-Scale Quantum
NO: Natural Orbitals
NOA-VQE: Natural-Orbitalizing Adaptive Variational Quantum Eigensolving
NOization: Natural-Orbitalization
NOizing: Natural-Orbitalizing
QC: Quantum Computer
QM: Quantum Mechanics
RDM: Reduced Density Matrix
RISB: Rotationally-Invariant Slave Boson
VQE: Variational Quantum Eigensolver

Moreover, I have used the following notational conventions:

- Operators do not bear hats to lighten the notation.
- I took the liberty to assimilate a matrix A to its general term A_{ij} .
- ' U ' depending on the context may refer to the Coulomb term in the Hubbard Hamiltonian, a unitary matrix or the evolution operator.

- ' Z ' might stand for the quasiparticle weight or for the partition function.
- i might be a label or the imaginary unit.
- The bitstrings are big-endian.
- 'h.c.' stands for 'hermitian conjugate'.

"Go home now love, leave your wandering. . ."
PJ Harvey, *A noiseless noise*

Contents

Abstract	iii
Résumé	v
Résumé substantiel	ix
Acknowledgments	xii
List of acronyms, abbreviations and conventions for notation	xiv
1 Introduction	1
2 Strongly-correlated systems	3
2.1 Many-fermion systems	3
2.2 When mean-field theory breaks down: strong correlations	5
2.3 A minimal model of strongly-correlated systems: the Hubbard model	7
3 Embedding: Dynamical Mean-Field Theory and alike	11
3.1 What does it mean to solve the Hubbard model?	11
3.2 Probing correlations with single-particle Green's functions	14
3.2.1 Single-particle Green's function as the bridge between theory and experiment	14
3.2.2 Matsubara formalism	15
3.3 DMFT's prescription: going back to a local, atom-like picture	15
3.4 Impurity model	17
3.5 DMFT self-consistency scheme	19
3.6 Impurity solving: methods and limitations	20
3.7 Rotationally-Invariant Slave Boson (RISB) method	22
3.7.1 Theory	22
3.7.2 Slave-boson equations	24
3.7.3 Self-consistent solving of the slave-boson equations	24
4 Computing with noisy quantum devices	27
4.1 The paradigm of quantum computation	28
4.1.1 From the classical bit to qubits	28

4.1.2	Quantum computing paradigms	30
4.1.3	Digital quantum computing: circuits, gates, measurements	31
4.2	Encoding from fermions to qubits	33
4.3	Computing Green's functions with a quantum circuit	34
4.4	Preparing ground states and time-evolving on the chip: main algorithms	36
4.4.1	Variational ground state preparation	36
4.4.2	Trotterization	40
4.5	Quantum noise	40
4.5.1	Quantum channels and Kraus representation	41
4.5.2	Lindblad master equation	44
4.6	Study of the influence of the different noise sources on state preparation	45
4.7	Mitigating errors with the Zero-Noise Extrapolation scheme	47
5	Alleviating the quantum circuit depth burden: Natural-Orbitalization	49
5.1	Single-particle basis representational freedom	50
5.1.1	Single-particle orbitals and associated Fock space	50
5.1.2	Rotation of the modes	50
5.1.3	Natural Orbitals	52
5.1.4	Variational circuit optimization within natural orbitals	55
5.2	Methods	61
5.2.1	Natural-Orbitalization algorithm	61
5.2.2	Natural-Orbitalizing Adaptive Variational Quantum Eigen- solving scheme (NOA-VQE)	66
5.3	Results	67
5.3.1	Natural Orbitalization at work: expressivity enhancement	68
5.3.2	Effect of the Natural-Orbitalization algorithm onto the geom- etry of the single-particle orbitals: an example	70
5.3.3	Natural-Orbitalized two-impurity slave-boson scheme	75
5.3.4	Single-impurity slave-boson scheme	79
5.3.5	Circuit-depth reduction with NOA-VQE	80
5.4	Conclusion	82
6	Leveraging decoherence: dissipative bath approach to impurity solving	83
6.1	Philosophy	83
6.2	Keldysh formalism for out-of-equilibrium many-body systems	84
6.2.1	Keldysh contour	85
6.2.2	Contour-ordered Green's functions	86
6.3	Dissipative bath scheme	89
6.3.1	Steady-state Green's functions in the absence of dissipation	90
6.3.2	Fermionic quantum regression theorem	94
6.3.3	Out-of-equilibrium Green's functions in the presence of linear dissipation	95
6.4	Auxiliary hybridization associated with the dissipative scheme	96
6.5	Hybrid quantum-classical algorithm for DMFT with a dissipative bath	100
6.6	Quality of the fits with the bath size and the strength of dissipation	101
6.7	Influence of the encoding onto the dissipative dynamics	103

6.8 Conclusion	105
7 Conclusion	107
Published work	109
Appendices	111
A Diagonalization of quadratic Hamiltonians	112
B Fourier transform	114
C List of definitions of Green's functions	115
D Equivalence between analyticity in the upper half-plane and causality, Kramers-Kronig relations	117
E Resonant level model	119
F Grassmann variables	122
G Gaussian integral	123
H Tracing out bath degrees of freedom in an action-based representation	124
I Computation of Green's function elements	127
J Proof of the correlation entropy-minimization property of natural orbitals	129
K Specifics of the two-impurity slave-boson scheme	133
L Nature of the qubit pool operators in NOA-VQE	135
M Keldysh contour formalism	137
List of Figures	139
List of Tables	145
Bibliography	159

Introduction

Quantum computing is nowadays a trendy topic, with quantum chemistry and many-body physics ranging amongst the first promising applications to be expected. While the past few years have seen the first claims of a quantum advantage such as the random circuit sampling experiment by Google [1], these achievements were nonetheless not met with practical applications. They were mostly the demonstration of striding advances in terms of quantum hardware quality. In spite of such advances, the domain remains in its infancy, with devices being subject to experimental noise at significant levels. In the end, error-correcting schemes should render quantum computation reliable but require millions of physical qubits to encode a few logical qubits.

Yet, at the start of this thesis back in October 2020, most applications were envisioned considering perfect quantum devices, making the conceivable horizon of practical advantage for the description of many-body compounds particularly remote. Noisy hardware whose access had just started being provided was used to test strategies on minimal systems, but the question of whether these strategies would scale up to tackle larger-size problem instances was open. Still, couldn't the boundaries of computational methods for the study of interacting matter be pushed with mid-term noisy quantum computers? Couldn't we at least lay the grounds for such advances for when better – but still, not perfect – hardware becomes available?

These questions underline the importance of thinking about improving on the software along with the hardware. An illuminating example of the power of algorithmic advances is that of the Wolff algorithm [2] for Monte-Carlo simulation of Ising models in classical computation. The naive Monte-Carlo simulation method relies on the sampling of configurations which get updated with single spin flips. On the other hand, the Wolff algorithm relies on cluster updates. It results in speed-ups of several orders of magnitude, such that it is more advantageous to run the Wolff algorithm on a computer from the 1980s rather than the naive Monte-Carlo update scheme on one of nowadays' supercomputers!

In this vein, this thesis aimed at putting forth improved algorithms for the study of strongly-correlated systems within the quantum-classical implementation of Dy-

namical Mean-Field Theory (DMFT) in the presence of noise in the quantum device.

We begin with some elements of context, defining strongly-correlated systems, the challenges they pose and the DMFT approach to strong correlations. We then give an overview of quantum computing techniques for the many-body problem, and how noise impacts the performances of quantum devices. After that, we present the contributions crafted during this thesis. First, the scope of the usual noisy state preparation algorithm, the Variational Quantum Eigensolver (VQE), is extended by carrying out state-informed single-particle basis updates, which enable to make most of a variational circuit for the task of state preparation. A variation of the proposed algorithm is also devised to provide reduced gate counts. Second, we propose to use noise as a resource for the fit of the DMFT hybridizations. We assess the possibility to reduce, in the presence of noise, the requirements over the count of bath sites in the impurity model of DMFT to properly fit the hybridizations.

Strongly-correlated systems

Strongly-correlated materials, sometimes also referred to as *quantum materials*, are materials whose properties cannot be elucidated if one neglects inter-electronic interactions. Typically, these materials have incompletely filled f or d electron shells and their behaviour is neither metallic nor ionic, as electronic localisation and itinerancy are in competition. For example, many rare earths, transition metal oxides and actinides are strongly correlated materials. Emerging phenomena arising from strong correlations paint a very rich physics, with strong industrial stakes such as high critical-temperature superconductivity. However, after more than half a century of research dedicated to them, they remain notoriously hard to tackle and still pose unsolved mysteries in solid-state physics.

In this chapter, we first introduce many-fermion systems and the challenges associated with their simulation. We then move on to strong correlations in such systems, highlighting how mean-field or even more refined schemes such as the Fermi liquid theory or the Density Functional Theory have a very limited scope in accurately describing correlation effects. Finally, we introduce the 'spherical cow' of correlated materials, the Hubbard model, which will be addressed by embedding schemes such as the Dynamical Mean-Field Theory introduced in a subsequent chapter.

2.1 Many-fermion systems

The starting point of the modelling of electrons in solid-state physics is the *electronic structure Hamiltonian*, also referred to as the *molecular Hamiltonian* in a quantum chemistry context, which describes a system comprising N_a atoms and N_e electrons in the non-relativistic limit as

$$H_{\text{ESH}} = \sum_{m=1}^{N_a} \frac{\hbar^2}{2M_m} \nabla_m^2 + \sum_{i=1}^{N_e} \frac{\hbar^2}{2m_e} \nabla_i^2 - \sum_{i=1}^{N_e} \sum_{m=1}^{N_a} \frac{Z_m e^2}{4\pi\epsilon_0 \|\mathbf{R}_m - \mathbf{r}_i\|} + \frac{1}{2} \sum_{i,j=1}^{N_e} \frac{e^2}{4\pi\epsilon_0 \|\mathbf{r}_j - \mathbf{r}_i\|} + \frac{1}{2} \sum_{m,n=1}^{N_a} \frac{Z_m Z_n e^2}{4\pi\epsilon_0 \|\mathbf{R}_m - \mathbf{R}_n\|}$$

with Z_m the proton content of atom m , M_m its mass, \mathbf{R}_m the position of its nucleus, m_e the mass of an electron and $-e$ its charge. The positions of the electrons are denoted \mathbf{r}_i .

We will make the Born-Oppenheimer approximation and neglect the motion of nuclei, as $M_p \gg m_e$. Consequently, we will only consider the electronic part of the full

electronic structure Hamiltonian of Equation 2.1. Additionally, from now on we will denote by N the number of electrons. Introducing a set of single-particle orbitals ϕ_p , in second quantization the Hamiltonian describing the motion of electrons in the field of fixed nuclei reads:

$$\mathcal{H}_{\text{el.}} = \sum_{p,q} h_{pq} a_p^\dagger a_q + \frac{1}{2} \sum_{p,q,r,s} h_{pqrs} a_p^\dagger a_q^\dagger a_r a_s \quad (2.0)$$

In this expression:

- $h_{pq} = \int d^3r \phi_p^*(\mathbf{r}) \left(-\frac{\nabla^2}{2} - \sum_m \frac{Z_m}{\|\mathbf{R}_m - \mathbf{r}\|} \right) \phi_q(\mathbf{r})$ is the one-electron overlap integral
- $h_{pqrs} = \int d^3r_1 d^3r_2 \frac{\phi_p^*(\mathbf{r}_1) \phi_q^*(\mathbf{r}_2) \phi_r(\mathbf{r}_1) \phi_s(\mathbf{r}_2)}{\|\mathbf{r}_1 - \mathbf{r}_2\|}$ is the two-electron overlap integral
- a_p^\dagger (resp. a_p) is the creation (resp. annihilation) operator associated to fermionic mode p . Such operators obey anti-commutation rules:

$$\begin{aligned} \{a_p^\dagger, a_q\} &= \delta_{pq} \\ \{a_p^\dagger, a_q^\dagger\} &= \{a_p, a_q\} = 0 \end{aligned}$$

with $\{A, B\} \equiv AB + BA$.

Here, indices p, q, r, s must be understood as multi indices with a spatial component (an atom of the crystal lattice around which the mode is localized) as well as a spin component, $p = (i, \sigma)$.

Among the great successes of the twentieth century physics is the possibility through the Schrödinger stationary equation

$$\mathcal{H}_{\text{el}} \psi = E \psi \quad (2.1)$$

to fully describe, in theory, the dynamics of the system through the eigenmodes ψ . It is however untractable: a macroscopic volume of matter has an average electron count which makes it impossible to address straightforwardly. Consider for instance a 1cm^3 sample of copper. The conduction electron density of copper is $\rho = 8.5 \cdot 10^{28} \text{m}^{-3}$. There are thus an order $N = 10^{23}$ of such electrons in the sample. Factoring in the 2^N scaling of the Hilbert space, it is clear why the *many-fermion problem*, a central problem in condensed matter physics, is a notoriously challenging one. As put by Dirac and Fowler in 1929 [3]: *"The general theory of quantum mechanics is now almost complete [...]. The underlying physical laws necessary for the mathematical theory of a large part of physics and the whole of chemistry are thus completely known, and the difficulty is only that the exact application of these laws leads to equations much too complicated to be soluble"*.

As we will see, the sole large number of electrons is not actually fully responsible for the tremendous difficulty to solve the electronic Hamiltonian. What makes the task all-the-more so challenging is the presence of strong inter-electronic effects, so strong that mean-field approaches do not even offer a correct qualitative picture of the material's behaviour.

2.2 When mean-field theory breaks down: strong correlations

The first part of Hamiltonian 2.0 is quadratic in the fermionic fields, whereas the second part is quartic. In the absence of this second part, it is very easy to describe the many-body eigenstates of the Hamiltonian: they are simply obtained by filling the single-electron states which diagonalize h_{pq} , as proven in Appendix A. The exponential complexity of the problem, due to the size of the Hilbert space, is thus only apparent as h_{pq} is a $N \times N$ matrix. On the other hand, the quartic term embodies interactions, which leads to so-called *correlation* and *exchange* effects. In strongly-correlated materials, this term gives rise to specific emerging phenomena which cannot be rendered by a plain-vanilla mean-field approach.

Mean-field theory consists in describing the behaviour of an assembly of particles solely through single-particle quantities. For instance, the classical Ising spin model

$$\mathcal{H}_{\text{Ising}} = - \sum_{i,j} J_{ij} S_i S_j - \sum_i h_i S_i \quad (2.2)$$

away from criticality might be tackled from a mean field perspective by setting the operator for the component i of the spin $S_i = \langle S_i \rangle + \delta S_i$ with $\langle S_i \rangle$ the thermal average of the local magnetisation and δS_i a small fluctuation. Then at first order, $S_i S_j \simeq \langle S_i \rangle \langle S_j \rangle + \langle S_i \rangle \delta S_j + \langle S_j \rangle \delta S_i = S_i \langle S_j \rangle + \langle S_i \rangle S_j - \langle S_i \rangle \langle S_j \rangle$ so that no two-body terms remain: the mean-field Ising Hamiltonian describes independent particles in an effective field created by the other particles. To wit,

$$\mathcal{H}_{\text{Ising,MF}} = - \sum_i h_i^{\text{eff}} S_i \quad (2.3)$$

(up to a constant term) with $h_i^{\text{eff}} = h_i + \sum_j J_{ij} \langle S_j \rangle$. The determination of $\langle S_i \rangle$ is the object of a self-consistent scheme and will be touched on later, when the Dynamical Mean Field Theory is introduced.

A first depiction of collective effects beyond mean-field approaches is provided by the (Landau-) Fermi liquid theory (FLT, nicely addressed in e.g. [4]), where 'liquid' refers to the presence of interaction as opposed to the free Fermi gas. Originally a phenomenological theory, it allows to retain an independent-particle picture at low energy by introducing *quasiparticles*, which are elementary excitations corresponding to particles 'dressed' by their interaction with the other particles¹. The prefix quasi- refers to the fact that they can be traced back, upon renormalization of some physical quantities such as the mass, to low-lying particle excitations of the non-interacting system. The existence of this one-to-one correspondence relies on *adiabatic continuity* between the non-interacting system and its interacting counterpart: when interactions are turned on smoothly and the system does not run into singular behaviours (phase transitions), occupation numbers remain good quantum

¹Here we use the term particle but it must be understood that both electronic excitations and hole excitations are spanned.

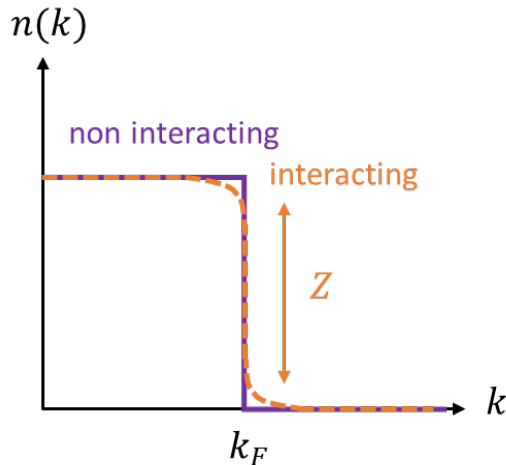


Figure 2.1: Characterization of the quasiparticle weight Z across the Fermi surface in presence of interactions within Fermi liquid theory. The discontinuity in ground state momentum density at the Fermi momentum k_F is reduced from 1 to Z as interactions are turned on.

numbers. What is meant by 'dressed' is that quasiparticle excitations interact – albeit weakly – with each other, and thus acquire a finite lifetime, which is quadratically suppressed away from the Fermi surface and with temperature. FLT allows for a first non-perturbative treatment of correlations. Moreover, it introduces a first key quantity to measure correlations, the *quasiparticle weight* $0 \leq Z \leq 1$ which measures the overlap between the quasiparticle excitations and the particle excitations. It can be read off as the discontinuity of the momentum distribution at the Fermi surface, as sketched on Figure 2.1. $Z = 1$ corresponds to the absence of interactions, also referred to as a standard *metallic* state, whereas a low value of Z signals the breakdown of the Fermi liquid description.

Another theory of correlations is the ubiquitous Density Functional Theory [5] (DFT) which deploys as a fundamental object the ground state electron density n_0 rather than what could be understood at first sight as the 'full ID' of the ground state, namely the ground state wavefunction ψ_0 . DFT is rooted in the two Hohenberg-Kohn theorems. The first theorem states that any ground state observable is a unique functional of the ground state electron density, as – assuming the ground state is non-degenerate – the latter is in one-to-one correspondence with the external potential. In particular, the ground state energy is uniquely defined from the ground state electron density. The second theorem states that the variational principle holds, namely $E[n_{\text{test}}] \geq E[n_0] \equiv E_0$. In effect, DFT is often implemented within the Kohn-Sham formalism [6] which solves self-consistently for a fictitious system of non-interacting particles that reproduce the electron density. It supposes to use an approximation for the unknowable *exchange-correlation functional* which can be selected off-the-shelf, which comes with a wide variety of complexities and accuracies. Although computationally cheap, DFT does not allow for systematic

improvement and inadequately addresses correlations, being essentially mean-field.

A most comprehensive description of correlation effects can be attained through *Dynamical Mean-Field Theory* [7], a modern theory which constitutes the context of this thesis. Through a self-consistent embedding scheme, it solves for the toy model of strongly-correlated materials, the Hubbard model, introduced in the next section.

2.3 A minimal model of strongly-correlated systems: the Hubbard model

Strongly-correlated materials are fundamentally materials which retain an atomic-like description which competes with delocalization onto lattice sites.

The toy model to address strongly-correlated systems in a simplified fashion is the Hubbard Hamiltonian, which compared with the general fermionic Hamiltonian 2.0 conserves only local onsite interaction and nearest-neighbour hopping so as to minimally capture this competition effect.

In its single-band version, where one atomic site can host up to two electrons, it reads:

$$\mathcal{H}_{\text{Hubbard}} = -t \sum_{\langle i,j \rangle, \sigma} (a_{i\sigma}^\dagger a_{j\sigma} + a_{j\sigma}^\dagger a_{i\sigma}) + U \sum_{i=1}^N n_{i\uparrow} n_{i\downarrow} \quad (2.4)$$

In this model, depicted on Figure 2.2, one considers a tight-binding lattice of N atomic spin-degenerate orbitals labelled by i , from which an electron can hop to populate a nearest neighbour orbital j with hopping energy $-t$ ($\langle i, j \rangle$ denotes a pair of sites adjacent on the lattice, whose geometry is part of the definition of a specific instance of the Hubbard model). This hopping process does not allow for spin-flips. Atomic orbitals can be populated by two antiparallel-spin electrons (as diagnosed from the density-density interaction term $n_{i\uparrow} n_{i\downarrow} \equiv a_{i\uparrow}^\dagger a_{i\uparrow} a_{i\downarrow}^\dagger a_{i\downarrow}$) at a cost of a Coulomb interaction U : we say these orbitals are *correlated*. Longer range interaction is completely screened: roughly speaking, this reflects that the electronic charge of more remote electrons is obfuscated by mobile electrons. Here, we will limit ourselves to the case $U \geq 0$, but the case $U < 0$ is also relevant, for instance – and although not a prerequisite to – in order to describe superconducting phases. The dimensionless quantity U/t is referred to as the *interaction strength* and is the relevant parameter to characterize the physical regime a specific instance of the Hubbard model captures.

We will approach the Hubbard model in the grand canonical ensemble by introducing a chemical potential term, $-\mu \sum_{i,\sigma} a_{i\sigma}^\dagger a_{i\sigma}$. We will more specifically work at half-filling, which means we enforce the half-filling of the ground state by setting the chemical potential appropriately. This is achieved through $\mu = \frac{U}{2}$, as can be

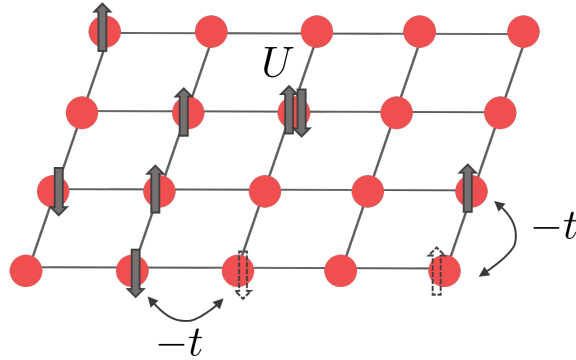


Figure 2.2: Representation of the Hubbard model. Only onsite repulsion and nearest-neighbour hopping are taken into account, with respective strengths U and $-t$. The scheme represents a 2D square lattice. Figure adapted from [9].

shown from particle-hole symmetry arguments (see for instance the lecture notes referenced as [8]).

The Hubbard model interpolates between two regimes:

- $U/t \ll 1$: this is the metallic limit. The Hamiltonian is diagonalized in the Fourier basis. Electrons are fully delocalized onto the lattice; the material is a conductor.
- $U/t \gg 1$: this is the atomic limit. The Hamiltonian is diagonal in the local basis. Electrons are frozen on atomic sites. As a consequence, the material is an insulator, more specifically a *Mott insulator*. This insulating character is not predicted within band theory and is typical of strongly-correlated materials. It typically comes with antiferromagnetic order: neighbouring electrons carry antiparallel spins.

A sketch of a typical phase diagram for the Hubbard model – which depends on the lattice geometry – is outlined on Figure 2.3. It displays the different phases of the model as the doping and the temperature $T > 0$ are varied. The doping δ is related to the average number of electrons per atomic sites n as $\delta = 1 - n$, and although a different quantity than the chemical potential μ it also relates to electron filling. In this diagram, one can spot among other phases a superconducting dome, associated to an optimal doping such that the critical temperature defined as the temperature under which the material is superconducting is maximal. This particular example underlines the importance of sorting out the phase diagram of strongly-correlated materials for material design.

The physics brought about by strong correlations is exotic and rich. This is all-the-more so interesting that one can 'move' in the phase diagram by varying the temperature, the pressure, or the voltage the material is submitted to, which translates into 'smart' behaviour: materials which can adapt positively to the conditions they are experiencing. For more details about these tangible aspects, the reader can refer for instance to [10] which reviews optical properties of correlated materials.

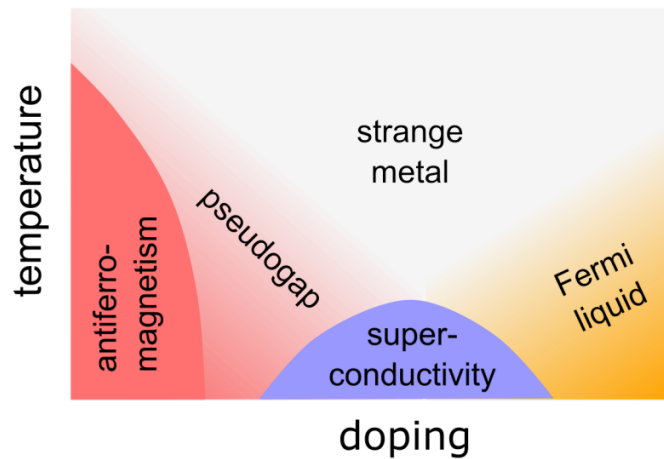


Figure 2.3: Phase diagram of the Hubbard model at finite temperature, for intermediate interaction strength U/t . Figure taken from [11].

The Hubbard model admits exact solutions in one-dimension where it can be tackled directly and, as we shall see, in infinite 'dimension' (or better said, coordination, that is for an infinitely-connected lattice). Longstanding efforts have been devoted to computing relevant physical observables in regimes of interest. A nice snapshot of these efforts, focused on the single-band, two-dimensional lattice Hubbard model, is provided in Reference [11].

The main tools to address the Hubbard model are embedding theories, and especially Dynamical-Mean Field Theory, which are the subject of the next chapter.

Embedding: Dynamical Mean-Field Theory and alike

In this chapter, we introduce the flagship theory of strongly correlated materials, Dynamical Mean-Field Theory (DMFT). We focus here on the equilibrium formulation of the theory. We first touch on the meaning of solving the Hubbard model in order to motivate the DMFT approach. We then introduce the key mathematical tool to probe correlations, namely single-particle Green's functions. We then introduce the phenomenology of DMFT, highlighting the physical phenomena it aims to capture and in which theoretical grounds it is rooted. After introducing the Hamiltonian formulation of the impurity model DMFT maps to, we move on to the mathematical formulation of the theory. The classical methods for impurity solving are then reported on, showcasing their respective limitations which make a hybrid quantum-classical approach worth-investigating. Finally, we present an alternative to DMFT which provides a low-energy description of correlation effect, the Rotationally-Invariant Slave Boson (RISB) approach. We picked the latter for our hybrid implementation due to the fact it maps the Hubbard model to a minimal-bath impurity model and relies on self-consistent equations which do not involve the time-dependent single-particle Green's function.

3.1 What does it mean to solve the Hubbard model?

In what follows, we will speak – in a loose sense – about 'solving the Hubbard model'. Let us reflect here on what we mean by that.

The spectral function $A(\omega)$, also called *density of states* (DOS), is one of the crucial quantities through which solid-state physics comes to touch with experiments. On the theoretical side, it connects with the local single-particle Green's function. Correlation effects can be read off from the spectral function: it displays distinctive features according to the value of the Coulomb term U , as can be observed on Figure 3.1. The spectral function is experimentally accessible from the photoemission current $I(\omega)$ measured in *Angle-Resolved Photo-Electronic Spectroscopy* (ARPES) experiments [13]: $I(\omega) \propto A(\omega)$. In these experiments, a light-beam is shone on the

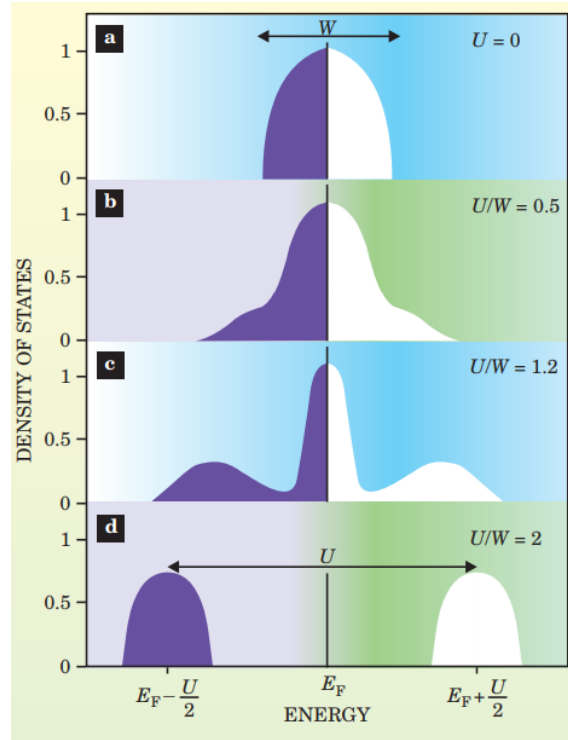


Figure 3.1: Typical density of states of the DMFT solution of the Hubbard model at zero temperature and half-filling. One can observe the free-electron DOS at $U = 0$ which is semi-circular and centered around the Fermi level E_F , whereas as U is increased, the so-called *quasiparticle peak* near the Fermi level shrinks in favour of *Hubbard bands* which are a signature of interactions. For large values of U only the Hubbard bands remain: the system is a Mott insulator. Illustration taken from [12].

material's surface, exciting electrons in the bulk, which results, on account of the photoelectric effect, in electrons being ejected from the material. The kinetic energy and angular distribution of the emitted electrons are then collected and give access to the momentum-dependent electronic band structure of solids.

We thus want to have access to the single-particle Green's function in order to connect with ARPES experiments. We might also want to compute other quantities, such as the average double occupancy of a lattice site. More generally we might want to compute thermal averages of observables over system Σ , defined as

$$\langle O \rangle_{\Sigma} = \frac{1}{Z_{\Sigma}} \text{Tr}(e^{-\beta H_{\Sigma}} O) \quad (3.1)$$

where $Z_{\Sigma} \equiv \text{Tr}(e^{-\beta H_{\Sigma}})$ is the partition function.

There are two main pathways to access $\langle O \rangle_{\Sigma}$. The first one is to diagonalize the system's Hamiltonian H_{Σ} and write down $\langle O \rangle_{\Sigma}$ in its eigenbasis: this approach is called *Exact Diagonalization* (ED). As will be explicated further in the text it is quickly limited by the memory requirements it comes with, whereas we would like to solve the Hubbard model in the thermodynamic limit, with a number of lattice sites going to infinity. A second approach is the diagrammatic approach within which $\langle O \rangle_{\Sigma}$ is rendered through stochastic sampling of configurations. The diagrammatic approach proceeds perturbatively, seeking the observable of interest as a perturbative expansion (for instance with regards to the Coulomb interaction U). It is impeded by the sign problem, an issue arising when summing terms with alternating signs (stemming here from fermionic anti-commutation) which translate into a high-variance result. The problem is all-the-more so salient that the observable, as seen from the definition 3.1, is expressed as a ratio.

Both methods are untractable for the Hubbard model, which thus cannot be tackled directly, except for a few cases when there exists an analytical solution, for instance in 1D. Otherwise, the Hubbard model can be mapped onto a simpler, proxy model Σ' such that $\langle O \rangle_{\Sigma'} \simeq \langle O \rangle_{\text{Hubbard}}$ ¹. To this end, one relies on embedding theories which consist in tiling the Hubbard lattice with cells of one or a few correlated 'Hubbard atoms' and spelling out the physics at work in the cell by considering that the remainder of the lattice acts as a 'bath', that is a reservoir of free conduction electrons.

The main embodiment of embedding theories in condensed matter is the Dynamical Mean Field Theory, which will be exposed further below. It employs single-particle Green's function as a key tool.

¹In the case of the diagrammatic approach, this resorting to a simpler proxy model has the effect of mitigating the severity of the sign problem, although the sampled diagrams are the same.

3.2 Probing correlations with single-particle Green's functions

3.2.1 Single-particle Green's function as the bridge between theory and experiment

The spectral function is related to the local time-ordered Green's function at zero temperature (where i denotes any site of the lattice)

$$G_{ii}(t) = -i \langle \psi_0 | \mathcal{T} d_i(t) d_i^\dagger(0) | \psi_0 \rangle \equiv G_{\text{loc}} \quad (3.2)$$

in which $|\psi_0\rangle$ refers to the Hamiltonian H 's ground state whereas \mathcal{T} denotes time-ordering, whose action over fermionic creation and annihilation operators in Heisenberg representation

$$d_i^{(\dagger)}(t) \equiv e^{iHt} d_i^{(\dagger)} e^{-iHt} \quad (3.3)$$

is as follows:

- if $t > 0$, $\mathcal{T} d_i(t) d_i^\dagger(0) \equiv d_i(t) d_i^\dagger(0)$,
- if $t < 0$, $\mathcal{T} d_i(t) d_i^\dagger(0) \equiv -d_i^\dagger(-t) d_i(0)$.

The interpretation of this Green's function differs with the sign of t :

- If $t > 0$, $G_{ii}(t)$ reflects the probability an electron populates the orbital associated with site i (creation operator d_i^\dagger) at time $t = 0$ and goes back to the remainder at time t
- If $t < 0$, $G_{ii}(t)$ reflects the probability a 'hole' (electronic depletion) appears on the orbital associated with site i (annihilation operator d_i) at time $t = 0$ and vanishes at time $-t$

The terminology 'Green's function' corresponds in mathematics to the impulse response of a linear system. Here, this interpretation remains valid: it can be understood by introducing the Green's function through the equations of motion, as in Reference [14]. If the system is non-interacting, namely it is quadratic in the creation/annihilation operators so that its Hamiltonian reads $\mathcal{H} = \sum_{pq} h_{pq} f_p^\dagger f_q$, then the Green's function defined above is the i th diagonal component of matrix

$$G(\omega) = [\omega - h]^{-1} \quad (3.4)$$

We can now state the relationship between the spectral function which can be drawn from ARPES experiments and the time-ordered Green's function:

$$A(\omega) = -\frac{1}{\pi} \text{Im}(G(\omega)) \quad (3.5)$$

where $G(\omega)$ (a shorthand notation for $G_{ii}(\omega)$) denotes the Fourier transform of $G(t)$, $G(\omega) = \int_{-\infty}^{\infty} e^{i\omega t} G(t) dt$.

3.2.2 Matsubara formalism

We will make use thoroughly in this manuscript of the Matsubara and imaginary time formalisms, using imaginary frequencies $i\omega_n$ and 'imaginary' time τ (a real number in spite of its name) which are the counterparts of real frequency ω and real time t . In particular, this formalism will prove useful to understand the grounds of DMFT.

Matsubara frequencies are, for fermions, the $\omega_n \equiv \frac{(2n+1)\pi}{\beta}$ with $n \in \mathbb{Z}$ and $\beta = 1/T$ the inverse temperature which might be taken to an arbitrary, high-enough value to tackle a zero-temperature system.

The so-called Matsubara Green's function which reads in imaginary time $\tau \in [0, \beta]$ (the function is antiperiodic in β):

$$\begin{aligned} G_{ii}^M(\tau) &= -\langle \psi_0 | \mathcal{T} d_i(\tau) d_i^\dagger(0) | \psi_0 \rangle \\ &= \frac{1}{\beta} \sum_{\omega_n} e^{-i\omega_n \tau} G_{ii}^M(i\omega_n) \end{aligned} \quad (3.6)$$

will yield the other Green's functions upon *analytic continuation* whose specifics depend on the quantity at hand. More specifically, the Green's functions (as well as the hybridizations and self-energies which will be introduced later) come under different 'flavours' which correspond to different Keldysh indices: the latter formalism, useful to describe out-of-equilibrium systems, will be introduced only later on, in chapter 6, but for now the reader might want to refer to Appendix C for a summary of all the definitions of these different quantities. An important member in this zoo of various Green's functions is the *retarded* instance due to the fact it is causal. For example, the zero-temperature retarded local Green's function is defined in real time as

$$G_{ii}^R(t) = -i\Theta(t) \langle \psi_0 | \{d_i(t), d_i^\dagger(0)\} | \psi_0 \rangle \quad (3.7)$$

and can be obtained from the Matsubara Green's function $G_{ii}^M(i\omega_n)$ of Equation 3.6 by doing $i\omega_n \rightarrow \omega + i0^+$. Here, the 'Feynman prescription' 0^+ denotes an infinitely-small real number and ensures the analyticity of $G_{ii}^R(\omega)$ in the upper-half complex plane, which is how causality translates into in the complex plane (a proof of this result is proposed in Appendix D). Analytic continuation from imaginary time to real time on the other hand is very cumbersome and relies for instance on Padé approximants or maximal-entropy methods.

3.3 DMFT's prescription: going back to a local, atom-like picture

Dynamical Mean Field Theory (DMFT) was developed in the 90s by A. Georges [7] and G. Kotliar [15]. It reintroduces an atomic picture by considering valence

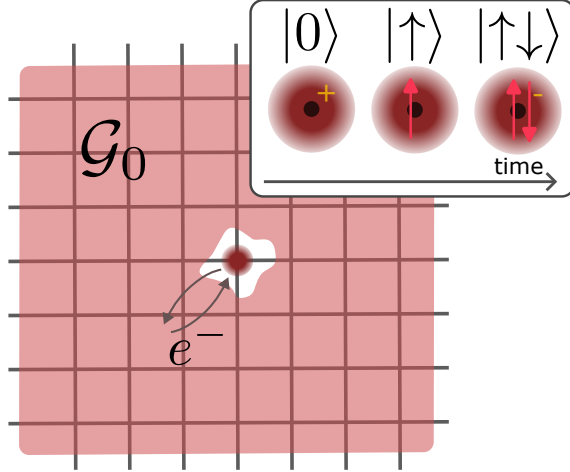


Figure 3.2: Depiction of the Dynamical Mean Field Theory viewpoint. Within DMFT, a lattice site is singled-out and regarded as an atom exchanging electrons with the remainder regarded as a bath, parametrized by the Weiss field \mathcal{G}_0 . The valence transition of the atomic sites are studied through the proxy impurity model, hence the *dynamical* character of the theory. Inset adapted from [12].

transitions in a singled-out atom, referred to as a correlated 'impurity'², exchanging electrons with a continuum of uncorrelated *bath* states. The proxy impurity model's parameters are adjusted self-consistently with the objective that, from the converged impurity model, observables regarding the original Hubbard model can be reconstructed.

First, let us touch on the *raison d'être* of this mapping onto an impurity model. In a path-integral formalism, the fundamental object is the action associated with the Hubbard model,

$$S_{\text{Hubbard}} = \int_0^\beta d\tau \left(\sum_{ij\sigma} c_{i\sigma}^\dagger(\tau) ((\partial_\tau - \mu) \delta_{ij} + t_{ij}) c_{j\sigma}(\tau) + U \sum_i n_{i\uparrow}(\tau) n_{i\downarrow}(\tau) \right), \quad (3.8)$$

from which the partition function can be computed as $Z = \int \mathcal{D}[c^\dagger, c] e^{-S_{\text{Hubbard}}}$. In this expression, $\beta = 1/T$ is the inverse temperature and $t_{ij} = t$ for connected indices, 0 otherwise. $c^\dagger(\tau)$ and $c(\tau)$ are independent Grassmann fields (a small note about Grassmann variables is proposed in Appendix F). Upon integrating out all but one site of the Hubbard lattice (labelled 0), in the limit of infinite coordination³ one is left with an effective action

²The somehow misleading term 'impurity' comes from the context such models were designed in, that is, Kondo physics where a few magnetic impurities in a bulk give rise to the Kondo effect, well known to condensed-matter physicists [16] [17]

³And in the absence of closed loops connecting lattice sites. This kind of lattice is called a *Bethe lattice*.

$$S_{\text{eff}} = - \int_0^\beta d\tau d\tau' \sum_\sigma c_{0\sigma}^\dagger(\tau) \mathcal{G}_0^{-1}(\tau - \tau') c_{0\sigma}(\tau') + U \int_0^\beta d\tau n_{0\uparrow}(\tau) n_{0\downarrow}(\tau) \quad (3.9)$$

which is that of a correlated impurity site 0 exchanging particles with a continuous bath (this derivation is sometimes referred to as the *cavity method* and is expanded in [7]).

The so-called *Weiss field* \mathcal{G}_0 plays the role of a mean-field and its inverse reads, in Matsubara frequencies,

$$\mathcal{G}_0^{-1}(i\omega_n) = G_{00}^{-1}(i\omega_n) + \Sigma_{\text{imp}}(i\omega_n) \quad (3.10)$$

where $G_{00}(i\omega_n)$ is the Green's function of the impurity site whose expression in real time was given in Equation 3.2 and where $\Sigma_{\text{imp}}(i\omega_n)$ is the *self-energy* of the impurity site. This type of equations is called a Dyson equation and defines the self-energy. The physical content of the self-energy is twofold: it accounts for interactions both through a shift in the spectral peaks (related to the real part of the self-energy) as well as a widening reflecting the finite lifetime of quasiparticles (related to its imaginary part). This is illustrated through the example of the resonant level model in Appendix E. The quasiparticle weight, first introduced in the context of the Fermi liquid theory in section 2.2, is related to the self-energy as:

$$Z = \left(1 - \frac{\partial \Sigma}{\partial \omega} \right)_{\omega=0}^{-1} \quad (3.11)$$

so that with a frequency-independent (constant) self-energy we retrieve the non-interacting, metallic limit $Z \rightarrow 1$.

Going back to \mathcal{G}_0 , its physical interpretation is the following: it gives the probability amplitude for an electron to hop from the bath onto the impurity at imaginary time τ and to hop back onto the bath at τ' . Introducing the *hybridization function*

$$\Delta(i\omega_n) = i\omega_n + \mu - \mathcal{G}_0^{-1}(i\omega_n) \quad (3.12)$$

the latter can be seen as a 'retarded hopping' compared with the original t coupling of the site with its neighbours in the Hubbard model and allows to trace local quantum fluctuations, as opposed to a static mean-field approach where \mathcal{G}_0 would be a scalar. A visual representation of the DMFT viewpoint is proposed on Figure 3.2, whereas in the next section we adopt a Hamiltonian view of the impurity model in order to spell out why the action of Equation 3.9 is indeed that of an impurity model with traced-out bath degrees of freedom, and get a better sense of the physical content of $\Delta(i\omega_n)$.

3.4 Impurity model

As seen previously, the starting point of DMFT was to notice that within the hypothesis of an infinitely-coordinated lattice, the Hubbard action could be reduced

down to an effective action which is that of a correlated 'impurity' site exchanging electrons with a free-electron bath.

This latter model can be rendered by an impurity Hamiltonian. Several such models are available and will yield a similar action S_{imp} upon tracing out the bath degrees of freedom, but we will employ the ubiquitous Anderson Impurity Model (AIM [18]):

$$\mathcal{H}_{\text{AIM}} = \underbrace{U n_{\uparrow}^d n_{\downarrow}^d - \mu \sum_{\sigma=\uparrow,\downarrow} d_{\sigma}^{\dagger} d_{\sigma}}_{H_{\text{imp}}} + \underbrace{\sum_{p=0}^{n-1} \sum_{\sigma=\uparrow,\downarrow} \epsilon_p a_{p\sigma}^{\dagger} a_{p\sigma}}_{H_{\text{bath}}} + \underbrace{\sum_{p=0}^{n-1} \sum_{\sigma=\uparrow,\downarrow} (V_p a_{p\sigma}^{\dagger} d_{\sigma} + \text{h.c.})}_{H_{\text{hyb}}}. \quad (3.13)$$

This Hamiltonian can be decomposed as follows:

- H_{imp} describes a correlated orbital, which exhibits onsite Coulomb interaction and lies at energy $-\mu$ where μ is the chemical potential, aka the Fermi level
- H_{bath} describes a reservoir of conduction, free electrons with energies ϵ_p
- H_{hyb} renders tunneling between electrons localized on the impurity site and bath electrons, it is characterized by the hoppings V_p (which we considered spin-independent).

The drawback of the Hamiltonian formulation of the impurity model is that the number of bath sites n should be infinite in order to work in the thermodynamic limit. However, it is how the impurity model is usually tackled in hybrid quantum-classical approaches. Moreover, it is more convenient in the objective to further explain how the DMFT reduction of the Hubbard model to an impurity model is achieved in practice.

Let us first retrieve the action associated with the impurity model from the Hamiltonian \mathcal{H}_{AIM} . The connection between these two quantities is the transformation $S_{\text{AIM}} = \int_0^{\beta} d\tau \left(\sum_j \xi_j^{\dagger} \partial_{\tau} \xi_j + H_{\text{AIM}}(\xi_j^{\dagger}, \xi_j) \right)$ where ξ_j is a Grassmann variable spanning the Grassmann counterparts of the fermionic operators d_{σ} and $a_{p\sigma}$. It can be expanded as

$$S_{\text{AIM}} = \int_0^{\beta} d\tau \left(U n_{\uparrow}^d(\tau) n_{\downarrow}^d(\tau) + \sum_{\sigma} d_{\sigma}^{\dagger}(\tau) (\partial_{\tau} - \mu) d_{\sigma}(\tau) + \sum_{p\sigma} \left(a_{p\sigma}^{\dagger}(\tau) (\partial_{\tau} + \epsilon_p) a_{p\sigma}(\tau) + V_p (a_{p\sigma}^{\dagger}(\tau) d_{\sigma}(\tau) + \text{h.c.}) \right) \right)$$

Performing the integration over the fields $a_{p\sigma}$ in the partition function $Z_{\text{AIM}} \equiv \int \mathcal{D}[\xi_j, \xi_j^{\dagger}] e^{-S_{\text{AIM}}}$ (which is achieved by recognizing a Gaussian integral), one is left with an effective action

Effective local impurity problem

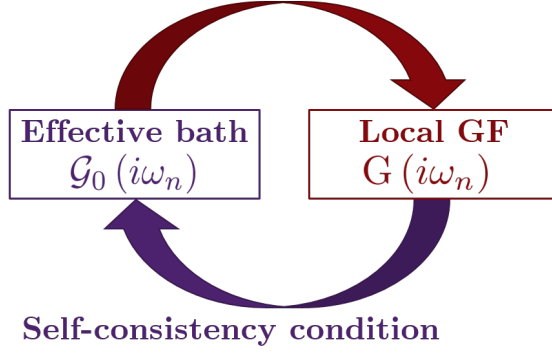


Figure 3.3: The DMFT iterative scheme. Image adapted from [19].

$$S_{\text{eff,imp}} = \int_0^\beta d\tau U n_\uparrow^d(\tau) n_\downarrow^d(\tau) - \int_0^\beta d\tau d\tau' d_\sigma^\dagger(\tau) ((-\partial_\tau + \mu)\delta(\tau - \tau') - \Delta(\tau - \tau')) d_\sigma(\tau') \quad (3.14)$$

with the effect of the bath remaining tangible through retardation effects captured by the hybridization function $\Delta(\tau - \tau')$ which depends on the imaginary time interval. Its expression in Matsubara frequencies can be shown to be

$$\Delta(i\omega_n) = \sum_p \frac{|V_p|^2}{i\omega_n - \epsilon_p} \quad (3.15)$$

as expanded in Appendix H.

Comparing expressions 3.9 and 3.14, the AIM will provide a good proxy model to the original Hubbard model provided its hybridization to the bath is such that the Weiss field

$$\mathcal{G}_0^{-1}(i\omega_n) = i\omega_n + \mu - \Delta(i\omega_n) \quad (3.16)$$

matches the non-interacting local Green's function of the Hubbard model. Thus, the DMFT procedure within the Hamiltonian approach boils down to a bath fitting, with an hybridization being defined from the original Hubbard model and that we seek to fit with parameters ϵ_p, V_p . The next section introduces the self-consistent scheme that is implemented to complete this task.

3.5 DMFT self-consistency scheme

The goal of DMFT is to be able to compute the local, interacting Green's function of a site of the Hubbard lattice, whose expression in Matsubara frequencies is:

$$G_{\text{loc}}(i\omega_n) \equiv \sum_{\mathbf{k} \in \text{BZ}} G(\mathbf{k}, i\omega_n) = \sum_{\mathbf{k} \in \text{BZ}} \frac{1}{i\omega_n + \mu - \epsilon_{\mathbf{k}} + \Sigma_{\text{latt}}(\mathbf{k}, i\omega_n)} \quad (3.17)$$

with $\epsilon_{\mathbf{k}} = t \sum_{\langle i,j \rangle} e^{i\mathbf{k} \cdot (\mathbf{R}_i - \mathbf{R}_j)}$ is the energy dispersion relation and the \mathbf{k} -summation is over the first Brillouin zone.

Since this task is untractable, DMFT consists in finding an optimal mapping from the Hubbard model onto an impurity model which will provide $G_{\text{imp}}(i\omega_n)$ as a proxy for $G_{\text{loc}}(i\omega_n)$. The equivalence of both models, based on the existence of an effective representation of the Hubbard action as that of an impurity model (Equation 3.9), is only valid in the limit of infinite coordination (or in the atomic limit $t = 0$, namely, as long as the self-energy is purely local). Otherwise, an optimal mapping is sought after through the following iterative procedure.

Being given a Weiss field \mathcal{G}_0 (one launches the procedure with a guess) and an impurity model, one can compute the local interacting Green's function $G_{\text{imp}}(i\omega_n)$ (by means of 'solving the impurity model') and deduce $\Sigma_{\text{imp}}(i\omega_n)$ through Dyson equation, considering the Weiss field as being the non-interacting ($U = 0$) Green's function of the impurity:

$$\Sigma_{\text{imp}}(i\omega_n) = \mathcal{G}_0^{-1}(i\omega_n) - G_{\text{imp}}^{-1}(i\omega_n) \quad (3.18)$$

DMFT proceeds with the approximation that the local self-energy of the interacting lattice model is \mathbf{k} -independent. This comes at a price: one cannot achieve so a spatial resolution in the description of correlation effects. It however allows to set:

$$\Sigma_{\text{latt}}(\mathbf{k}, i\omega_n) \leftarrow \Sigma_{\text{imp}}(i\omega_n) \quad (3.19)$$

One can then use $\Sigma_{\text{imp}}(i\omega_n)$ in lieu of $\Sigma_{\text{latt}}(\mathbf{k}, i\omega_n)$ in Equation 3.17 to compute $G_{\text{loc}}(i\omega_n)$. This gives rise to a new Weiss field computed self-consistently as

$$\mathcal{G}_0^{-1}(i\omega_n) = G_{\text{loc}}^{-1}(i\omega_n) + \Sigma_{\text{imp}}(i\omega_n) \quad (3.20)$$

and the procedure is repeated over, until the two models yield the same local interacting Green's function, namely $G_{\text{imp}}(i\omega_n) \simeq G_{\text{loc}}(i\omega_n)$. This iterative scheme is represented on Figure 3.3. It can be compared with the usual self-consistent scheme at work in the mean-field treatment of the Ising model: recalling that the model is cast to the effective model $\mathcal{H}_{\text{Ising, MF}} = - \sum_i h_i^{\text{eff}} S_i$ with $h_i^{\text{eff}} = h_i + \sum_j J_{ij} \langle S_j \rangle$, the local magnetisation $\langle S_j \rangle$ is self-consistently computed from the implicit relation $\langle S_i \rangle = \tanh(\beta h_i^{\text{eff}}) = \tanh\left(\beta \sum_j J_{ij} \langle S_j \rangle + \beta h_i\right)$.

The bottleneck of DMFT is the solving of the impurity model. Several approaches were developed over the years, all of which having their own advantages and drawbacks.

3.6 Impurity solving: methods and limitations

The main methods to solve the impurity model are the following:

- Exact Diagonalization [20]: bath modes number are truncated to some finite value n and the now tractable model is exactly solved. The problem with this

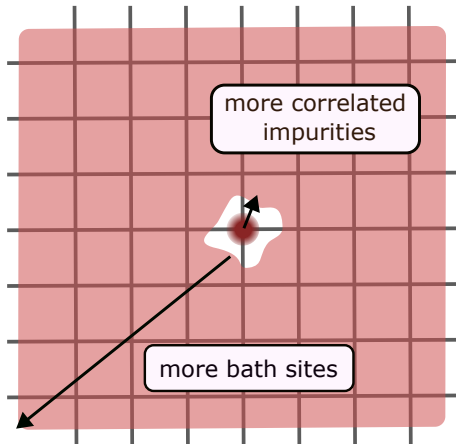


Figure 3.4: Two directions along which DMFT results can be improved. The first direction is investigated in chapter 5; the second one, in chapter 6.

method is that only a very limited number of spin-degenerate bath orbitals can be addressed (up to 27, if one resorts to the Lanczos iterative diagonalization method [21] coupled with a clever representation of the AIM's ground state [22]).

- Continuous Time Quantum Monte Carlo [23]: the partition function is expanded as a perturbative series $Z(A) = \sum_n a_n A^n$ (where A can be for instance, in one embodiment of this class of algorithms, the interaction U), and the perturbative expansion's coefficients a_n are sampled within a Monte-Carlo stochastic scheme. This approach corresponds to an infinite bath, but gives access to imaginary time quantities, yet the analytic continuation required to go back in real time is very sensitive to noise. Last but not least, this method exhibits the fermionic sign problem, whose severity increases as temperature is lowered and as the number of impurities increases.
- Numerical Renormalization Group [24]: an iterative diagonalization is performed, using a logarithmic discretization of the energy spectrum of the relevant states. This method does not work well at high energy scales.

Moreover, in order to be able to gain a spatial resolution of correlation effects, it is necessary to trade the Anderson single-impurity model for a several-impurity model so that the self-energy can carry a \mathbf{k} dependence (more specifically, to make the embedding scheme exact, the number of impurities should be increased, yielding a self-energy which is more and more space resolved, up until it gets stabilized). Momentum-resolution is necessary for instance to render the 'Fermi arcs' showing in the ARPES spectrum of cuprates in their *pseudogap* phase. This is the scope of an extension of DMFT referred to as *cluster* or *cellular* DMFT [25], as well as its *Dynamical Cluster Approximation* [26, 27] counterpart formulated in the reciprocal \mathbf{k} -space.

All the methods above are nevertheless limited to a low number m of impurity orbitals. These orbitals, since they exhibit correlation, can be seen as the truly

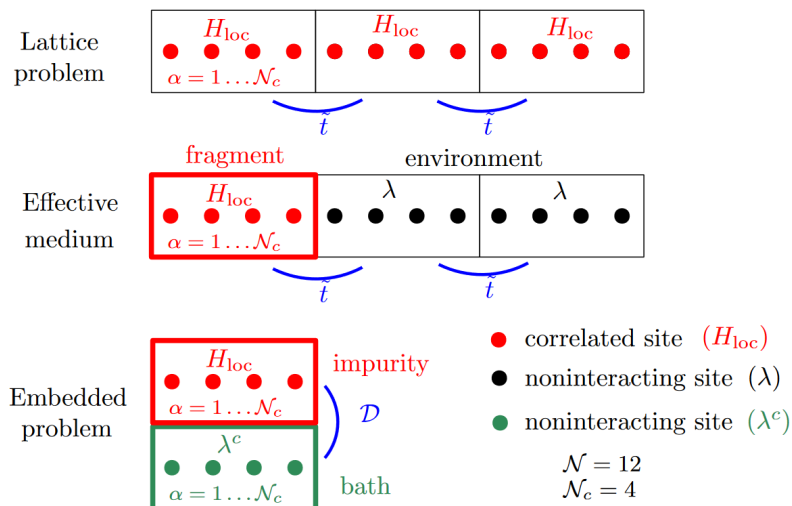


Figure 3.5: The different models – original lattice, effective and embedded – considered within RISB. Image taken from [30].

quantum ones. As a consequence, treating them on a quantum computer sounds like a very promising endeavour and at the start of and along this thesis, a few efforts have emerged to design and implement a hybrid quantum-classical DMFT scheme, sparked by the original 2016 proposal by Bauer et al. [28] and the proof-of-concept set forth by Kreula et al. [29].

The quantum-classical offshoot of DMFT that we tackled is essentially that of the original proposal of [28]: it relies on a Hamiltonian formulation of the impurity model. Thus, its accuracy is limited both by the impurity cluster size and by the size of the bath. During my thesis, I tried to improve in both of these directions, which are represented on Figure 3.4.

Before delving into the specifics of tackling DMFT with a quantum computer, which is the object of the next chapter, we finish the current chapter by introducing an alternative embedding scheme that I have resorted to to advance along the first line of improvement, namely the impurity cluster size. This embedding scheme, dubbed *Rotationally-Invariant Slave Boson* (RISB), is a less computationally-demanding alternative to cellular DMFT which has appealing features for the quantum-classical approach. It is introduced in the next section. The scheme has been put to use to obtain results which are reported later on, in chapter 5.

3.7 Rotationally-Invariant Slave Boson (RISB) method

3.7.1 Theory

The rotationally-invariant slave boson method (RISB [31, 32], a generalization of the work by Kotliar and Ruckenstein [33]) is a less computationally-demanding alternative to DMFT. It provides a low-energy expansion of the self-energy, and con-

sequently yields results regarding ground state properties whose accuracy is close to that of DMFT. We will see that the RISB approach has two features particularly desirable to limit the impediments to a quantum-classical implementation of embedding.

Within RISB, the self-energy is expanded as

$$\Sigma(\omega) = \omega(I - (R^\dagger R)^{-1}) + R^{-1}\lambda(R^\dagger)^{-1} \quad (3.21)$$

where R is the mass renormalization weight matrix and λ the static energy shift matrix. Both are complex matrices with size $2N_c \times 2N_c$, where N_c denotes the number of correlated impurities. R and λ carry a spatial resolution. In particular, R yields a (partially) momentum-resolved quasiparticle weight, $Z = RR^\dagger$, which was one of the objectives which motivated the scheme.

R and λ parametrize the effective Hamiltonian over the lattice as

$$\mathcal{H}_{\text{eff}} = \sum_{\mathbf{k} \in RBZ} [R_{a\alpha} \epsilon_{\mathbf{k}}^{\alpha\beta} R_{\beta b}^\dagger + \lambda_{ab}] f_{\mathbf{k}a}^\dagger f_{\mathbf{k}b} \quad (3.22)$$

The self-consistent mapping is realized onto an embedded Hamiltonian of the form

$$\begin{aligned} \mathcal{H}_{\text{emb}}[\mathcal{D}, \lambda^c] &= U \sum_i n_{i\uparrow}^c n_{i\downarrow}^c + \sum_{ij,\sigma} t_{ij} c_{i\sigma}^\dagger c_{j\sigma} \\ &+ \sum_{ab,\sigma} [\lambda^c]_{ab} f_{b\sigma} f_{a\sigma}^\dagger + \sum_{ia,\sigma} ([\mathcal{D}]_{ia} c_{i\sigma}^\dagger f_{a\sigma} + \text{h.c.}) \end{aligned} \quad (3.23)$$

and is rooted in the functional integral formalism, namely by means of minimization of the free-energy functional. A scheme of the RISB embedding scheme is depicted on Figure 3.5.

As its name indicates, this embedding method relies on the introduction of auxiliary degrees of freedom, the slave bosons. These additional degrees of freedom allow to treat the spin and charge degrees of freedom on an equal footing by second-quantizing valence fluctuations, and render the free-energy functional bilinear in the fermionic operators⁴. Among the states living in the enlarged space, physical states must be retrieved: within functional integral formalism, this is achieved upon imposing some constraints through Lagrange multipliers. A specificity of the *rotationally-invariant* formulation of the scheme [35] is that the free-energy functional is also bilinear in the slave-boson amplitudes, by enforcing spin-rotation invariance. While this is made at the expense of additional Lagrange multipliers and variables, it allows for a simplified minimization scheme whose equations are exposed in the next paragraph.

⁴As an alternative to Hubbard-Stratanovitch decoupling [34].

3.7.2 Slave-boson equations

The RISB free-energy functional has six variables $\Delta^p, R, \lambda, \mathcal{D}, \lambda^c, |\Phi\rangle$ and its minimization translates into the following six Lagrange equations:

$$\Delta_{\alpha\beta}^p = \sum_{\mathbf{k} \in \text{BZ}, i\omega_n} [i\omega_n - R\varepsilon_{\mathbf{k}}R^\dagger - \lambda + \mu]_{\beta\alpha}^{-1} e^{i\omega_n 0^+}, \quad (3.24a)$$

$$\left[(\Delta^p(1 - \Delta^p))^{1/2} \right]_{\alpha\mu} \mathcal{D}_{\beta\mu} = \sum_{\mathbf{k} \in \text{BZ}, i\omega_n} \left[\{\varepsilon_{\mathbf{k}}R^\dagger\} [i\omega_n - R\varepsilon_{\mathbf{k}}R^\dagger - \lambda + \mu]^{-1} \right]_{\beta\alpha} e^{i\omega_n 0^+}, \quad (3.24b)$$

$$\lambda_{\alpha\beta}^c = -\lambda_{\alpha\beta} - \left(\mathcal{D}_{\gamma\delta} R_{\eta\gamma} \frac{\partial \left[(\Delta^p(1 - \Delta^p))^{1/2} \right]_{\eta\delta}}{\partial \Delta_{\alpha\beta}^p} + \text{c.c.} \right), \quad (3.24c)$$

$$\mathcal{H}_{\text{emb}}|\Phi\rangle = E_0|\Phi\rangle, \quad (3.24d)$$

$$\langle \Phi | f_\beta f_\alpha^\dagger | \Phi \rangle = \Delta_{\alpha\beta}^p, \quad (3.24e)$$

$$\langle \Phi | c_\alpha^\dagger f_\beta | \Phi \rangle = R_{\gamma\alpha} \left[(\Delta^p(1 - \Delta^p))^{1/2} \right]_{\gamma\beta}. \quad (3.24f)$$

where we have used Einstein convention which implies that repeated indices are summed over. c.c. denotes complex conjugation. Here, $\varepsilon_{\mathbf{k}}$ is the free dispersion on a square lattice tiled with N_c -site unit cells (as in, e.g., Reference [32], and as explicated in the next paragraph). $i\omega_n$ denotes Matsubara frequencies, and $\mathbf{k} \in \text{BZ}$ denotes discretized points in the first Brillouin zone.

\mathcal{H}_{emb} is the impurity model defined in Equation 3.23, comprising N_c correlated orbitals ("impurities", corresponding to c operators) and N_c bath orbitals (corresponding to f operators). The arising in RISB of a bath whose size is that of the correlated cell is related to the Schmidt decomposition⁵ and won't be discussed any further, but it is a crucial point as the bath size is exactly that of the cell without loss of accuracy. Its ground state is denoted as $|\Phi\rangle$. The Greek indices are multi-indices $\alpha = (i, \sigma)$ with $i = 1 \dots N_c$ and $\sigma = \uparrow, \downarrow$. \mathcal{D} and λ^c are matrices which parametrize this embedded model. Δ_p is called the local density matrix. The reader might refer to Ref. [30] for a derivation of these equations as well as a more thorough introduction to the meaning of the variables \mathcal{D}, λ^c and Δ^p . Finally, as stated previously, R and λ are low-energy parametrizations of the lattice self-energy via Equation 3.21.

3.7.3 Self-consistent solving of the slave-boson equations

The self-consistent scheme defined by the set of Equations 3.24 can be understood as the following forward recursion:

⁵We recall that the Schmidt decomposition is behind the purification of open quantum systems: any density matrix of an open system can be considered as the reduced density matrix of the pure density matrix of a system which is twice the size as the system under scrutiny.

- starting from an initial guess for (R, λ) , one gets Δ^p through 3.24a.
- This allows to find a parametrization (\mathcal{D}, λ^c) to the embedded Hamiltonian \mathcal{H}_{emb} : this parametrization is prescribed by Equations 3.24b and 3.24c.
- The embedded model is solved for its ground state $|\Phi\rangle$ (Equation 3.24d).
- Then, the static correlators over the ground state $|\Phi\rangle$ of \mathcal{H}_{emb} , $\langle\Phi|f_\beta f_\alpha^\dagger|\Phi\rangle$ and $\langle\Phi|c_\alpha^\dagger f_\beta|\Phi\rangle$, are computed: these two latter steps constitute the 'impurity solving' part of the scheme.
- This sets a new R upon combining equations Equations 3.24e and 3.24f, and a new λ with Equation 3.24c.
- Then, Δ_p is updated with Equation 3.24a which in turn defines new parametrizations \mathcal{D} and λ^c for the embedded model.

The procedure is repeated until convergence (e.g. stabilization of the static correlators).

As we can see, the self-consistency equations imply *static* correlators, as opposed to the *dynamical* correlators Green's functions represent. We mean by that that these correlators do not conjure time evolution, contrarily to the Green's function which embeds time-evolution through the definition of the creation and annihilation operators in Heisenberg representation, to wit $G_{ii}(t) \propto \langle\Phi|c_i(t)c_i^\dagger(0)|\Phi\rangle$. In chapter 4, we will see that time-evolving on a quantum chip comes with deep (many-gate) circuits which pick up a lot of noise as they are executed. This makes RISB more likely to succeed in presence of noise at realistic levels than DMFT. Also, within RISB the bath has inherently as many sites as there are impurities: we thus set aside spurious effects which could arise due to the bath truncation.

Computing with noisy quantum devices

Every computation, at its core, relies on the fundamental principles of the physical world. However, multiple layers of abstraction usually mask the underlying physical phenomena. Nevertheless, it is worth noting that nature itself exhibits unparalleled computational capabilities. By effectively translating an abstract problem into the language of nature, we unlock the remarkable potential to solve complex challenges by simply observing and analyzing natural processes. This approach is at the heart of *simulation*, where we harness the inherent computational power of the natural world to tackle a wide range of problems.

Let us take as an example the NP-hard problem of Steiner tree determination, that we state in a simplified fashion also known as the *motorway problem*. Given a set of vertices, we want to determine how to make all these vertices connected by exactly one path such that the total length of edges is minimal. The structure of paths is called a tree, and might contain ancillary vertices which are external to the initial set of vertices. We might think of it as the shortest-length road structure connecting a bunch of cities. For a few vertices, this optimization problem can be solved leveraging surface minimization at work in the physical world, namely by plunging pins in soapy water and observing the structure of the soap film relax! For a larger collection of vertices, instabilities most likely prevent the soap film to adopt the Steiner tree configuration and it is not expected that analog devices provide a mean to solve NP-complete problems[36].

This fundamental idea of harnessing nature's computational power in a raw form was brought into the quantum realm by Richard Feynman in the 1980s [37]. Quantum mechanical systems evolve according to the Schrödinger equation: to understand their behaviour, one is 'simply' required to solve the equation. However, this task becomes quickly untractable with classical means as system size increases. This inspired the following insight: to solve a quantum problem, one would better use a system which itself is quantum!

The advent of the second quantum revolution, with the control of individual quantum systems now being at reach, made quantum simulation a reality. Nowadays, even prototypes of *universal* quantum computers are arriving in laboratories. Just

as soap films are too unstable to be used to solve relevant-size optimization problems, for now such devices are highly error-prone: we are currently experiencing a stage of quantum computing which was dubbed *Noisy Intermediate Scale Quantum* (NISQ [38]). Yet, strong theoretical grounds support the ability of quantum devices - upon enhancement of qubit quality and control - to unlock computations that remain unfeasible on classical computers, including supercomputers.

In this section, we present the principles onto which quantum computation is based, flash at the different types of quantum computing devices and delve more specifically into the workings of quantum computation for the many-fermion problem.

4.1 The paradigm of quantum computation

4.1.1 From the classical bit to qubits

Classical computation is based on chains of bits, which are either 0 or 1. Classical programs consist in recording and manipulating bistrings. They rely on hardware working according to the laws of classical physics, the central piece being the transistor which modulates a current depending on some input signal. Computational power has increased over time owing to the miniaturization of transistors, at a rate described by the famous Moore law. However, there is a hard limit to miniaturization: the arising of quantum effects past a certain scale, below a few nanometers.

Quantum mechanics (QM) came out as one of the main flagship advances of 20th century physics. It is governed by the three following main principles:

Principle 1 (Hilbert space) Closed quantum systems are described by Hilbert spaces, which are complex vector spaces equipped with an inner product. Composite quantum systems (say $A + B$) are described by the tensor product of the Hilbert spaces of the subsystems, $\mathcal{H} = \mathcal{H}_A \otimes \mathcal{H}_B$. Any normalized complex linear combination of states is a physically acceptable state: this is the superposition principle. We will denote the state of a quantum system using the ket notation $|\psi\rangle \in \mathcal{H}$. Global phase factors have no physical meaning: $e^{i\varphi}|\psi\rangle$ and $|\psi\rangle$ describe the same system states, so that the fundamental objects are rather the *rays* of the Hilbert space $\{e^{i\varphi}|\psi\rangle, \varphi \in \mathbb{R}\}$.

An important consequence of the superposition principle for composite systems is *entanglement*: whereas some global states might be described in terms of a product $|\phi_A\rangle \otimes |\phi_B\rangle$ of a well-defined state of subsystem A , $|\phi_A\rangle$, and a well-defined state of subsystem B , $|\phi_B\rangle$, some states do not admit such a factored description. They are said to be entangled.

Principle 2 (Schrödinger unitary dynamics) Let $|\psi(t)\rangle \in \mathcal{H}$ be the state at time t of a closed system S . The evolution of $|\psi(t)\rangle$ is entirely described by its

Hamiltonian $\mathcal{H}(t)$ according to the so-called Schrödinger equation (we set $\hbar = 1$):

$$i\partial_t |\psi(t)\rangle = \mathcal{H}(t) |\psi(t)\rangle \quad (4.1)$$

which is solved introducing the unitary time evolution operator

$$|\psi(t')\rangle = \underbrace{\mathcal{T} e^{-i \int_t^{t'} \mathcal{H}(s) ds}}_{U(t',t)} |\psi(t)\rangle \quad (4.2)$$

where \mathcal{T} corresponds to the time-ordering operator such that $\mathcal{T}A(t)B(t') = A(t)B(t')$ if $t \geq t'$, $\xi B(t')A(t)$ otherwise (with $\xi = -1$ if A, B are fermionic operators, $\xi = +1$ if they are bosonic).

Thus, any closed system evolves linearly: a consequence of that is the important *non-cloning theorem* which states that one cannot be given a state and a 'fresh quantum register' $|\bar{0}\rangle$ to write $|\psi\rangle$ onto: otherwise, there would be a unitary U such that $U(|\psi\rangle \otimes |\bar{0}\rangle) = |\psi\rangle \otimes |\psi\rangle$, which violates linearity ($U((\alpha|\psi_\alpha\rangle + \beta|\psi_\beta\rangle) \otimes |\bar{0}\rangle) = (\alpha|\psi_\alpha\rangle + \beta|\psi_\beta\rangle) \otimes (\alpha|\psi_\alpha\rangle + \beta|\psi_\beta\rangle) \neq \alpha|\psi_\alpha\rangle \otimes |\psi_\alpha\rangle + \beta|\psi_\beta\rangle \otimes |\psi_\beta\rangle$ in general).

Principle 3 (Measurement) Measurements are concerned with estimating the expectation value $\langle\psi|O|\psi\rangle$ in state $|\psi\rangle$ of an *observable* O .

An observable is a hermitian operator $O = O^\dagger$ over the system's Hilbert space, and as such it can be decomposed as a linear combination of projectors P_j onto orthogonal subspaces E_j : $O = \sum a_j P_j$ with $O|\phi_j^{(k)}\rangle = a_j|\phi_j^{(k)}\rangle \forall |\phi_j^{(k)}\rangle \in E_j$, $\langle\phi_i^{(k)}|\phi_j^{(k')}\rangle = 0 \forall i \neq j$.

The expectation value is thus defined as

$$\langle\psi|O|\psi\rangle = \sum_j a_j \langle\psi|P_j|\psi\rangle \quad (4.3)$$

When measuring state $|\psi\rangle$ in the eigenbasis of O , eigenvalue a_j is read with probability given by Born's rule:

$$p_j = \|P_j|\psi\rangle\|^2 \quad (4.4)$$

In particular, if the eigenspaces of O are one-dimensional $P_j = |\phi_j\rangle\langle\phi_j|$ so that we can write $|\psi\rangle = \sum_j c_j |\phi_j\rangle$ and the Born rule reads

$$p_j = |c_j|^2 \quad (4.5)$$

Furthermore, just after the measurement was made the state is projected onto the eigenspace associated to the observed outcome

$$|\psi'\rangle = \frac{P_{j_{\text{meas}}}|\psi\rangle}{\|P_{j_{\text{meas}}}|\psi\rangle\|} \quad (4.6)$$

Owing to the probabilistic nature of the measurement outcome, the expectation value is defined as the limit of the empirical average over a number of repeated measurements going to infinity:

$$\langle \psi | O | \psi \rangle = \lim_{M \rightarrow \infty} \frac{1}{M} \sum_{m=1}^M a_{j_{\text{meas}}}^{(m)} \quad (4.7)$$

The destructive nature of the measurement process coupled to the non-cloning theorem incurs a first limit on quantum computation: information can only be extracted upon repeated measurements on identically prepared systems.

Qubits The qubit is the quantum counterpart to the classical bit. Qubit and qubit registers can be seen as abstract entities satisfying a set of requirements, known as DiVincenzo criteria [39]. A qubit is a quantum system admitting an accurate two-level description (like, e.g., a spin), meaning that so-called leakage out from the computational subspace (probability for the state to acquire a component different from the two levels) is suppressed. For instance, superconducting qubits correspond to anharmonic potentials arising in superconducting circuits. Such circuits are similar to LC circuits, but with an inductance replaced by a Josephson junction in order to introduce anharmonicity, without which exciting from the ground to the first excited state would also trigger the excitation from the first excited state to the second excited state, and so on. Rydberg atoms' two levels can correspond either to their ground state and a selected Rydberg state (electronic layer with a very large quantum number n), or to two different Rydberg states with dipole coupling. From the first principle of QM, a register comprising n qubits can thus represent states from a 2^n -dimensional Hilbert space. Operations over the qubit register correspond to a certain Hamiltonian, and are reversible. Furthermore, we require a fine control over the qubits' state. Different degrees of control will correspond to different quantum computing paradigms.

4.1.2 Quantum computing paradigms

There are three main classes of quantum computing devices, according to the paradigm they fit in: quantum annealers, analog QC/simulators and digital quantum computers. The three paradigms are actually all equivalent in some sense that will be made clearer later.

Quantum annealers (Adiabatic Quantum Computing) Quantum annealers such as D-Wave's machines are devices which implement adiabatic evolution. They are grounded on the *adiabatic theorem*: if one begins in the ground state of an initial Hamiltonian H_0 and smoothly changes the Hamiltonian to a target Hamiltonian of interest H_1 according to an interpolation schedule s , namely

$$H(t) = (1 - s(t))H_0 + s(t)H_1, \quad (4.8)$$

with $s(t = 0) = 0$ and $s(t = T) = 1$ (e.g. a linear interpolation schedule $s(t) = t/T, t \in [0, T]$), then the state along the evolution remains the ground state of the current Hamiltonian. In particular, at the end of the evolution the ground state of

H_1 is attained. This theorem can be leveraged to prepare a complicated ground state by evolving from an easy-to-prepare one (typically, a Slater determinant, that is to say a state from the computational basis). Here, 'smoothly' must be understood in terms of rate of change of the Hamiltonian with regards to the spectral gap $\Delta = E_1 - E_0$. A rule of thumb is to evolve during a total time $T \gg \frac{\max_s \|\frac{d}{ds} H(s)\|}{\min_s \Delta(s)^2}$ where $\|\cdot\|$ denotes the spectral norm.

Quantum simulators/Analog quantum computers Quantum simulators are platforms characterized by a resource Hamiltonian H_{res} whose control fields can be adjusted (according to a *schedule*) to perform the subset of operations $e^{-i \int_0^T H_{\text{res}}(t) dt}$ allowed by the form of the resource Hamiltonian. For instance, depending on which atomic levels they target, platforms of Rydberg atoms (see, e.g., [40, 41]) may implement an Ising Hamiltonian:

$$H(t) = \sum_{ij, i \neq j} \frac{C}{|r_i - r_j|^6} n_i n_j + \frac{\Omega(t)}{2} \sum_i X_i - \delta(t) \sum_i Z_i, \quad (4.9)$$

with $n_i = (1 - Z_i)/2$, or a *XY* Hamiltonian:

$$H(t) = \frac{1}{2} \sum_{ij, i \neq j} \frac{C}{|r_i - r_j|^3} (X_i X_j + Y_i Y_j) + \frac{\Omega(t)}{2} \sum_i X_i - \frac{\delta(t)}{2} \sum_i Z_i. \quad (4.10)$$

In these expressions, the control fields are the Rabi pulse $\Omega(t)$ and the detuning $\delta(t)$. Such platforms can also be leveraged for quantum annealing.

Universal quantum computers/Digital quantum computers Provided with a sufficient level of control, one gets endowed with an all-purpose quantum computer capable of implementing any unitary evolution. We will mainly consider such type of quantum devices in this thesis.

4.1.3 Digital quantum computing: circuits, gates, measurements

Circuits The manipulation of qubit states can be represented pictorially as a *quantum circuit*, as represented on Figure 4.3. A quantum circuit consists of horizontal lines, one per qubit, to be understood as 'evolution lines' for the qubits with time flowing from left to right. Quantum operators appear as boxes. A box in a quantum circuit must correspond to a unitary single or multi-qubit operation, but not necessarily to some operation directly accessible to the hardware: rather, the quantum circuit formalism allows to think formally about the way quantum information is transformed and read. For a given unitary, there is infinitely many circuits that represent its implementation: a first reason is that owing to the reversibility of QM, any insertion of a quantum operation V followed by V^\dagger does not change the global operation the circuit embodies. A second reason is that there are infinitely many universal sets of quantum gates to decompose a unitary onto. Even within a specified set there is still some freedom to be exploited for optimization purposes,

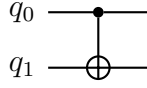


Figure 4.1: Symbol of the CNOT gate. The top qubit is the control qubit, whereas the bottom one is the target qubit.

which is the problem *quantum compilation* is concerned with and lies beyond the scope of this thesis.

Gates Gates relevant to the present work are, as written in the eigenbasis $\{|0\rangle, |1\rangle\}$ of the Pauli-Z operator, the Pauli gates

$$X = \begin{pmatrix} 0 & 1 \\ 1 & 0 \end{pmatrix}, Y = \begin{pmatrix} 0 & -i \\ i & 0 \end{pmatrix}, Z = \begin{pmatrix} 1 & 0 \\ 0 & -1 \end{pmatrix}, \quad (4.11)$$

as well as rotation gates associated to Pauli operators $P \in \{X, Y, Z\}$,

$$R_P(\theta) = \cos \frac{\theta}{2} I - i \sin \frac{\theta}{2} P, \quad (4.12)$$

the Hadamard gate

$$H = \frac{1}{\sqrt{2}} \begin{pmatrix} 1 & 1 \\ 1 & -1 \end{pmatrix}, \quad (4.13)$$

and the two-qubit entangling CNOT gate (controlled-X)

$$\text{CNOT} = \begin{pmatrix} 1 & 0 & 0 & 0 \\ 0 & 1 & 0 & 0 \\ 0 & 0 & 0 & 1 \\ 0 & 0 & 1 & 0 \end{pmatrix}. \quad (4.14)$$

Here, we have supposed that the first qubit was the *control* qubit, whose state prescribes the action over the second, *target* qubit. The matrix is written in the basis of two-qubit states ordered as $|00\rangle, |01\rangle, |10\rangle, |11\rangle$, which corresponds to the *big-endian* convention for bitstrings¹. The symbol of the gate is presented on Figure 4.1.

Finally, we will make use of Google's *fermionic simulation* gate (fSim [42])

$$\text{fSim}(\theta, \phi) = \begin{pmatrix} 1 & 0 & 0 & 0 \\ 0 & \cos \theta & -i \sin \theta & 0 \\ 0 & -i \sin \theta & \cos \theta & 0 \\ 0 & 0 & 0 & e^{i\phi} \end{pmatrix}. \quad (4.15)$$

¹This terminology can be confusing: big-endian means that the most significant bit is on the left. This is because historically *endian* does not correspond to the order one reads the bitstring, but to how the computer stores each bit in memory.

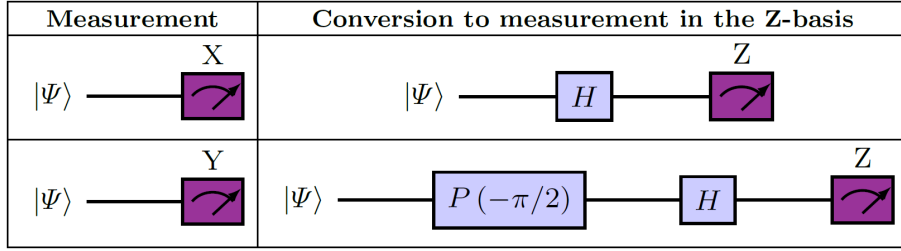


Figure 4.2: Conversion of measurements in X or Y bases into measurements in the Z basis.

Measurements Otherwise specified differently, measurements are always to be understood as being in the Z -basis. They are represented by a meter at the end of the circuit. Measuring in the X or Y basis comes with a small gate overhead, as documented on Figure 4.2. The eigenbasis of the $Z_1 \otimes \dots \otimes Z_n$ operator, namely the bitstrings $|010\dots1\rangle \dots$, is referred to as the *computational basis*.

4.2 Encoding from fermions to qubits

Encoding consists in prescribing a way to map a fermionic state onto a state of the qubit register, as well as translating a second-quantized Hamiltonian onto a 'qubit Hamiltonian' or 'spin Hamiltonian', that is, a Hamiltonian decomposed as a linear combination of Pauli words. A Pauli word is a tensor product of Pauli operators: $P_q = \otimes_{i=1}^{n_{\text{qubits}}} P_q^{(i)}$ with $P_q^{(i)} \in \{I_i, X_i, Y_i, Z_i\}$ acting on qubit i .

There is no unique procedure for encoding. The most standard mapping techniques are the Jordan-Wigner (JW) transformation [43], the Bravyi-Kitaev (BK) [44] or the parity mapping [45]. We present the JW case which is the encoding we have been using. The remainder of this paragraph is adapted from [46].

Fermionic systems can be described in second quantization through the occupancies of spin-orbitals (spatial orbitals that can only host a single spin species), which owing to Pauli exclusion principle can only take values 0 and 1 (spin orbitals are thus also referred to as *single-particle orbitals*, and the corresponding n -fermion space is referred to as the *Fock space*). It is thus natural to describe fermionic states as qubit states: in JW encoding, the fermionic state $|n_1\dots n_M\rangle_{\text{ferm}} \equiv (c_1^\dagger)^{n_1}\dots(c_M^\dagger)^{n_M}|\bar{0}\rangle$ is straightforwardly encoded onto the qubit register as $|n_1\dots n_M\rangle_{\text{qubit}}$. Then, the operator

$$Q_p^+ = |1\rangle_p\langle 0|_p = \frac{1}{2}(X_p - iY_p) \quad (4.16)$$

and its hermitian conjugate Q_p^- encode the effect of, respectively, the creation operator c_p^\dagger and the annihilation operator c_p , up to the fermionic sign. Indeed, these operators commute between each other for different qubits whereas fermionic operators anticommute:

$$\{c_p^\dagger, c_q\} = \delta_{pq}, \{c_p, c_q\} = \{c_p^\dagger, c_p^\dagger\} = 0 \quad (4.17)$$

One can remedy to this issue by choosing a specific ordering for the one-to-one correspondence between the single-particle state and the qubits, and using the following mapping:

$$c_p^\dagger \longleftrightarrow (Z_1 \otimes \dots \otimes Z_{p-1}) \otimes Q_p^+, \quad c_p \longleftrightarrow (Z_1 \otimes \dots \otimes Z_{p-1}) \otimes Q_p^-. \quad (4.18)$$

The fermionic sign is thus kept track of with the string $\bigotimes_{k=1}^{p-1} Z_k$ of Pauli- Z operators. As a consequence, an operation that is one-body at the fermionic level may translate into a multi-qubit operation. For instance, $c_1^\dagger c_3$ leads to a term $Q_1^+ Z_2 Q_3^-$ that acts on the three qubits (1, 2, 3).

4.3 Computing Green's functions with a quantum circuit

Let us consider from now on we are using JW encoding. For the purpose of studying strongly-correlated materials, we are interested in computing Green's functions. Let us consider here we are dealing with a system in equilibrium, at zero-temperature: then a single two-point Green's function contains all the information about the system's spectral properties.

We consider here the retarded Green's function G^R , to which the *spectral function* $A(\omega)$ is related to as

$$A(\omega) = -\frac{1}{\pi} \text{Im}(G^R(\omega)) \quad (4.19)$$

with $G^R(\omega)$ being the Fourier transform (see convention in Appendix B) of the retarded, causal Green's function

$$\begin{aligned} G^R(t) &= -i\Theta(t) \langle \psi_0 | \{d_1(t), d_1^\dagger(0)\} | \psi_0 \rangle \\ &= \Theta(t) \left(\underbrace{-i \langle \psi_0 | d_1(t) d_1^\dagger(0) | \psi_0 \rangle}_{G^>(t)} - \underbrace{i \langle \psi_0 | d_1^\dagger(0) d_1(t) | \psi_0 \rangle}_{G^<(t)} \right) \end{aligned}$$

$iG^>(t)$ can be expanded (i) introducing the Schrödinger representation of time-dependent operators and (ii) within JW encoding (supposing we are considering the impurity local spin component which is encoded by the first state qubit, so that we do not have to bother with Z chains) as

$$\begin{aligned} iG^>(t) &= \langle \psi_0 | e^{iHt} d_1 e^{-iHt} d_1^\dagger | \psi_0 \rangle \\ &= \langle \psi_0 | e^{iHt} Q_1^- e^{-iHt} Q_1^+ | \psi_0 \rangle \\ &= \frac{1}{4} \langle \psi_0 | e^{iHt} (X_1 + iY_1) e^{-iHt} (X_1 - iY_1) | \psi_0 \rangle \end{aligned} \quad (4.20)$$

It is now manifest that $iG^>(t)$ is the sum of four terms of the form

$$T_{kl} = \langle \psi_0 | e^{iHt} \sigma^k e^{-iHt} \sigma^l | \psi_0 \rangle \quad (4.21)$$

with $\sigma^j \in \{I, X, Y, Z\}$. Note that we dropped the qubit index in order to lighten the notation.

Any such term is accessible by aggregating statistics of two distinct quantum measurements, from the interferometry circuit \mathcal{C}_{kl} depicted on Figure 4.3. The qubit register of this circuit comprises a part holding the state, as well as an additional, *ancillary* qubit which is measured. More specifically, we can show that (see derivation in Appendix I)

$$T_{kl} = \langle Z \rangle_{\mathcal{C}_{kl}} + i \langle Y \rangle_{\mathcal{C}_{kl}} \quad (4.22)$$

In practice, the frequency dependence of the equilibrium spectral function can be obtained by introducing a small fictitious temperature and Fourier transforming up to some cut-off frequency the time-ordered Green's function G^T [28]. Appendix C lists definitions of the different types of Green's functions mentioned in this manuscript.

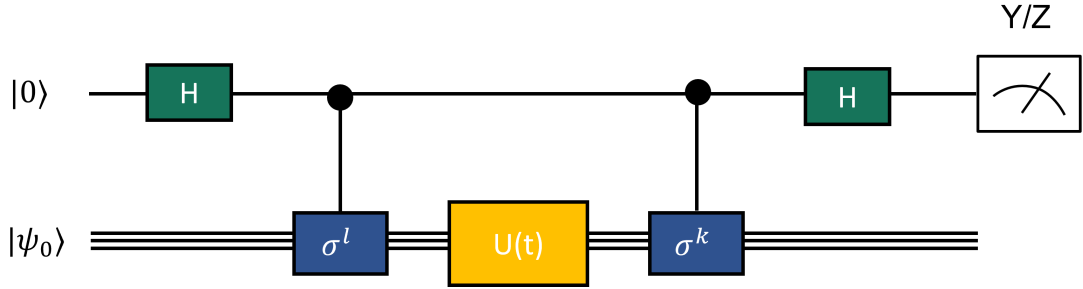


Figure 4.3: Circuit \mathcal{C}_{kl} enabling the calculation of Green's functions elements $T_{kl} = \langle \psi_0 | e^{iHt} \sigma^k e^{-iHt} \sigma^l | \psi_0 \rangle$.

The circuit represented in Figure 4.3 displays two 'black-box' items:

- the input state $|\psi_0\rangle$, which is the ground state of the Hamiltonian under consideration,
- the time evolution operator. $U(t)$

In the next section we turn to the actual implementation of these boxes.

4.4 Preparing ground states and time-evolving on the chip: main algorithms

4.4.1 Variational ground state preparation

4.4.1.1 Variational Quantum Eigensolver (VQE)

We assume we have a Hamiltonian H we would like to determine the non-degenerate ground state of, noted $|\psi_0\rangle$. This state is defined by the extremization property (Rayleigh-Ritz principle)

$$|\psi_0\rangle = \operatorname{argmin}_{|\psi\rangle \in \mathcal{H}} \frac{\langle \psi | H | \psi \rangle}{\langle \psi | \psi \rangle} \quad (4.23)$$

which simply states that from all the physical states (defined by $\langle \psi | \psi \rangle = 1$) of the Hilbert space \mathcal{H} , the ground state is the one associated to the smallest expectation value of H (energy). Whereas the Hilbert space is extremely large, the relevant portion (say, the portion of the Hilbert space which is accessible within adiabatic evolution from a simple product state in finite time) is comparatively very small. The variational characterization of the ground state coupled with the observation that only a tiny fraction of the whole Hilbert space is worth examining motivates the so-called *Variational Quantum Eigensolver* (VQE [47]) algorithm.

The underlying principle of VQE is the following: let's consider a parametrized subspace of normalized states from the Hilbert space, which we will write as $\{|\psi(\boldsymbol{\theta})\rangle = U(\boldsymbol{\theta})|\bar{0}\rangle, \boldsymbol{\theta} \in \mathbb{R}^d\}$ where U is some parametrized unitary evolution. d is the number of parameters that U holds: $U(\boldsymbol{\theta}) = G_d(\theta_d) \dots G_2(\theta_2)G_1(\theta_1)$, $G_j \in U_n(\mathbb{R})$. Let

$$\boldsymbol{\theta}^* \equiv \operatorname{argmin}_{\boldsymbol{\theta} \in \mathbb{R}^d} \langle \psi(\boldsymbol{\theta}) | H | \psi(\boldsymbol{\theta}) \rangle \quad (4.24)$$

Then, provided U was carefully chosen, we can make the following approximation:

$$|\psi_0\rangle \simeq |\psi(\boldsymbol{\theta}^*)\rangle \quad (4.25)$$

We have thus replaced the extremization of the Rayleigh quotient over the whole Hilbert space by an extremization in \mathbb{R}^d , which is now amenable to computation. The principle is illustrated on Figure 4.4.

The VQE algorithms proceeds iteratively, going back and forth between quantum and classical outputs, which makes it the most salient embodiment of *hybrid* methods. The chosen parametrized unitary U is realized as a quantum circuit (or rather, it is a quantum circuit we pick for the optimization), referred to as the *ansatz circuit*. The parameters $\boldsymbol{\theta}$ are set to some values $\boldsymbol{\theta}^{(k)}$. The corresponding fixed circuit $U(\boldsymbol{\theta}^{(k)})$ is implemented on a quantum device, and the expectation value $E^{(k)}$ of the Hamiltonian H over the output of the circuit, $E^{(k)} \equiv \langle \psi(\boldsymbol{\theta}^{(k)}) | H | \psi(\boldsymbol{\theta}^{(k)}) \rangle$, is calculated by classically aggregating the expectation values of the Pauli words $P_q H$ is made of:

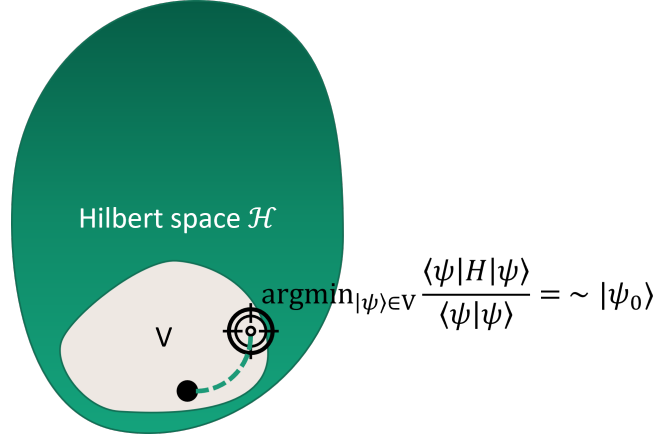


Figure 4.4: Principle of the Variational Quantum Eigensolver (VQE) algorithm. An approximation to the ground state is prepared by optimizing a variational circuit.

$$E^{(k)} \equiv \langle \psi(\boldsymbol{\theta}^{(k)}) | H | \psi(\boldsymbol{\theta}^{(k)}) \rangle = \sum_q \lambda_q \langle \psi(\boldsymbol{\theta}^{(k)}) | P_q | \psi(\boldsymbol{\theta}^{(k)}) \rangle. \quad (4.26)$$

Some other quantities such as the gradient can be evaluated with the quantum computer. The resulting energy (and as the case may be, the gradient) is fed to a classical optimizer which provides new parameters $\boldsymbol{\theta}^{(k+1)}$ to test for. Iterating the procedure one hopefully converges to some energy $E(\boldsymbol{\theta}^*)$ and gets provided with a parametrization of the ground state $\boldsymbol{\theta}^*$.

The obtained ground state parametrization is subject to two fundamental types of errors:

1. the selected subspace might not hold the ground state (which we will refer to as a lack of *expressivity*);
2. the optimization might not have yielded the lowest-energy state within the variational subspace, but instead might have gotten stuck in a local minimum.

These errors add to convergence issues, compounded by noise, when considering large-dimensional subspaces.

On the other hand, VQE exhibits key advantages for the so-called *NISQ* (Noisy, Intermediate Scale Quantum [38]) era in that one can work within the limitations of the quantum hardware at hand: schematically, this is achieved by selecting an ansatz circuit whose running time is below the decoherence time. Moreover, ground state preparation from parametrized unitaries arises naturally in certain settings such as free fermions, devising a second strategy for ansatz design.

4.4.1.2 Ansatz circuits for VQE

Strategies for ansatz circuit design fall into two main categories.

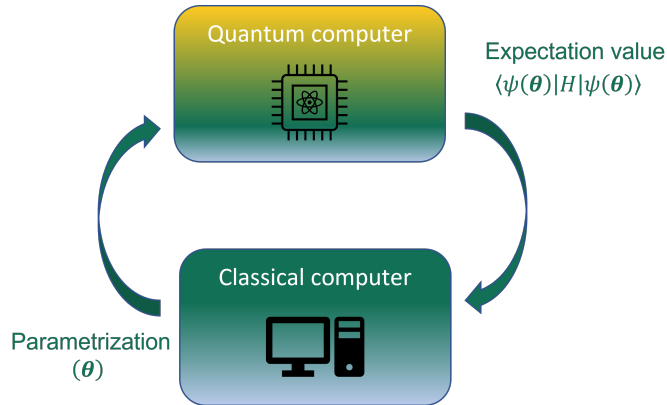


Figure 4.5: Flowchart of the Variational Quantum Eigensolver (VQE) algorithm, a quantum-classical hybrid algorithm.

The first one consists in picking a few parametrized gates native to the hardware considered, for example the fermionic simulation gate fSim for Google’s Sycamore chip, and combining them so as to generate entanglement in an unstructured fashion. It generates a class of circuits dubbed as *Hardware-Efficient Ansatz* (HEA). Expressivity is buildable in that stacking layers of gates that entangle all of the qubits systematically increases the representation power of the circuit. This strategy offers a way to consider small-depth circuit, but usually comes with a large number of parameters to be optimized and is more prone to the Barren plateau problem [48]: the optimization of high-dimensional, unstructured unitaries run into the issue of vanishing gradients due to concentration of measure phenomenon.

The second one is rooted in physical arguments. If one knows the structure of the parametrized unitary $U(\boldsymbol{\theta})$ connecting some reference state $|\phi_0\rangle$ to the target ground state $|\psi_0\rangle$ and knows how to decompose it into quantum gates, then one is provided with an exact ansatz for the VQE task.

The most famous ansatz circuit in this category comes from quantum chemistry and is dubbed the UCC (Unitary-Coupled Cluster) circuit. The trial wavefunction is written in a general form [49]:

$$|\Psi_{\text{UCC}}(\boldsymbol{\theta})\rangle = e^{T(\boldsymbol{\theta})-T^\dagger(\boldsymbol{\theta})}|\Psi_0\rangle \equiv U(\boldsymbol{\theta})|\Psi_0\rangle, \quad (4.27)$$

where T can be expanded as a set of operators of increasing complexity with $T = T_1 + T_2 + \dots$. Here, T_1, T_2, \dots stands for single, double, ... particle-hole excitation operators with respect to the state $|\Psi_0\rangle$, with

$$T_1 = \sum_{i,j} T_{ij}^{(1)} a_i^\dagger a_j, \quad (4.28)$$

$$T_2 = \sum_{i,j,k,l} T_{ij,kl}^{(2)} a_i^\dagger a_j^\dagger a_l a_k, \quad (4.29)$$

...

We will consider another embodiment of such ansatz here: the Low-Depth Circuit Ansatz (LDCA [50]), more adapted to the physics of impurity models. It starts

Type of circuit	Hardware-efficient	Physically-motivated
Expressivity	buildable	✓
Noise resilience	✓	✗
Optimization	✗	✓
Examples	thinly-dressed CNOT circuits	LDCA [50]

Table 4.1: Two leading ansatz design strategies for VQE circuits.

from the exact variational circuit to prepare free-fermion ground states. In virtue of *Thouless theorem*, such states can be obtained upon rotating the single-particle basis over a product state. The basis rotation can be decomposed onto elementary *Givens rotations*, which in turn can be implemented as so-called *matchgates*. One obtains a sizable circuit (hence the denomination low depth: the depth scales linearly with the number of fermionic modes, that is the number of qubits). Correlated ground states can be reached by tweaking the free fermion states preparation circuit in two ways:

- inserting RZZ gates, which in Jordan-Wigner encoding mirror the density-density term in the Hamiltonian
- repeating the circuit to increase the expressivity, similarly to HEA

During the first part of my thesis, I devised a method to bridge the gap between these two strategies, dubbed Natural-Orbitalization.

4.4.1.3 Optimization of the ansatz parameters

VQE optimization usually relies on standard optimization techniques, available within python’s `scipy` library. In most cases however a specific technique can be used, leveraging the parameter-shift rule [51]. Here we present briefly three standard techniques which I used in my work as well as this last technique which only applies to a certain class of circuits.

COBYLA stands for ‘Constrained Optimization BY Linear Approximation’ [52]. It is a gradient-free method based on linear approximations to the objective function. When benchmarking against other optimizers, I have found most of the time that COBYLA optimization results were at least as good.

BFGS [53] stands for Broyden, Fletcher, Goldfarb, and Shanno. It is based on estimations of the gradient, and is used extensively in a machine-learning context.

Nelder-Mead [54] belongs to the class of simplex methods, which scan the optimization landscapes at the vertices of a simplex which gets updated along the optimization. Nelder-Mead optimization is resilient to stochastic noise.

Rotosolve This terminology comes from [55], but the technique was already proposed in [51]. Due to the parameter-shift rule, a locally-optimal update can be computed by evaluating the energy over three parametrizations of the circuit:

$$\theta_j^{(\text{new})} = f(E(\theta_j^{(\text{old})}), E(\theta_j^{(\text{old})} + \frac{\pi}{2}), E(\theta_j^{(\text{old})} - \frac{\pi}{2})) \quad (4.30)$$

4.4.2 Trotterization

Trotterization is a technique to implement a time evolution $U = e^{-iHt}$ on digital quantum hardware [56], i.e., as a sequence of few-qubit gates.

Most many-body Hamiltonians are k -local, meaning they can be decomposed as a sum of terms acting on at most k qubits:

$$H = \sum_{j=1}^m \lambda_j P_j, \quad (4.31)$$

with P_j a product of at most k Pauli operators. k -locality is crucial to the viability of the trotterization technique, in that time evolution circuits will not scale exponentially with system size.

The core idea is to approximate the exponential of the sum $e^{-i\sum_j \lambda_j P_j t}$ as the product of the individual terms $e^{-i\lambda_j P_j t}$ which can easily be turned into few-qubit operations. If the different terms P_j in the Hamiltonian were to commute, then we would have $e^{-iHt} = \prod_{j=1}^m e^{-i\lambda_j P_j t}$. However, in general these terms do not commute. Rather, according to the BCH formula $e^{t(A+B)} = e^{tA}e^{tB}e^{t^2/2[A,B]}e^{t^3/6(2[B,[A,B]]+[A,[A,B]])} \dots$, so that as $t \rightarrow 0$ the error associated with taking the product to approximate the sum scales as $\mathcal{O}(t^2)$.

Thus, since the total time evolution can be exactly decomposed into a chain of n_t small timesteps (*Trotter slices*), $e^{-iHt} = (e^{-iHt/n_t})^{n_t}$, the exponential can be implemented at first order as the repeated product

$$e^{-iHt} = \left(\prod_{j=1}^m e^{-i\lambda_j P_j \frac{t}{n_t}} \right)^{n_t} + \mathcal{O}\left(\frac{m^2 t^2}{n_t}\right) \quad (4.32)$$

It is the so-called first-order *Trotter-Suzuki* formula [56].

Notably, in order to retain a fixed accuracy, the number n_t of Trotter steps must increase linearly with t . In some cases, a sublinear scaling can be proposed, but this is not generally the case in virtue of the *no fast-forwarding theorem* [57].

4.5 Quantum noise

Turning quantum computing devices into a reality represents a tremendously difficult engineering problem.

The manufacturing of high-fidelity quantum devices requires to reconcile two hardly-compatible requirements: on the one hand, one demands a fine control over the system's state, which means one has to interact with the system. On the other hand, one wants the system's state to be stable when not manipulated upon: this means we aim at minimizing environmental leaks, in other words, isolate the system as much as possible. Real-world devices are indeed noisy, in that unwanted interaction with the environment leads to decoherence effect and thus, imperfect states.

Instead of a wavefunction $|\psi\rangle$, one ends up at the end of a noisy computation with a statistical mixture, described by a density operator

$$\rho = \sum_j p_j |\psi_j\rangle \langle \psi_j| \quad (4.33)$$

which is a hermitian operator such that

$$\text{Sp}(\rho) \subset \mathbb{R}^+ \quad (4.34)$$

$$\text{Tr}(\rho) = 1 \quad (4.35)$$

As a consequence, $\text{Tr}(\rho^2) \leq 1$, the equality characterizing a pure state $\rho = |\psi\rangle \langle \psi|$.

In this section, we delve into the modelization of the evolution of such states.

4.5.1 Quantum channels and Kraus representation

The operations carried out during the execution of the circuit do not fall into the unitary picture anymore: rather, they are described as CPTP (completely positive, trace preserving) maps, also known as *quantum channels* \mathcal{E} .

Unitary operations map physical states onto physical states. Similarly, quantum channels are defined as superoperators (operators mapping operators to operators) which transform density operators onto other density operators. It follows that they must obey the following mathematical properties:

$$(\mathcal{E}(\rho))^\dagger = \mathcal{E}(\rho) \quad (4.36)$$

$$\text{Tr}(\mathcal{E}(\rho)) = \text{Tr}(\rho) = 1 \quad (4.37)$$

$$\text{Sp}(\mathcal{E}(\rho)) \subset \mathbb{R}^+ \quad (4.38)$$

Complete positivity rather than positivity reflects that considering the density matrix as the reduced density matrix of a larger system does not change that positivity is preserved: extending \mathcal{E} as $\mathcal{E} \otimes I$ to act on the larger space preserves the positivity of density operators of that larger system.

Quantum channels admit different means of representation. We present here the most ubiquitous one: the Kraus operator-sum representation. Quantum channels

admit other representations such as the Choi matrix representation as well as the Pauli Transfer Matrix [58].

Any quantum channel can be decomposed onto Kraus operators $\{E_k\}$ satisfying the completeness relation

$$\sum_{k=1}^K E_k^\dagger E_k = I \quad (4.39)$$

such that

$$\mathcal{E}(\rho) = \sum_{k=1}^K E_k \rho E_k^\dagger \quad (4.40)$$

where K is called the Kraus rank of the quantum channel. The decomposition is not unique.

We present here a few channels corresponding to noise models that are commonly used and that we will resort to in our simulations to study the noise-resilience of our algorithms. We present single-qubit versions from which the multi-qubit counterparts follow naturally.

Amplitude damping Even when idle, the qubit may lose energy to its environment, a general process which may be modelled through the two following Kraus operators:

$$\begin{aligned} E_1 &= \begin{pmatrix} 1 & 0 \\ 0 & \sqrt{1 - p_{\text{AD}}} \end{pmatrix} \\ E_2 &= \begin{pmatrix} 0 & \sqrt{p_{\text{AD}}} \\ 0 & 0 \end{pmatrix} \end{aligned} \quad (4.41)$$

which might read, for instance in our model,

$$p_{\text{AD}}(t) = 1 - e^{-\frac{t}{T_1}} \quad (4.42)$$

with T_1 the characteristic time of spontaneous emission so that

$$\begin{pmatrix} \rho_{11} & \rho_{12} \\ \rho_{21} & \rho_{22} \end{pmatrix} \longrightarrow \begin{pmatrix} 1 + e^{-\frac{t}{T_1}} \rho_{11} & e^{-\frac{t}{2T_1}} \rho_{12} \\ e^{-\frac{t}{2T_1}} \rho_{21} & e^{-\frac{t}{T_1}} \rho_{22} \end{pmatrix}. \quad (4.43)$$

t here refers to the idling time (corresponding to a gate applying on other qubits).

Pure dephasing Another aspect of idle noise is the loss of coherence through the vanishing of the off-diagonal coefficients of the density matrix on a characteristic timescale T_φ :

$$\begin{pmatrix} \rho_{11} & \rho_{12} \\ \rho_{21} & \rho_{22} \end{pmatrix} \longrightarrow \begin{pmatrix} \rho_{11} & e^{-\frac{t}{T_\varphi}} \rho_{12} \\ e^{-\frac{t}{T_\varphi}} \rho_{21} & \rho_{22} \end{pmatrix} \quad (4.44)$$

This process, also known as *pure dephasing*, can be modelled through the following Kraus operators:

$$\begin{aligned} E_1 &= \begin{pmatrix} 1 & 0 \\ 0 & \sqrt{1 - p_{\text{PD}}} \end{pmatrix} \\ E_2 &= \begin{pmatrix} 0 & 0 \\ 0 & \sqrt{p_{\text{PD}}} \end{pmatrix} \end{aligned} \quad (4.45)$$

setting p_{PD} as

$$p_{\text{PD}}(t) = 1 - e^{-\frac{2t}{T_\varphi}}. \quad (4.46)$$

(assuming a flat spectrum, aka white noise).

Usually idle noise in a quantum device is characterized by times T_1 and T_2 : the latter characteristic time corresponds to dephasing, and thus encompasses the effects of both amplitude damping and pure dephasing. This is encapsulated in the formula

$$\frac{1}{T_2} = \frac{1}{T_\varphi} + \frac{1}{2T_1} \quad (4.47)$$

Depolarizing noise Depolarizing noise is commonly used to model errors at the gate level. The idea is to consider that with probability p the gate U applies, whereas with probability $1 - p$ a random Pauli gate applies on top of the gate. The noisy gate U_{noisy} is thus represented as

$$\mathcal{E}_{U_{\text{noisy}}} = \mathcal{E}_{\text{depol}} \circ \mathcal{E}_U \quad (4.48)$$

with

$$\mathcal{E}_U(\rho) = U\rho U^\dagger \quad (4.49)$$

and

$$\mathcal{E}_{\text{depol}}(\rho) = (1 - p)\rho + \frac{p}{3}(X\rho X + Y\rho Y + Z\rho Z) \quad (4.50)$$

which can be interpreted as probability $1 - p$ that nothing occurs, and probability p that a random Pauli gate applies. This corresponds to Kraus operators

$$E_1 = \sqrt{1 - p}I, \quad E_2 = \sqrt{\frac{p}{3}}X, \quad E_3 = \sqrt{\frac{p}{3}}Y, \quad E_4 = \sqrt{\frac{p}{3}}Z. \quad (4.51)$$

Our two-qubit depolarizing model's Kraus operators are all tensor products corresponding to that of the one-qubit model, although the parameter p is different.

Usually, companies building prototypes of universal quantum computers quantify the accuracy of their single and two-qubit gates through so-called *randomized benchmarking* error rates, $\epsilon_{\text{RB}}^{(1)}$ and $\epsilon_{\text{RB}}^{(2)}$. The values of p for the single-qubit depolarizing model as well as that of the two-qubit model can be set to reflect these rates: starting from the relationship between the *average process fidelity* and the coefficient p_0 of the identity in the Kraus decomposition of the channel [59],

$$\mathcal{F}_{\text{ave}} \equiv 1 - \epsilon_{\text{RB}} = \frac{p_0 d + 1}{d + 1}, \quad (4.52)$$

with $d = 2^n$ the dimension of the subspace that is acted on by the channel, we must set p_0 so that

$$p_0 = 1 - \left(1 + \frac{1}{d}\right) \epsilon_{\text{RB}}. \quad (4.53)$$

Applying this formula to the one-qubit process, we get

$$p_1 = \frac{3}{2} \epsilon_{\text{RB}}^{(1)}, \quad (4.54)$$

and for the two-qubit process:

$$p_2 = 1 - \sqrt{1 - \frac{5}{4} \epsilon_{\text{RB}}^{(2)}}. \quad (4.55)$$

Readout errors Finally, errors may occur as the qubit is being measured as well as because the qubit wasn't prepared in the target state. We consider only the former source of error here, considering that during the measurement time T_{meas} the qubit's $|1\rangle$ state might decay to $|0\rangle$. The readout error is modelled through a Positive-Operator Valued Measurement (POVM), namely a measurement in the Z -basis with outcome probabilities $p_0 = \text{Tr}(\Pi_0 \rho)$, $p_1 = \text{Tr}(\Pi_1 \rho)$ where

$$\Pi_0 = \begin{pmatrix} 1 & 0 \\ 0 & \alpha \end{pmatrix} \quad (4.56)$$

$$\Pi_1 = \begin{pmatrix} 0 & 0 \\ 0 & 1 - \alpha \end{pmatrix} \quad (4.57)$$

with $\alpha = 1 - e^{-t_{\text{meas}}/T_1}$.

The form of the Kraus operators can be deduced from the more general framework of Lindblad's master equation. We introduce below the latter as it will prove relevant with regards to our proposal of a noise-assisted impurity solver.

4.5.2 Lindblad master equation

The continuous evolution of open quantum systems is usually described with Lindblad master equation

system type	closed	open
state	$ \psi\rangle, \langle\psi \psi\rangle = 1$	$\rho, \rho^\dagger = \rho, \text{Tr}(\rho) = 1, \text{Tr}(\rho^2) < 1$
master equation	$-i\partial_t \psi(t)\rangle = H(t) \psi(t)\rangle$	$\partial_t \rho(t) = \mathcal{L}[\rho(t)]$ (within hyp.)
evolution	$ \psi\rangle' = U \psi\rangle$	$\rho' = \mathcal{E}(\rho)$
$\langle O \rangle$	$\langle\psi O \psi\rangle$	$\text{Tr}(\rho O)$

Table 4.2: Description of quantum systems. The master equation for open systems referred to here, Lindblad’s equation, relies on several assumptions.

$$\dot{\rho} = -i[H, \rho] + \sum_k \Lambda_k \left(L_k \rho L_k^\dagger - \frac{1}{2} \{L_k^\dagger L_k, \rho\} \right) \quad (4.58)$$

$$= -i[H, \rho] + \mathcal{D}[\rho] \quad (4.59)$$

$$= \mathcal{L}[\rho] \quad (4.60)$$

\mathcal{L} is referred to as the Lindbladian, a quantum channel (completely positive and trace preserving, note that we require $\Lambda_k \geq 0$) whereas \mathcal{D} is the dissipator. Operators L_k are referred to as jump operators.

It must be understood as the evolution equation for the reduced density matrix in interaction representation. It is obtained from the von-Neumann equation by going in the interaction picture, and applying the Born-Markov approximation. This approximation consists in considering the system and its environment (the ‘reservoir’) start and remain in a product state of their respective density matrices, and that the reservoir does not display memory effects. The time locality is implied by the form of the equation, which is first order.

Then, being given the Lindblad operators and solving the master equation, one can deduce the Kraus operators by identifying the solution with

$$\rho(t) \equiv \mathcal{E}(\rho(0)) = \sum_j E_j^\dagger(t) \rho(0) E_j(t) \quad (4.61)$$

Conversely, a Kraus map does not necessarily correspond to a master equation as quantum channels also encompass non-Markovian evolutions.

4.6 Study of the influence of the different noise sources on state preparation

Noise has a strong impact of VQE state preparation. At the beginning of this work, the LDCA circuit was the state-of-the-art variational circuit to prepare correlated fermionic ground states. How do the different sources of noise introduced in the previous section (idle noise, depolarizing noise and readout error) impact instances of LDCA states?

	$\epsilon_{\text{RB}}^{(1)}$	$\epsilon_{\text{RB}}^{(2)}$	$t_{\text{meas}} (\mu\text{s})$	$T_1 (\mu\text{s})$	$T_\varphi (\mu\text{s})$
Reference	0.00304	0.0414	3.42	71.0	123
Depolarizing noise	$\times r$	$\times r$	0	∞	∞
Idle noise	0	0	0	$\times 1/r$	$\times 1/r$
Readout error	0	0	1	$\times 1/r$	∞

Table 4.3: Specifications of IBM Melbourne as of March 2020, and noise rescaling details. r stands for the noise rescaling factor.

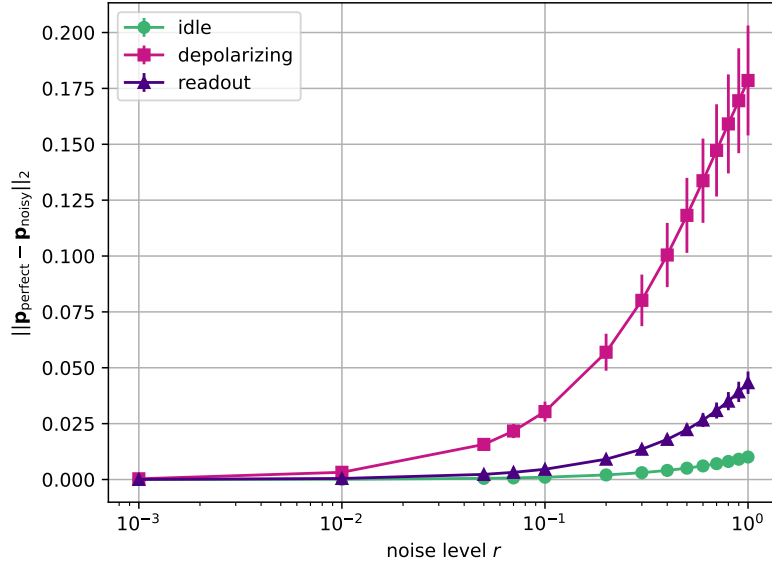


Figure 4.6: Study of the influence of each noise source on the distance of the probability vector $\mathbf{p}_{\text{noisy}} = (\rho_{11}, \rho_{22}, \rho_{33}, \rho_{44})$ to its statevector counterpart, noisefree simulation counterpart. Average over 10 runs corresponding to different random parametrizations of the circuit. The error corresponds to the standard deviation.

We consider here more specifically the one-cycle version of the LDCA circuit [50] on four qubits, in a compressed version using the *lazy synthesis* compilation algorithm [60]. The recompilation relies on an advantageous decomposition of the basic pattern of two-qubit rotation gates in the LDCA circuit. The compressed circuit’s two-qubit gate count is 24 corresponding to CNOT gates, and the number of single-qubit gates is 50. We study the influence of each source of noise separately.

We tune the parameters of the noisy model with respect to the ”actual” value as documented on Table 4.3. These values correspond to IBM Melbourne, one of the quantum computers IBM offered to test quantum algorithms on in 2020, as retrieved from the IBM Quantum Experiment platform at the beginning of the work presented here.

The results of the simulations (averaged over 10 runs, corresponding to 10 random parametrizations of the circuit) are presented Figure 4.6. They show that the most

cumbersome noise source is by far the depolarizing noise: consequently, the first focus of this work was to limit the effect of imperfect gates applications on variational state preparation.

Before presenting the solution we proposed to this end, we conclude this chapter by presenting a light-touch error mitigation technique which we leveraged in some numerical simulations to correct for the value of observables, dubbed *Zero-Noise Extrapolation*.

4.7 Mitigating errors with the Zero-Noise Extrapolation scheme

The NISQ era will end with the advent of error-corrected qubits. Such logical qubits are to be obtained by combining a large number of faulty physical qubits, provided these reach error rates below the error correction threshold.

In the meantime, one can still try to reduce the impact of noise on the evaluation of observables: this is the scope of error mitigation.

Several error mitigation techniques were developed over the past few years. They aim at providing a better estimate $\langle \tilde{O}_{\text{perfect}} \rangle$ for the expectation value of an observable O based on a set of couples $\{x_i, \langle O^{(i)} \rangle\}_i$ where x_i denotes some measurement parameter and $\langle O^{(i)} \rangle$ the expectation value of the observable $O^{(i)}$ associated to x_i .

For instance, x_i might be a multi-index labelling

- which non-Clifford gates of the original circuit are to be replaced by Clifford gates to allow for classical simulability of the modified circuit \mathcal{C}_i
- whether $\langle O^{(i)} \rangle$ corresponding to O over the modified circuit \mathcal{C}_i is estimated with classical simulation or from the hardware

in the context of Clifford Data Regression (CDR [61]) which aims at extrapolating the perfect expectation value from the noisy expectation value by training an ansatz function relating these two quantities over the test set of modified Clifford circuits.

x_i might also refer to a noise-inflation level in the case of Zero-Noise Extrapolation (ZNE), whose details are explained below. In the remainder of this paragraph, I repeat the wording of the section dedicated to the introduction of the ZNE method in Reference [46], which I have co-authored².

Within ZNE, the departure of the observable as measured $\langle O \rangle_{\text{meas}}$ from its noise-free counterpart $\langle O \rangle_{\text{perfect}}$ is assumed to depend on a single parameter, an error rate ϵ_{phys} . Assuming some ansatz for the precise form of how these two are related, one can infer an estimation of $\langle O \rangle_{\text{perfect}}$ from a set of measurements corresponding to

²I was the main contributor to the cited paragraph.

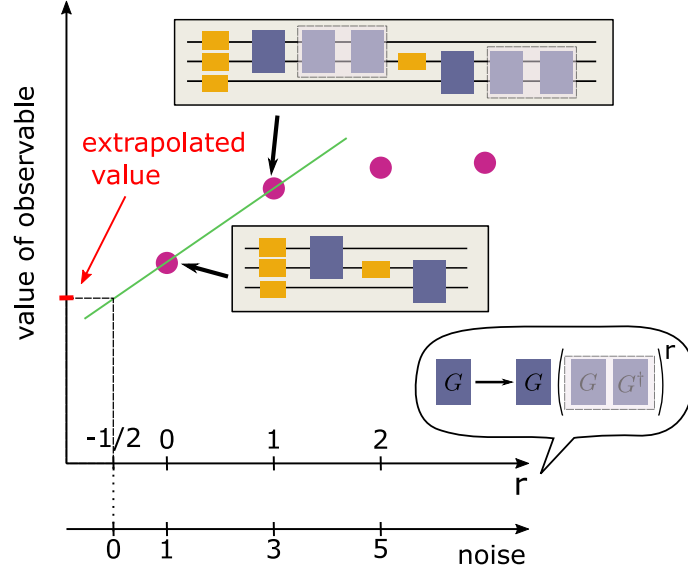


Figure 4.7: Principle of zero-noise extrapolation illustrated with a linear ansatz for inference. Occurrences of two-qubit gates G are followed by a number r of resolutions of the identity $I = GG^\dagger$ to scale the noise to a factor $(2r + 1)$. A noiseless observable value can be inferred from the noisy observables measured on the original circuit and the circuit with $r = 1$ by linearly extrapolating to $r = -1/2$. Image published in Reference [46].

different effective error rates $\epsilon = f(\epsilon_{\text{phys}}, r)$ where r is a tunable parameter.

A ZNE-specific challenge is to find a way to explore different error rates, which depend on the noise processes at play. Typically, the noise to be mitigated is the one stemming from the two-qubit gate of the set, say G , and the 'rescaling' of the error rate is obtained by inserting decompositions of the identity under the form GG^\dagger after each occurrence of G [62]. This process does not change the state encoded by the circuit. However, it makes it more error-prone: under the assumption that a depolarizing channel can model the two-qubit gates errors, r insertions correspond to inflating the (two-qubit gate) error rate from its physical value $\epsilon_{\text{phys}}^{(2)}$ to $\epsilon(r) = (2r + 1)\epsilon_{\text{phys}}^{(2)}$, and a noise-free observable can subsequently be inferred by extrapolating to the $r = -1/2$ regime, see Figure 4.7. Alternatively, one can resort to pulse stretches rather than identity insertions to increase the noise picked along the execution of the circuit [63]: the only underlying assumption is that the noise is time-invariant.

Alleviating the quantum circuit depth burden: Natural-Orbitalization

The NISQ approach to hybrid quantum-classical DMFT relies on variational quantum state preparation with the VQE algorithm. The ansatz circuit must be chosen so it is able to provide a good approximation to the target state, but it should also be short enough so that it does not pick up too much noise when run on the device. Above a certain level of complexity displayed by the target state such as a high degree of entanglement, these two requirements are antagonistic.

Previous state of the art concerning NISQ implementations of hybrid DMFT focused on two-site DMFT or equivalents, in which the auxiliary Anderson impurity model only has a single impurity site and a single bath site [64, 65, 66, 67]. We wanted to tackle two-impurity models in order to improve in the first direction highlighted in section 3.6, that of the size of the impurity cell which dictates the capability to spatially resolve correlation effects. We could not adapt the hardware-efficient circuits which were leveraged in these work to two-impurity, two-bath sites models: their expressibility is buildable upon stacking entangling layers, but this is counteracted by noise effects. Similarly, the LDCA circuit's performances are strongly degraded by noise.

In this chapter, we present a technique developed to enhance the expressibility of variational circuits through single-particle orbital rotations, which enabled to run successfully for the first time a two-impurity embedding scheme in a noisy quantum-classical setting.

The first section of the chapter introduces the concept of single-particle orbitals and more specifically that of natural orbitals, a state-specific set of orbitals we argue has promising properties to limit circuit depths. At the end of this first section, VQE runs in natural orbitals illustrate their power.

Then, two algorithmic methods are introduced. The first one, natural-orbitalization (*NOization*), consists in approximating the sought-after ground state's natural orbitals by carrying out orbital rotations iteratively based on variational approxima-

tions to the ground state. The second one, natural-orbitalizing adaptive VQE (*NOA-VQE*), combines the natural-orbitalization scheme with adaptive circuit construction.

Finally, the results section illustrates the capacity of the NOization scheme to enhance the expressibility of a given parametrized circuit and that of NOA-VQE to reduce circuit depth as orbital rotations are performed.

5.1 Single-particle basis representational freedom

5.1.1 Single-particle orbitals and associated Fock space

In first quantization, within the tight-binding approximation [68] electrons on the atomic lattice can be described from so-called *Wannier functions* [69], the equivalent in solid-state physics of localized molecular orbitals. These wavefunctions are localized around the atomic sites, and do not overlap each other. They decompose into a spatial part and a spin part: each atomic site is thus associated to two Wannier functions corresponding to the two spin species along a quantization axis, \uparrow and \downarrow . Any N -fermion wavefunction over $2M$ Wannier 'spin-orbitals' can be constructed by combining Slater determinants of the form:

$$\psi_{\alpha_1, \alpha_2, \dots, \alpha_N} = \frac{1}{\sqrt{N!}} \sum_{\sigma \in S_N} \varepsilon_\sigma \psi_{\alpha_1}(\sigma(1)) \psi_{\alpha_2}(\sigma(2)) \dots \psi_{\alpha_N}(\sigma(N)) \quad (5.1)$$

where ε_σ stands for the signature of the permutation σ , $\alpha_1, \alpha_2, \dots, \alpha_N$ labels a subset $\{\psi_{\alpha_i}\}$ of the $2M$ Wannier single-particle spin-orbitals, and $\sigma(i)$ refers to which electron occupies the corresponding wavefunction. The summation over all permutations accounts for the indistinguishability of the fermions, whereas the presence of the signature reflects the anticommutation of fermions. Finally, the fact that $\alpha_i \neq \alpha_j \forall i \neq j$ reflects Pauli exclusion principle. The many-electron space is called the *Fock space*.

Second quantization offers a more convenient way to write down multi-fermion states, without having to bother with the indistinguishability and anticommutation of fermions: any state of up to $2M$ electrons can be constructed by combining second-quantized Slater determinants of the form:

$$|n_1 \dots n_{2M}\rangle \equiv (c_1^\dagger)^{n_1} \dots (c_{2M}^\dagger)^{n_{2M}} |0 \dots 0\rangle \quad (5.2)$$

where $n_i \in \{0, 1\}$ stands for the occupation of spin-orbital i (referred to as a *mode*). We will refer to this basis of modes based on Wannier functions as the *site-spin basis*. The number of electrons of such a state is $\sum_i n_i$.

5.1.2 Rotation of the modes

A new basis of modes can be obtained upon transforming the creation/annihilation operators as

$$\tilde{c}_k^\dagger = \sum_p V_{pk} c_p^\dagger \quad (5.3)$$

with V a unitary matrix $VV^\dagger = I$.

How is the Hamiltonian in its second-quantized form, H , affected by the rotation of the modes?

A first answer can be provided at the level of tensors h_{pq} and h_{pqrs} of the second-quantized fermion Hamiltonian introduced in 2.0:

$$\begin{aligned} \mathcal{H} &= \sum_{p,q} h_{pq} c_p^\dagger c_q + \frac{1}{2} \sum_{p,q,r,s} h_{pqrs} c_p^\dagger c_q^\dagger c_r c_s \\ &= \sum_{p'q'} \tilde{h}_{p'q'} \tilde{c}_{p'}^\dagger \tilde{c}_{q'} + \frac{1}{2} \sum_{p'q'r's'} \tilde{h}_{p'q'r's'} \tilde{c}_{p'}^\dagger \tilde{c}_{q'}^\dagger \tilde{c}_{r'} \tilde{c}_{s'} \end{aligned} \quad (5.4)$$

with

$$\begin{aligned} \tilde{h}_{p'q'} &= (V^T h V)_{p'q'} \\ \tilde{h}_{p'q'r's'} &= \sum_{pqrs} V_{pp'} V_{qq'} V_{rr'} V_{ss'} h_{pqrs} \end{aligned} \quad (5.5)$$

A second answer is given by Thouless' theorem [70]. Since V is unitary we can write it as $V = e^R$ where R is a skew-hermitian matrix. Then, the Hamiltonian in the rotated space can be written in *dressed* form, as

$$\tilde{\mathcal{H}} = \mathcal{U}^\dagger \mathcal{H} \mathcal{U} \quad (5.6)$$

with

$$\mathcal{U} = \exp \left(\sum_{pq} R_{pq} c_p^\dagger c_q \right). \quad (5.7)$$

Equivalently, the orbital rotation can be borne at the level of the state:

$$|\tilde{\psi}\rangle = \mathcal{U} |\psi\rangle \quad (5.8)$$

The specific choice of single-particle basis has repercussions on required circuit depth in VQE. Strategies to reduce circuit depth by rotating the modes in favour of that associated to more compact circuits started being explored when this work began, and after. However, they rely on a different mechanics than the one we have put forward, namely they optimize for the basis rotation by classically dressing the Hamiltonian with a parametrized rotation V and optimizing the rotation parameters along the circuit's parameters [71, 72, 73, 74].

Here instead we will aim at leveraging a specific set of single-particle orbitals: Natural Orbitals.

5.1.3 Natural Orbitals

Definition Let $|\psi\rangle$ be a fermionic quantum state. The one-particle reduced density matrix (1-RDM) relative to modes $\{c_i^\dagger, c_i\}_i$ is defined as

$$D_{ij}^{(c)} = \langle \psi | c_i^\dagger c_j | \psi \rangle \quad (5.9)$$

Since $D^{(c)} = (D^{(c)})^\dagger$, it can be diagonalized as

$$D^{(c)} = V n V^\dagger \quad (5.10)$$

with $V V^\dagger = V^\dagger V = I$ and

$$n = \begin{pmatrix} n_1 & & & \\ & n_2 & & \\ & & \ddots & \\ & & & n_M \end{pmatrix} \equiv D^{(\tilde{c})} = \langle \psi | \tilde{c}_i^\dagger \tilde{c}_j | \psi \rangle \quad (5.11)$$

where the n_i 's are the occupation numbers of the so-called *natural orbitals* \tilde{c}_i^\dagger , a terminology introduced by Löwdin [75]. These spin-orbitals are related to the original modes by the rotation matrix V as in Equation 5.3: $\tilde{c}_k^\dagger = \sum_p V_{pk} c_p^\dagger$. Similarly, the diagonal elements of $D^{(c)}$ are occupation numbers of the original c spin-orbitals. Any quantum state which physically is a non-interacting state, that is, a Slater determinant, has natural orbital occupations numbers (NOONs) that are either 0 or 1. Otherwise, Pauli exclusion principle prescribes $0 \leq n_j \leq 1$. Finally, $\sum_j n_j = N$ the number of electrons in $|\psi\rangle$.

Properties Natural orbitals exhibit the property of minimizing the *correlation entropy*

$$S_{\text{corr}} = - \sum_j D_{jj}^{(c)} \log(D_{jj}^{(c)}) \quad (5.12)$$

which is a well-defined quantity since $D_{jj}^{(c)} \equiv n_j^{(c)}$ is the expectation value of the density operator $c_j^\dagger c_j$ over the state, that is the occupancy of mode j which cannot be negative. A proof of this result is presented in Appendix J.

S_{corr} measures the 'skewness' of the orbital occupancies: the lower, the more skewed the distribution. What we mean by skewed distribution is a distribution which concentrates around a portion of its support. A mathematical formulation of the maximal-skewness character of the natural orbital occupancies can be expressed through the Schur-Horn majorization property [76]: the occupancies n_j ordered decreasingly verify

$$\sum_{j=1}^{j_{\text{cutoff}}} n_j^{(\text{NO})} \geq \sum_{j=1}^{j_{\text{cutoff}}} n_j^{(\text{other})}, \quad \forall j_{\text{cutoff}} \leq M. \quad (5.13)$$

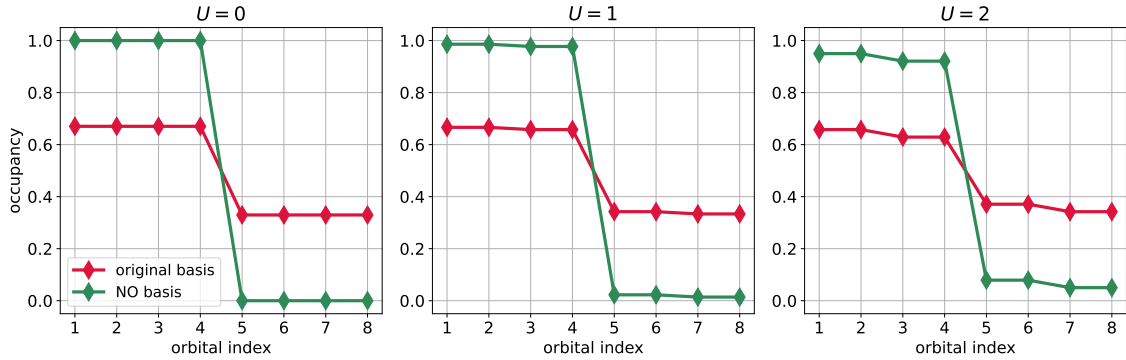


Figure 5.1: Orbital occupancies in the original basis (symmetry-adapted) and in the Natural-Orbital basis for $N_c = 2$ typical embedded models at different levels of Coulomb interaction U .

This is illustrated on Figure 5.1 which displays the occupancies in both the original symmetry-adapted basis +/- leveraged in the RISB scheme (see Appendix K) and in the Natural-Orbital basis for typical two-impurity, two-bath-site embedded models ($D = 0.4, \lambda = 0.04$).

Interest for VQE Working in the NO basis of the state to prepare is appealing for several reasons, which can be listed as follows:

- **State sparsity:** for a non-interacting Hamiltonian, the GS takes the obvious form of a single Slater determinant provided we work in the NO basis. This translates into a minimal state preparation circuit, comprising solely X gates applied to the qubits representing occupied natural orbitals. For a two-fermion system, NOs are also optimal in the sense that truncated CI expansions will achieve maximal fidelity when performed in NOs [77], and the NO transformation can be shown to be the diagonalization basis of the quadratic part of the Hamiltonian. It yields the bonding/antibonding basis, that is, it corresponds to the two-site Fourier transform (see Reference [78]). For other systems, one can often read that the number of Slater determinants in the CI expansion of the wavefunction is minimal when expressed in its NO basis (see for instance the seminal paper by Lowdin [75]). To our knowledge, no formal proof of this property can be found in the literature, although a sketch of the proof is available in Reference [79].
- Also, the Slater determinant corresponding to the filling of the first N natural orbitals (where $N = \text{Tr}D$ is the number of particles) yields a 1-RDM γ which is the closest in trace distance to the true 1-RDM D ($\text{Tr}[(\gamma - D)]^2$ is minimal), see [80]. We stress here how NO differ from the Molecular Orbitals (MO) which are output by the Hartree-Fock procedure [81]: the latter yield the best single-determinantal approximation to the target state according to an energetic criterion. Conversely, NOs are state-dependent and not relative to a Hamiltonian.

- (Quasi)pinning: this is related to state sparsity. NOONs verify some conditions known as Generalized Pauli Constraints (GPC, see Klyachko [82]). These constraints are often saturated (pinned), which strongly limits the type of Slater determinants to appear in the CI expansion. If not pinned, the NOONs of relevant many-fermion states often exhibit quasipinning in that they are close to being pinned (see eg [83, 84, 85]).

Let us expand the last point more. In quantum chemistry, Complete Active Space (CAS) methods are used to reduce the number of configurations to be considered to characterize a wavefunction of interest, for instance the wavefunction associated to the electrons of a given molecule. CAS consists in spotting among, e.g., the Hartree-Fock molecular orbitals which one have occupancies close to 0 or 1. These are said to be *frozen* orbitals, and are treated with mean-field techniques. On the other hand, orbitals with fractional occupancies are called *active* and these solely are treated with many-body methods. The *pinning* phenomenon above encompasses the existence of frozen and active degrees of freedom. Indeed, one of the generalized Pauli constraints is that for every NOON $n_j^{(\text{NO})}$, just as for any occupancy of an orbital in any single-particle basis, one has

$$0 \leq n_j^{(\text{NO})} \leq 1. \quad (5.14)$$

Thus, if this relation is pinned or quasipinned, one has either $n_j^{(\text{NO})} \simeq 0$ or $n_j^{(\text{NO})} \simeq 1$, which eliminates natural-orbital Slater determinants with occupancy of natural-orbital j that differs from 0 or 1 respectively. We expect the state preparation circuit to be reduced accordingly.

Such advantages, and possibly more, can be attained by *optimizing* the orbital basis rather than carrying out, specifically, the rotation to the NO basis: he who can do more, can do less. For instance, truncated FCI expansions in seniority-minimizing bases (minimizing the number of unpaired electrons, that is, the number of single-occupancy orbitals) have been found to yield lower ground state energies of some chemical compounds than the NO basis [86]. Recently, orbital optimization schemes which adapt the single-particle basis on the fly, by optimizing rotation parameters concomitantly with that of the VQE circuit have been set forward [73, 87]. We refer to these strategies as *dressed Hamiltonian* approaches.

Advantage over dressed Hamiltonian approaches These approaches consist in changing the usual VQE cost function

$$E(\boldsymbol{\theta}) = \langle \psi(\boldsymbol{\theta}) | \mathcal{H} | \psi(\boldsymbol{\theta}) \rangle$$

in favour of a basis-dependent cost function

$$E(\boldsymbol{\theta}, \boldsymbol{\kappa}) = \langle \psi(\boldsymbol{\theta}) | \mathcal{U}(\boldsymbol{\kappa})^\dagger \mathcal{H} \mathcal{U}(\boldsymbol{\kappa}) | \psi(\boldsymbol{\theta}) \rangle$$

The optimization of the parameters $\boldsymbol{\kappa}$ of the unitary dressing $\mathcal{U}(\boldsymbol{\kappa})$, which is a Gaussian transformation as introduced in 5.7, does not incur an exponential cost: the number of such parameters scales quadratically, as \mathcal{U} simply reflects a $2M \times 2M$

mode rotation V . The components of κ are actually the matrix elements R_{pq} where $R = \log V$. However, their optimization requires sensitively more computational resources than the sole optimization of circuit parameters θ . Instead, by singling-out the NO basis, we propose an explicit single-particle basis update: no additional classical optimization is added.

Other related techniques In Reference [88], the authors proposed to pre-process the Hamiltonian, e.g. in Jordan-Wigner representation $H = \sum_q \lambda_q P_q$ by optimizing the single-particle basis such that the one-norm $\sum_q |\lambda_q|$ is minimized. The goal is different than ours: the aim is to reduce the number of shots. Indeed, if one is to perform a number $M_q \propto |\lambda_q|$ of measurements to evaluate $\langle \lambda_q P_q \rangle$ with error lower than ϵ , then the total number of shots $\sum_q M_q$ scales as the square of the 1-norm [89]. Our suggestion to 'disentangle' as much as possible the state through orbital rotation bears more resemblance with the so-called *Hamiltonian transcorrelation* technique [90, 91]. Within this technique the Hamiltonian is dressed with a similarity transformation, $\tilde{H} = \mathcal{U}^{-1} \mathcal{H} \mathcal{U}$ rather than an unitary transformation where one would have required $\mathcal{U}^{-1} = \mathcal{U}^\dagger$. As a consequence, the hermiticity of the Hamiltonian is not preserved so that the variational principle does not hold anymore.

5.1.4 Variational circuit optimization within natural orbitals

We assess the interest of working in the natural orbital basis by running VQE in the NO basis of the ground state which is sought after. We recall that the problem which motivated the work reported in this chapter was to find a noise-resilient method to prepare $N_c = 2$ embedded models' ground states. We first consider ansatz design within natural orbitals. Then, we move on to VQE in the original basis and in the NO basis for a custom-made ansatz inspired from entanglement generation in natural orbitals and for the state of the art, highly noise-sensitive LDCA circuit.

Natural-orbital-guided ansatz design Natural orbitals provide a simple framework to think about ansatz design. More specifically, we investigate about the fSim gate (introduced in section 4.1.3) as we aim at preparing half-filled states and this entangling gate is excitation-preserving (the number of particles is conserved) as well as being native to some hardware (Google's). Figure 5.2b displays the effect of the number of similarly-parametrized entangling fSim layers on the NOONs. The chosen parametrization (all angles set to $\pi/4$) enables to show representative results while providing a well-characterized numerical experiment. We observe that in the absence of entangling layers, the circuit prepares an uncorrelated, half-filled state. As entangling layers are introduced, quasi-pinned states are prepared, as more and more NOONs acquiring a fractional character associated with larger correlation entropy. Then, we turn to the effect of the stacking of entangling layers on the diagonal elements of the 1-RDM and on the associated NOONs. The variety of the states achievable within such circuits is now taken into account by considering ten random parametrizations of each circuit instance (from one to four entangling layers). We observe on Figure 5.3 that the NOONs for the ten parametrizations are very similar

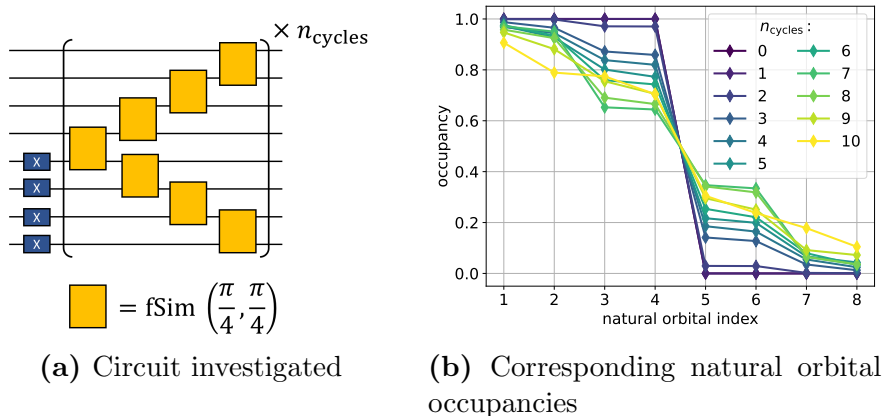


Figure 5.2: Effect of stacking fSim layers on the natural orbital occupancies.

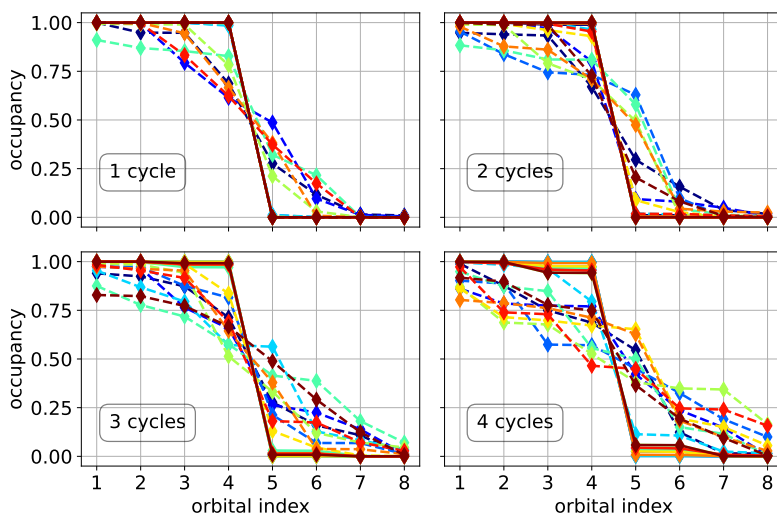


Figure 5.3: Attained orbital occupancies for ten different random parametrizations of a fSim circuit, with different numbers of fSim cycles. Dashed lines: occupancies in site-spin basis, solid lines: corresponding NOONs. The layered structure of the circuits is explicated on Figure 5.2a.

within each case, and that stacking fSim layers increases the number of fractional NOONs. On the other hand, the diagonal entries of the 1-RDM of the states which were prepared exhibit greater variety and tend to get flatter as the number of layers increases. These plots thus confirm the ability to spread the excitations present in a reference state over the different orbitals. Here, a product reference state was used. In the $N_c = 2$ ansatz that we have proposed, the reference state is of multi-reference character: it encompasses several Slater determinants. This choice is physically-motivated and grounded in the $N_c = 1$ case.

Towards a physically-inspired ansatz: Natural Orbitals for $N_c = 1$ embedded model ground states We start from the fact that the ground state of the half-filled single-impurity Anderson model is (see eg the diagonalization of the

Hamiltonian of the Anderson molecule in [92]):

$$|\psi\rangle = \alpha(|0101\rangle + |1010\rangle) + \beta(|1001\rangle + |0110\rangle) \quad (5.15)$$

with notation $|1 \uparrow 2 \uparrow 1 \downarrow 2 \downarrow\rangle$ (spin ordering) and $\alpha, \beta \in \mathbb{R}$, $\alpha^2 + \beta^2 = 1/2$. 1 labels the impurity site and 2, the bath site. Then the 1-RDM reads:

$$D^1 = \begin{pmatrix} \frac{1}{2} & \alpha\beta & 0 & 0 \\ \alpha\beta & \frac{1}{2} & 0 & 0 \\ 0 & 0 & \frac{1}{2} & \alpha\beta \\ 0 & 0 & \alpha\beta & \frac{1}{2} \end{pmatrix} \quad (5.16)$$

To determine the NO basis, we thus have to diagonalize:

$$A = \begin{pmatrix} \frac{1}{2} & a \\ a & \frac{1}{2} \end{pmatrix} \quad (5.17)$$

with $a = \alpha\beta$. The eigenvalues λ_1, λ_2 of A verify

$$\begin{aligned} \lambda_1 + \lambda_2 &= 1 \\ \lambda_1 \lambda_2 &= \frac{1}{4} - a^2 \end{aligned}$$

equivalent to

$$\begin{aligned} \lambda_2 &= 1 - \lambda_1 \\ (\lambda_1 - \frac{1}{2})^2 &= a^2 \end{aligned}$$

so that $\text{Sp}(A) = \frac{1}{2} \pm a = \frac{1}{2} \pm \alpha\beta$. Thus, we have natural occupations $n_+ = \frac{1}{2} + \alpha\beta$ associated with orbitals $\frac{1}{\sqrt{2}} \begin{pmatrix} 1 \\ 0 \\ 0 \\ 0 \end{pmatrix}$ and $\frac{1}{\sqrt{2}} \begin{pmatrix} 0 \\ 0 \\ 1 \\ 1 \end{pmatrix}$, and $n_- = \frac{1}{2} - \alpha\beta$ associated with orbitals $\frac{1}{\sqrt{2}} \begin{pmatrix} -1 \\ 0 \\ 0 \\ 0 \end{pmatrix}$ and $\frac{1}{\sqrt{2}} \begin{pmatrix} 0 \\ 0 \\ -1 \\ 1 \end{pmatrix}$: we recognize, in each spin sector, the bonding/antibonding basis well known in the context of the covalent bond model based on the linear combination of atomic orbitals (LCAO) method.

Also, note that the NO basis is in this case the diagonalization basis of h_{pq} : this is due to the fact that h_{pq} has the same structure as D , more specifically

$$h_{pq} = \begin{pmatrix} \mu & t & 0 & 0 \\ t & \mu & 0 & 0 \\ 0 & 0 & \mu & t \\ 0 & 0 & t & \mu \end{pmatrix} \quad (5.18)$$

Since the transformation does not mix orbitals from different spin sectors, we can consider the two-qubit case. The transformation to the bonding/antibonding basis

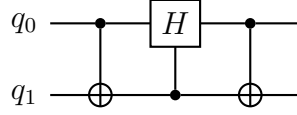


Figure 5.4: Quantum routine allowing to rotate into the bonding/antibonding basis.

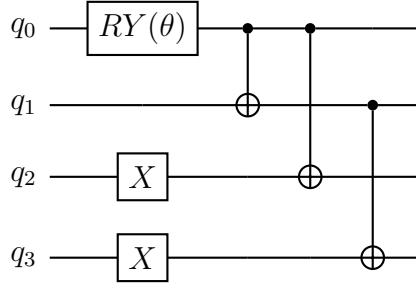


Figure 5.5: Multireference (MR) ansatz for $N_c = 1$ in natural orbitals.

reads

$$\begin{aligned}
 |00\rangle &\rightarrow |00\rangle \\
 |11\rangle &\rightarrow |11\rangle \\
 |01\rangle &\rightarrow \frac{1}{\sqrt{2}}(|01\rangle + |10\rangle) \\
 |10\rangle &\rightarrow \frac{1}{\sqrt{2}}(|01\rangle - |10\rangle)
 \end{aligned}$$

corresponding to the following self-adjoint matrix in the $\{|00\rangle, |01\rangle, |10\rangle, |11\rangle\}$ basis:

$$U = \begin{pmatrix} 1 & 0 & 0 & 0 \\ 0 & \frac{1}{\sqrt{2}} & \frac{1}{\sqrt{2}} & 0 \\ 0 & \frac{1}{\sqrt{2}} & -\frac{1}{\sqrt{2}} & 0 \\ 0 & 0 & 0 & 1 \end{pmatrix} \quad (5.19)$$

This transformation can be implemented at the circuit level, using the routine depicted on Figure 5.4.

The 1-RDM in NO reads (mind the reordering)

$$\begin{pmatrix} n_0 & 0 & 0 & 0 \\ 0 & n_0 & 0 & 0 \\ 0 & 0 & 1 - n_0 & 0 \\ 0 & 0 & 0 & 1 - n_0 \end{pmatrix} \quad (5.20)$$

(with n_0 relabelling n_+).

We consider the circuit depicted in Figure 5.5, drawing inspiration from [93]. Recalling the matrix expression for the RY gate

$$RY(\theta) = \cos(\theta/2)I - i \sin(\theta/2)Y = \begin{pmatrix} \cos(\theta/2) & -\sin(\theta/2) \\ \sin(\theta/2) & \cos(\theta/2) \end{pmatrix} \quad (5.21)$$

We define

$$\alpha = \cos(\theta/2) \quad (5.22)$$

$$\beta = \sin(\theta/2) \quad (5.23)$$

The circuit state reads

$$\begin{aligned} |\psi(\theta)\rangle &= CNOT(1,3)CNOT(0,2)CNOT(0,1)X_3X_2RY(\theta)_0|0000\rangle \\ &= CNOT(1,3)CNOT(0,2)CNOT(0,1)X_3X_2(\alpha|0000\rangle + \beta|1000\rangle) \\ &= CNOT(1,3)CNOT(0,2)CNOT(0,1)(\alpha|0011\rangle + \beta|1011\rangle) \\ &= \alpha|0011\rangle + \beta|1100\rangle \end{aligned}$$

corresponding to the one-particle reduced density-matrix (1-RDM) $D_{ij}^1 \equiv \langle \psi | c_i^\dagger c_j | \psi \rangle$

$$D^1 = \begin{pmatrix} |\beta|^2 & 0 & 0 & 0 \\ 0 & |\beta|^2 & 0 & 0 \\ 0 & 0 & |\alpha|^2 & 0 \\ 0 & 0 & 0 & |\alpha|^2 \end{pmatrix} \quad (5.24)$$

Let

$$\theta_0 = 2 \arcsin \sqrt{n_0} \quad (5.25)$$

$\theta_0 \in [0, \pi]$ because $0 \leq n_0 \leq 1$. Then by choosing

$$\theta = \pm \theta_0 (+\pi) \quad (5.26)$$

where the sign can be tuned and a translation of π can be included, one can reach the 1-RDM 5.20 through a state $\alpha|0011\rangle + \beta|1100\rangle$ whose amplitudes are real numbers α, β so that $|\beta|^2 = n_0, |\alpha|^2 = 1 - n_0$ and with signs either $(+, +), (-, -), (+, -), (-, +)$.

If one appends to the MR circuit the two transformations corresponding to each spin sector, one obtains an exact circuit in the original basis equivalent to the one used in Ref[94].

Using the MR circuit as a primitive, we have proposed a $N_c = 2$ ansatz dubbed the *Multi-Reference Excitation Preserving* (MREP) ansatz, represented on Figure 5.6 (a). It starts with a multi-reference state preparation part, obtained as the MR circuit being applied to each of the two {impurity + bath} subsystems. This first block thus provides a NOON baseline with particle-hole symmetry. Then, the two subsystems are connected through layers of 'fan' fSim-gate entangling routines that spread the excitations among the natural orbitals, as in circuit 5.2a.

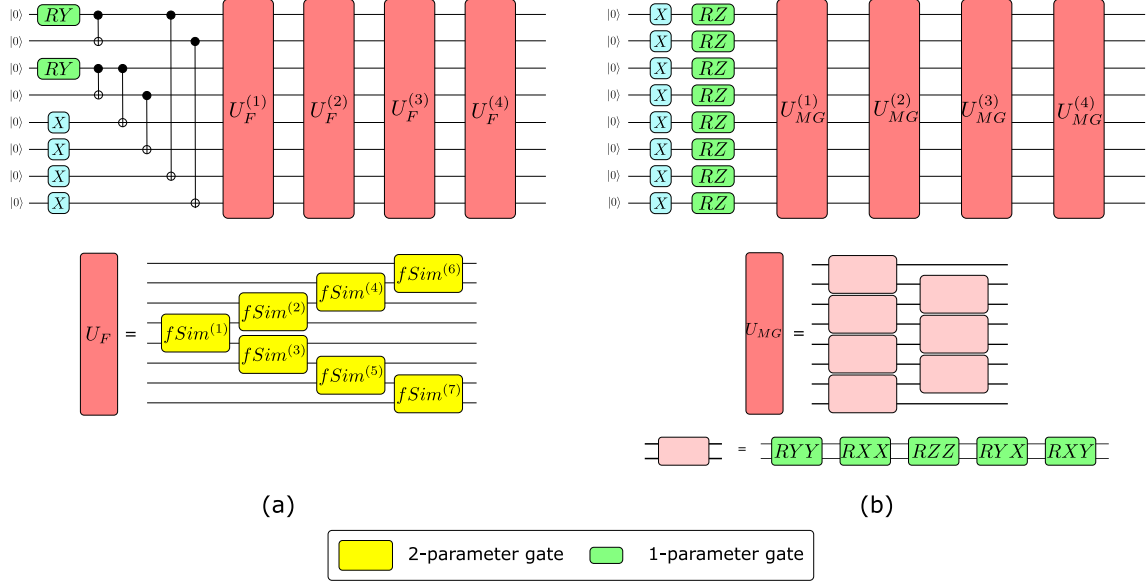


Figure 5.6: Circuits investigated for the ground state preparation of $N_c = 2$ embedded models. (a) Multi-Reference Excitation Preserving (MREP) circuit. (b) Eight-qubit, one-cycle Low-Depth Circuit Ansatz (LDCA) circuit.

VQE in NO The Hamiltonians considered here describe two impurities embedded in a two-site bath, whose parameters correspond to that returned at the end of a classical RISB loop for different values of the Coulombic interaction U (0, 1 and 2).

The circuits considered here are:

- the compressed version of the one-cycle LDCA circuit (see sections 4.4.1.2 and 4.6 for respectively, the description of the circuit’s structure and a word on the compilation method) and Table 5.2 for the characteristics of the circuit), which is taken as a state-of-the-art reference
- our shallow, custom-made *Multi-Reference Excitation Preserving* ansatz

Both circuit structures are depicted on Figure 5.6.

VQE runs in the original, symmetry-adapted basis are compared with runs in the true NO basis of the ground state. More specifically, upon diagonalizing the Hamiltonian, we find the target ground state $|\psi_0\rangle$. In the cases considered here, the ground state is not degenerate. We then compute the 1-RDM $D_{ij} = \langle \psi_0 | c_i^\dagger c_j | \psi_0 \rangle$ and diagonalize it as $D = VnV^\dagger$. Rotating the Hamiltonian accordingly as $\tilde{H} = \mathcal{U}^\dagger H \mathcal{U}$ where \mathcal{U} is the transformation in the Fock space reflecting the single-particle basis rotation V , we obtain a new expression for the Hamiltonian to be measured within Jordan-Wigner encoding, and consider VQE runs aiming at minimizing this new Hamiltonian.

We observe on Figure 5.7 what seems to be a systematic improvement of the results, as measured by the converged energy. For expressive enough circuits such as

LDCA, we observe a speed-up in the convergence, in accordance with recent results suggesting orbital rotations could result in favourable optimization landscapes [87].

These results motivate an approach based on Natural Orbitals. However, being state-specific, the Natural Orbital basis is not known prior to the ground state determination, calling for schemes which allow to compute relevant orbital basis updates, guided by the 1-RDM.

5.2 Methods

5.2.1 Natural-Orbitalization algorithm

Because we aim at finding the ground state, its natural orbital basis is generally also unknown. An exception is the case of two-electron systems, where the NO basis is given by the two-site Fourier transform. Otherwise, we can rotate to the NO basis of a converged VQE state, and go on iteratively, interspersing VQE runs with orbital rotations. We dubbed this algorithm *Natural-Orbitalization*.

More specifically, the algorithm goes as follows:

1. carry out a first VQE optimization of the ansatz circuit in the original basis (typically, the site-spin basis), this yields a state $|\psi(\boldsymbol{\theta}^*)\rangle$
2. compute the 1-RDM elements associated to the converged state, namely $D_{ij} = \langle \psi(\boldsymbol{\theta}^*) | c_i^\dagger c_j | \psi(\boldsymbol{\theta}^*) \rangle$
3. classically diagonalize this 1-RDM to get the NO associated to $|\psi(\boldsymbol{\theta}^*)\rangle$
4. transform the Hamiltonian's terms accordingly, namely as in Equation 5.5
5. repeat the procedure, now measuring the Hamiltonian as written in the current NO basis

A schematic depiction of the algorithm is proposed on Figure 5.10. The algorithm deforms the variational manifold so as to increase the capacity of the ansatz to approximate correctly the target state, as represented on Figure 5.8. In practice this is achieved due to the fact that the quantum circuit gets off-loaded of the task of carrying out orbital rotations, as illustrated on Figure 5.9.

Note that such an iterative scheme was implemented classically [95]. As far as hybrid quantum-classical schemes are concerned, it is comparable in spirit with the *Perm-VQE* algorithm [96]. Within Perm-VQE, the spin-orbitals ordering is updated according to how they correlate in the converged variational state: the qubit pairs whose *mutual information* (a measure of pairwise entanglement) is high are mapped to neighbouring qubits. The rationale is that mutual information reflects entanglement, which in the absence of proper remapping needs to be built 'across' qubits, that is, necessitates two-qubit gates that do not reflect physical entanglement but rather transfer entanglement up to the corresponding qubit. Similarly, our

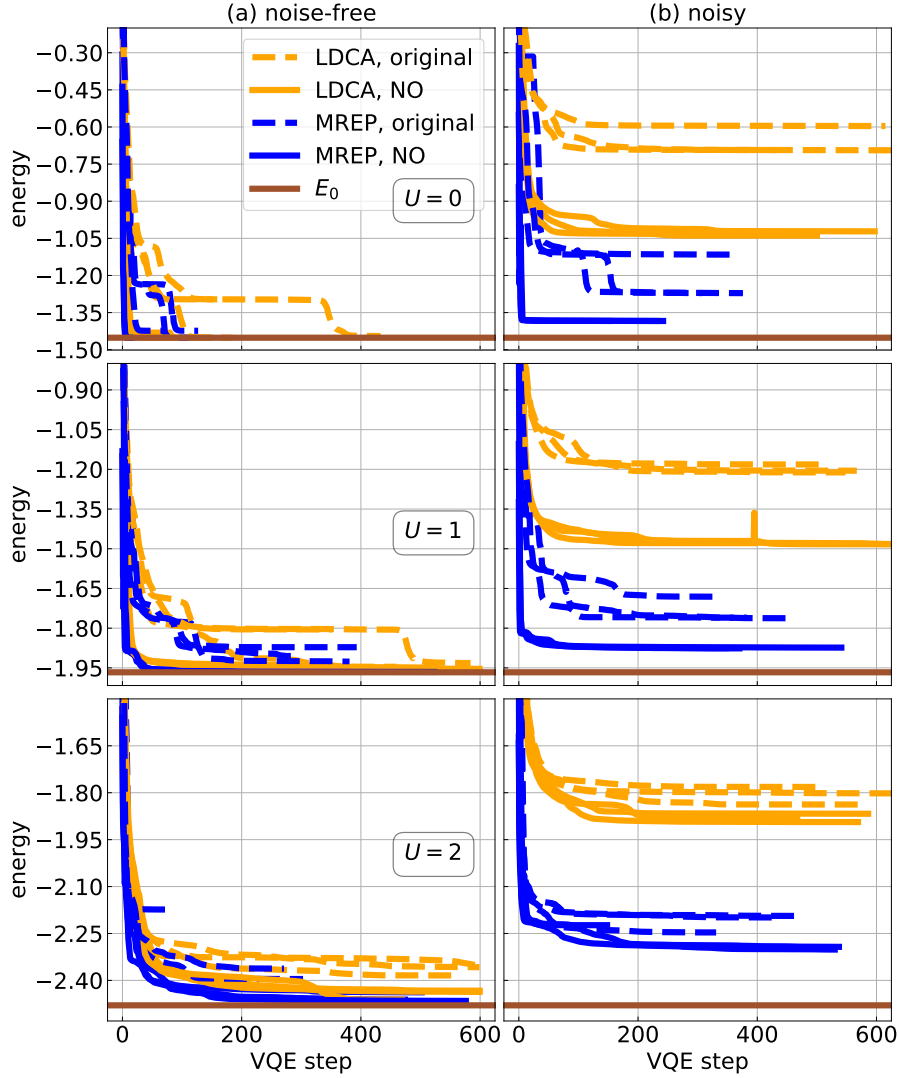


Figure 5.7: Comparison between runs in the original, site-spin basis (dashed lines) and in the NO basis (solid lines), with and without noise, for two-impurity converged embedded Hamiltonians, at different levels of Coulombic interaction U . The ansätze considered are the one-cycle compressed LDCA circuit and the MREP ansatz, whose structures are explicated in Figure 5.6. Each VQE optimization is repeated three times, with different random initializations so as to highlight sensitivity to the initialization. The VQE optimization is carrying out allowing for up to 10000 steps of the BFGS algorithm.

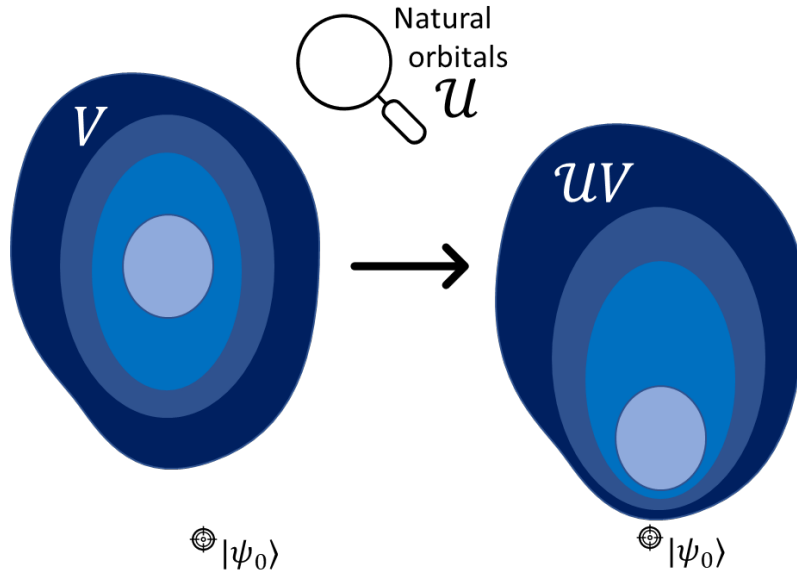
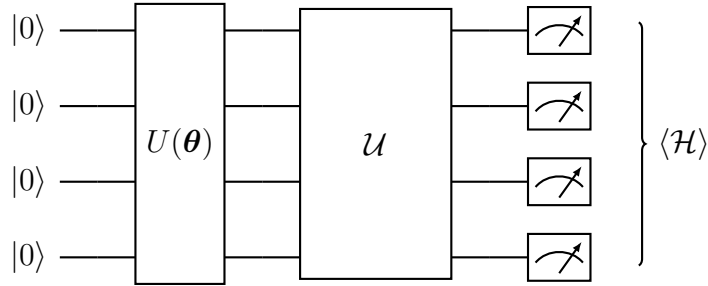


Figure 5.8: Illustration of the capability of the transformation to natural orbitals, \mathcal{U} , to enhance the expressibility of a variational ansatz manifold V . The different shades of blue represent different degrees of complexity corresponding to different parametrizations of the circuit, from product states in light blue to the most entangled states of the manifold in deep blue.

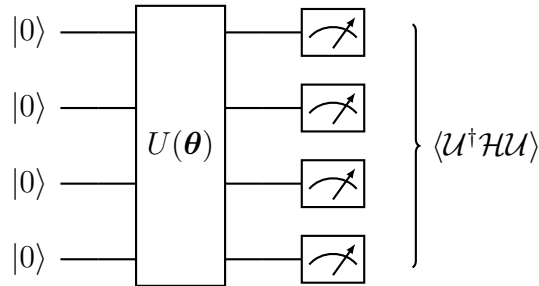
scheme aims at reducing circuit depth by eliminating the need for entanglers to be part of the circuit only to, on a more fundamental level, carry out single-particle basis rotations. This comes with a measurement overhead.

Overhead The measurements of the 1-RDM elements do not incur any overhead, as they are actually part of the measured elements to compute the energy of the converged VQE state. The diagonalization of this matrix comes with a small cost $O((2M)^3)$. The price to pay for reduced gate count is that rotating the basis typically wipes out the sparse character of the Hamiltonian. Further VQE optimizations thus incurs a larger measurement overhead as there are more Pauli words to be measured. This implies that there is a measurement/noise trade-off to be considered when selecting a strategy between the 'off-chip' method – Natural-Orbitalization – and the on-chip method, for instance employing the LDCA circuit.

We show in 5.3.1 that the expressibility of ansatz circuits does indeed increase with the NOizing scheme. The method allowed to approximately prepare ground states of two-impurity embedded models at satisfactory levels to converge a slave boson loop in the presence of simulated gate noise [97], as presented in section 5.3.3. In the case of a single-impurity slave boson scheme, we leveraged the NO basis through a minimal-depth circuit, attaining precisions above the previous art 5.3.4.



(a) On-chip orbital rotation strategy. The single-particle orbital rotation is performed at the chip level, and Pauli strings of \mathcal{H} are measured to access the energy of the variational state.



(b) Off-chip orbital rotation strategy. The single-particle orbital rotation is not performed at the chip level, but rather 'dresses' the Hamiltonian: Pauli strings of $\mathcal{U}^\dagger \mathcal{H} \mathcal{U}$ are measured to access the energy of the variational state.

Figure 5.9: Different strategies to modify the scope of a variational ansatz $U(\theta)$ through a single-particle orbitals rotation whose effect on the states is represented with the unitary \mathcal{U} . The strategies differ in the associated overheads: strategy 5.9a, in which \mathcal{U} is implemented with quantum gates, comes with a gate overhead whereas strategy 5.9b, where the effect of \mathcal{U} is included in the measurement process, incurs a measurement overhead as typically \mathcal{U} does not preserve the sparsity of \mathcal{H} .

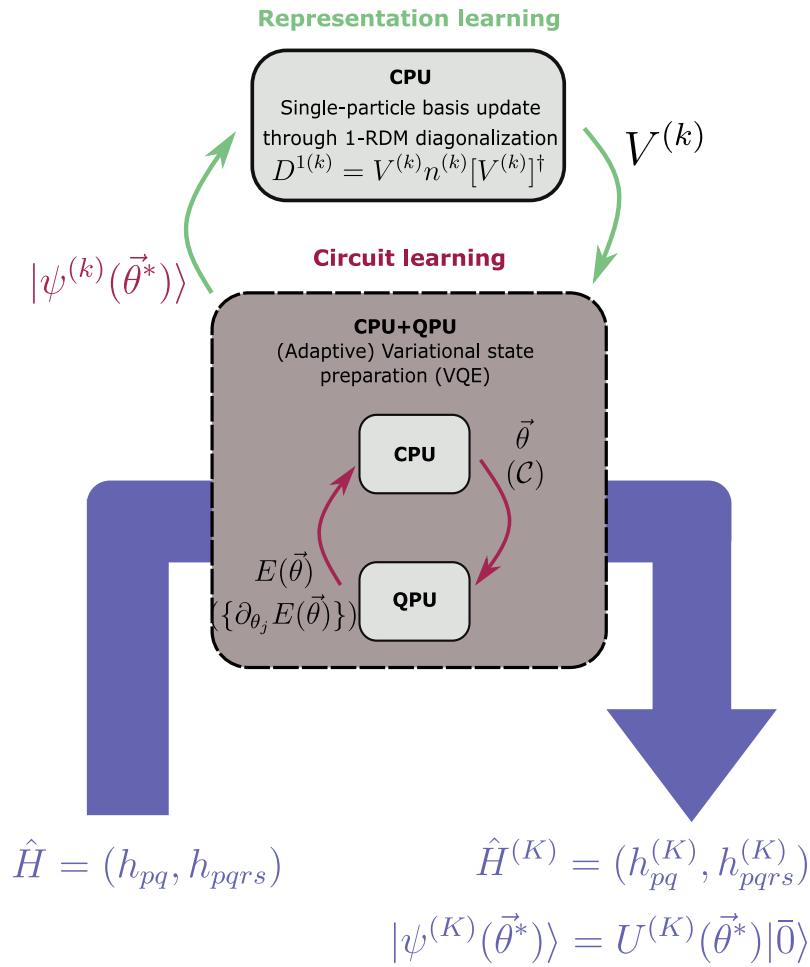


Figure 5.10: Principle of the Natural-Orbitalization algorithm, as well as the Natural-Orbitalizing Adaptive VQE (NOA-VQE) scheme.

5.2.2 Natural-Orbitalizing Adaptive Variational Quantum Eigensolving scheme (NOA-VQE)

The Natural-Orbitalization algorithm aims at making most of a circuit at hand by changing the representation basis of the Hamiltonian. However, ideally one would like to reduce the gate count of variational circuits. We have designed a second algorithm which enables us to do so. It is based on an adaptive VQE scheme.

Adaptive VQE scheme: ADAPT-VQE VQE has been adapted to an ansatz-free setting, in which the circuit is constructed on the fly: this defines the class of ADAPT-VQE (Adaptive Derivative-Assembled Pseudo-Trotter ansatz VQE) algorithms [98].

The ADAPT-VQE algorithm starts with the following:

- a reference state $|\Psi\rangle$ in which the circuit is initialized (usually, a product state),
- a pool of hermitian operators P_j , from which stem parametrized unitaries $e^{iP_j\theta_j}$ which will be considered for addition to the circuit.

Then, it goes as follows:

- given the current state $|\psi^{(k)}\rangle = U_k(\theta_k^{(k)})\dots U_1(\theta_1^{(k)})|\Psi\rangle$ of the circuit, measure the gradients associated to each operator of the pool

$$\partial_{\theta_j}\langle\psi^{(k)}|e^{-iP_j\theta_j}\mathcal{H}e^{iP_j\theta_j}|\psi^{(k)}\rangle|_{\theta_j=0} = i\langle\psi^{(k)}|[\mathcal{H}, P_j]|\psi^{(k)}\rangle \quad (5.27)$$

- set U_{k+1} to the operator associated with the highest-magnitude gradient and run VQE on ansatz $|\psi(\boldsymbol{\theta})\rangle = U_{k+1}(\theta_{k+1})U_k(\theta_k)\dots U_1(\theta_1)|\Psi\rangle$ to optimize all the circuit's parameters to their converged value $\theta_1^{(k+1)}, \dots, \theta_{k+1}^{(k+1)}$.
- repeat until a stopping criterion was met (either convergence, or exhausted budget)

Depending on the type of operators selected to form the pool, ADAPT-VQE comes in different flavours. We present the main ones in the context of Jordan-Wigner encoding:

- fermionic ADAPT-VQE, the original version of Ref [98]: the pool then consists in excitations of fermionic form, e.g. single $c_i^\dagger c_j + \text{h.c.}$ and double $c_p^\dagger c_q^\dagger c_r c_s + \text{h.c.}$ excitations, that is, they are thought of as fermionic Hamiltonians. For instance, one can consider any such non-spin-mixing excitations. The fermionic Hamiltonians are mapped onto spin Hamiltonians within Jordan-Wigner encoding, and the corresponding unitary is implemented. Exact implementations of these operators, which are those appearing in the (trotterized) UCCSD ansatz (see section 4.4.1.2), are known [99]. This original proposal is rooted into the high expressibility of the UCCSD ansatz and aims at reducing the gate count by retaining a fraction of the operators constituting the UCCSD ansatz by selecting them iteratively in a problem-tailored fashion.

- qubit ADAPT-VQE [100] further breaks down the operators by considering as pool operators the individual Pauli strings in the qubit-encoded fermionic excitation operators. The pool is thus more fine-grained at the expense of possibly more parameters to optimize.
- qubit-excitation based [101] also strips down the operators stemming from fermionic excitations, but instead of atomizing them as in qubit-ADAPT-VQE, it proceeds by removing the Z chains in the Jordan-Wigner representation of the fermionic excitations. This approach offers a compromise between the two previous one.

Qubit ADAPT-VQE can *a priori* provide the lowest gate count, we thus retained it for the implementation of our proposed Natural-Orbitalizing Adaptive Variational Quantum Eigensolving (NOA-VQE) scheme.

NOA-VQE algorithm This second algorithm is similar to NOization, except that the VQE steps are replaced with ADAPT-VQE steps. As such, it enters the scope of the schematic diagram of Figure 5.10, where it corresponds to the case when the CPU in the 'circuit learning' block picks a circuit \mathcal{C} along with parameters to test for, based on gradient estimates $\{\partial_j E(\boldsymbol{\theta})\}$. Note that the circuit is not optimized along the parameters, but at each outer step of adaptive growth of the circuit.

Our implementation considers the pool of single-qubit operators X, Y, Z and two-qubit operators $XY, YX, XX + YY$ and ZZ . It goes more specifically as follows:

1. optimize the $\prod_j RY_j$ to get a reference state, this state will be fixed as the circuit grows as opposed to being re-optimized along
2. carry out a first ADAPT-VQE optimization of the ansatz circuit in the original basis (typically, the site-spin basis), this yields a state $|\psi(\boldsymbol{\theta}^*)\rangle$
3. compute the 1-RDM elements associated to the converged state, namely $D_{ij} = \langle \psi(\boldsymbol{\theta}^*) | c_i^\dagger c_j | \psi(\boldsymbol{\theta}^*) \rangle$
4. classically diagonalize this 1-RDM to get the NO associated to $|\psi(\boldsymbol{\theta}^*)\rangle$
5. transform the Hamiltonian's terms accordingly, namely as in Eq 5.5
6. update the set of commutators between the Hamiltonian and pool operators
7. repeat the procedure, now considering optimization with regards to the Hamiltonian as written in the current NO basis

5.3 Results

In what follows, we emulate noisy runs using the depolarizing noise model introduced in 4.5.1 with depolarizing probabilities rendering the following randomized

benchmarking errors

$$\epsilon_{\text{RB}}^{(1)} = 0.16\%, \quad (5.28)$$

$$\epsilon_{\text{RB}}^{(2)} = 0.6\%. \quad (5.29)$$

which correspond to Google’s ‘Sycamore’ superconducting chip as documented in the supplementary material of Reference [1].

Unless specified otherwise, shot noise is not accounted for as well as any other source of noise.

5.3.1 Natural Orbitalization at work: expressivity enhancement

On Figure 5.7 we compared VQE runs in the original basis and in the NO basis for the solving of relevant (with regards to the RISB procedure) two-impurity embedded models. Since the LDCA circuit is ruled out by noise, we focus on the MREP ansatz and carry out the Natural-Orbitalization algorithm. The final VQE energies attained along the orbital update procedure are represented on Figure 5.11. We observe that in just a few Natural-Orbitalization steps (from three to five) similar energies to that attained in the true NO of the target state are achieved, which validates the iterative approach. Note that due to the fact these plots are not purely monotonic, we retain in the Natural-Orbitalization algorithm the setting having yielded the lowest energy, which might or might not correspond to the last VQE run.

We now turn to more systematic tests of the Natural-Orbitalization procedure. They consist in preparing the ground states of Hubbard Hamiltonians, either under the form of the Hubbard dimer (two sites, which map onto four qubits) or the ‘Hubbard plaquette’, that is four sites in a square lattice setting (representing eight qubits). We set the reference of the energies through $t = 1$ and consider both the uncorrelated $U = 0$ and $U = 1$ cases, with and without depolarizing noise. The ansatz circuits considered are the LDCA circuit in its one-cycle, compressed version as well as the simple product ansatz $\prod_j RY_j(\theta_j) |\bar{0}\rangle$ and a fSim-gate-based ansatz with a single layer of fSim gates. These circuits are represented on Figure 5.12, and their specifications are listed in Table 5.1 (resp. Table 5.2) for the four-qubit (resp. eight-qubit) circuits. The VQE optimizations were done with the COBYLA minimizer, and initialized at random. The single-particle basis at first is the site-spin basis Hubbard Hamiltonians are routinely written into. Raw VQE results are presented on Figures 5.13 and 5.14 and display a nearly-systematic improvement of the energy along the procedure. The NO energies, corresponding to VQE runs in the true NO basis¹, are marked as brown solid lines, and are most often attained or nearly attained in just a few Natural-Orbitalization steps. There are exceptions for the smaller, dimer system in the case of the product system, these might be related to

¹Note that the ground state of the Hubbard plaquette at $U = 0$ is degenerate, and the reference NO basis considered is the diagonalization basis of the average of the ground states’ 1-RDM.

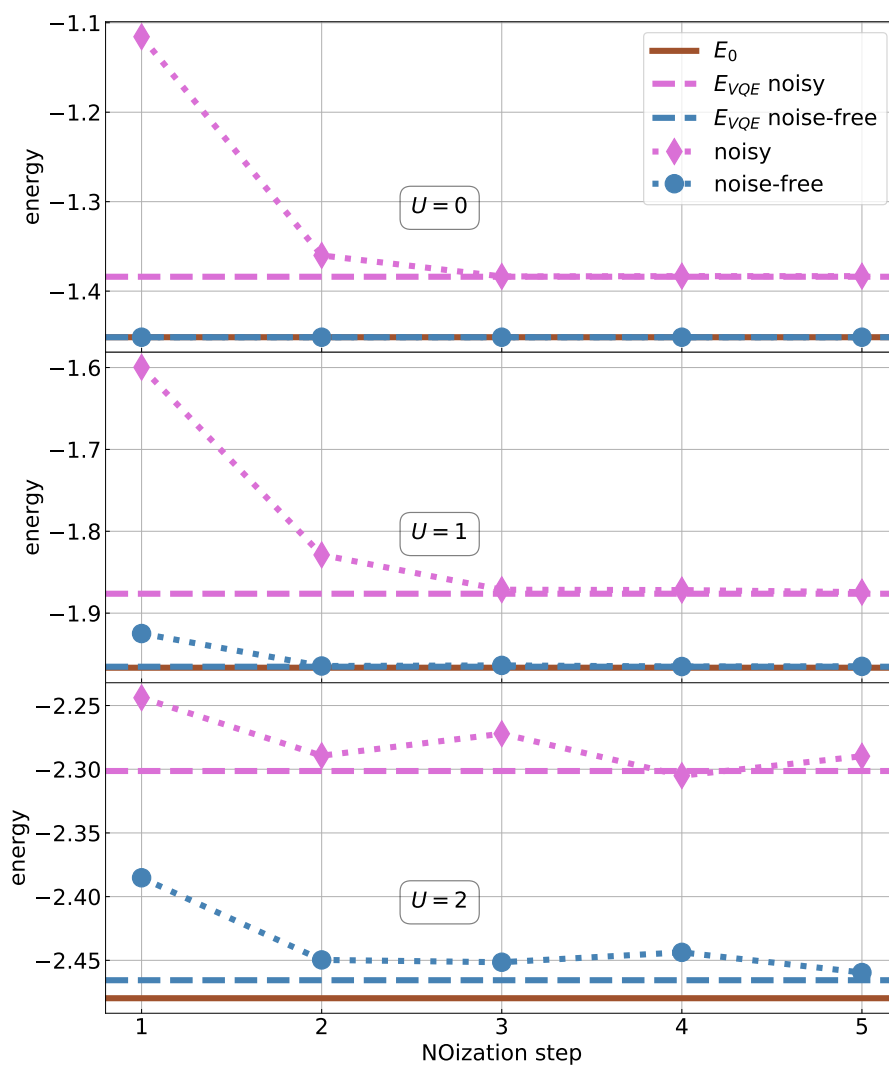


Figure 5.11: Converged VQE energies along the Natural-Orbitalization procedure for two-impurity converged embedded Hamiltonians, at different levels of Coulombic interaction U , within the MREP ansatz. For each case the NO energy reference corresponds to the best run of Figure 5.7.

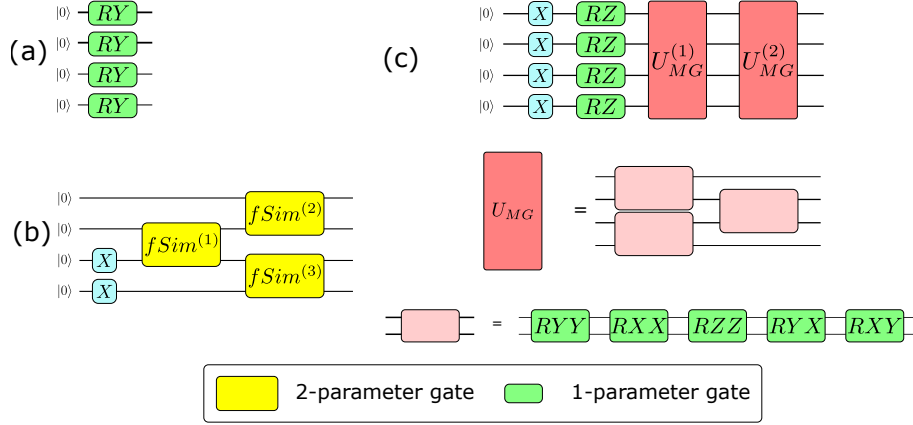


Figure 5.12: Circuits investigated within the Natural-Orbitalization algorithm. (a) Product circuit. (b) fSim circuit. (c) Four-qubit, one-cycle Low-Depth Circuit Ansatz (LDCA) circuit.

Ansatz \ Counts	Product	fSim (one cycle)	LDCA (one cycle, compressed)
Single-qubit gates	4	4	50
Two-qubit gates	0	3	24
Parameters	4	6	34

Table 5.1: Characteristics of the four-qubit circuits used within the Natural-Orbitalization algorithm.

sensitivity to initialization.

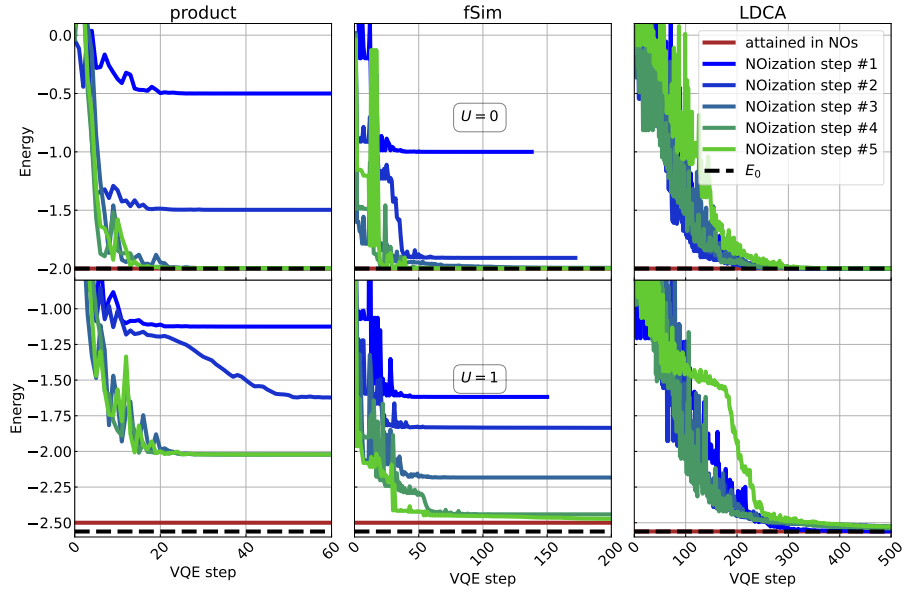
As a conclusion, these results demonstrate the relevance of the Natural-Orbitalization algorithm to make most of a given circuit.

5.3.2 Effect of the Natural-Orbitalization algorithm onto the geometry of the single-particle orbitals: an example

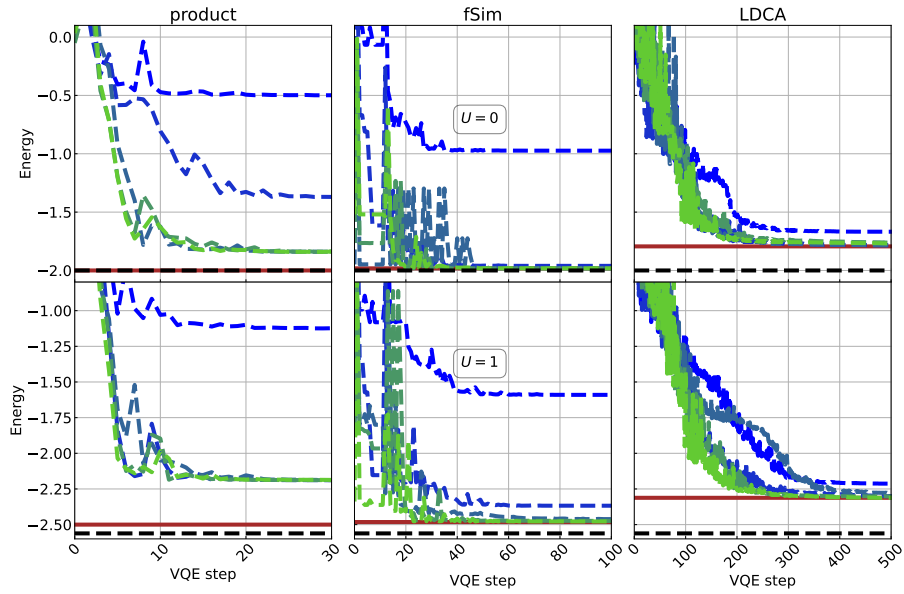
As an illustrative example of the way the single-particle orbitals evolve along the Natural-Orbitalization algorithm, we plot on Figure 5.16 the profiles of the spin-orbitals along the procedure for the Hubbard dimer at $U = 1$. These orbitals corre-

Ansatz \ Counts	Product	fSim (one cycle)	LDCA (one cycle, compressed)
Single-qubit gates	8	4	212
Two-qubit gates	0	7	112
Parameters	8	14	148

Table 5.2: Characteristics of the eight-qubit circuits used within the Natural-Orbitalization algorithm.

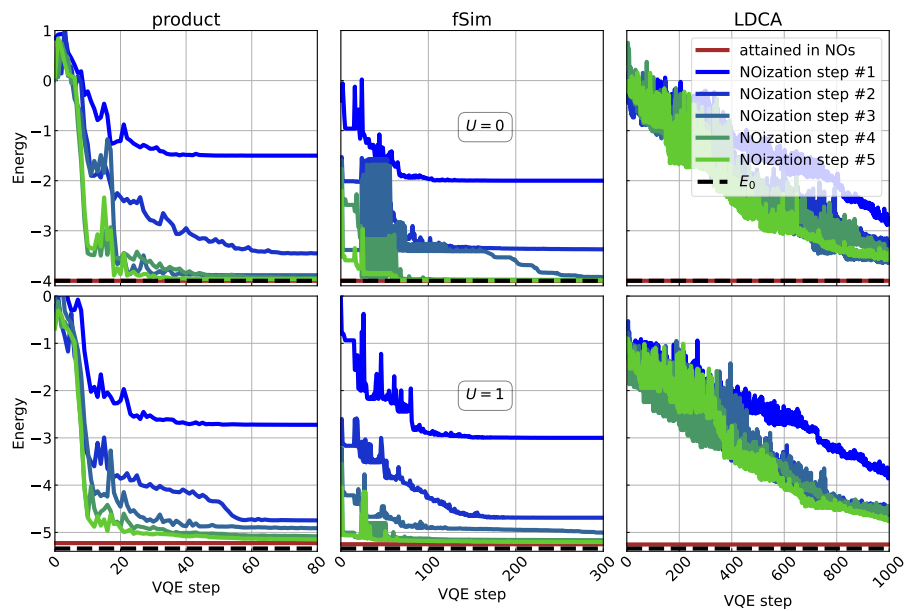


(a)

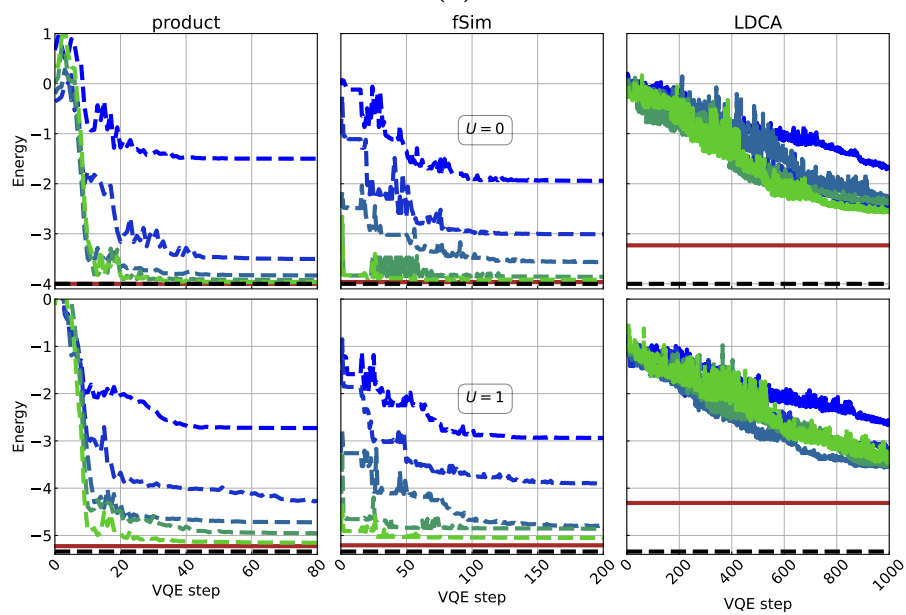


(b)

Figure 5.13: VQE traces within the Natural-Orbitalization algorithm applied to the ground state preparation of the Hubbard dimer, with (bottom) and without (top) depolarizing noise.

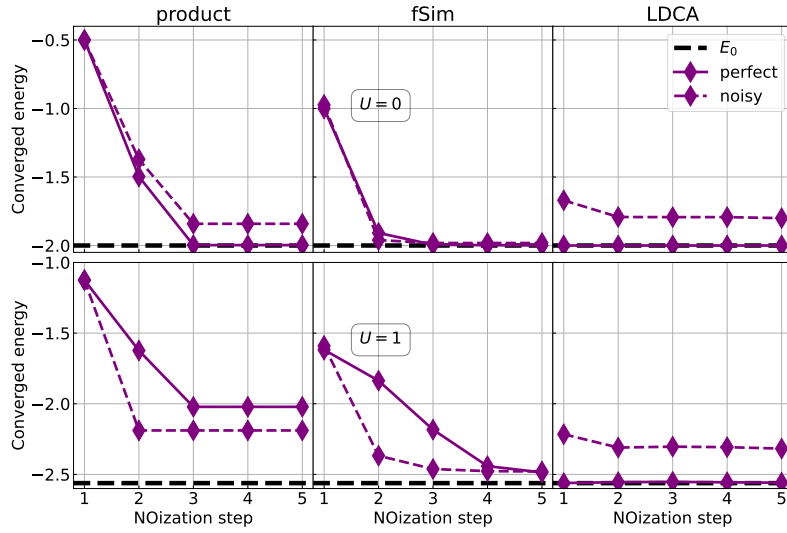


(a)

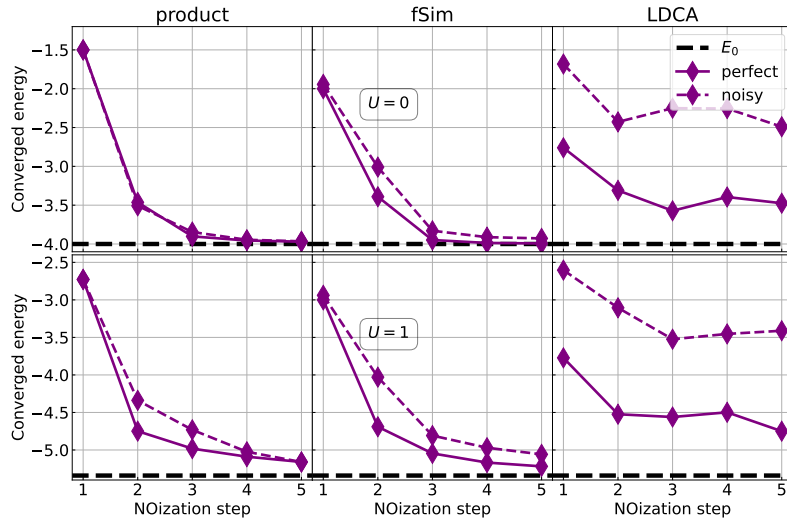


(b)

Figure 5.14: Same as 5.13, but for the Hubbard plaquette.



(a)



(b)

Figure 5.15: Converged VQE energies along the Natural-Orbitalization procedure for the Hubbard dimer (top) and the Hubbard plaquette (bottom), with (dashed lines) and without (solid lines) depolarizing noise. These plots present the final energies attained in the plots of Figure 5.13 and 5.14.

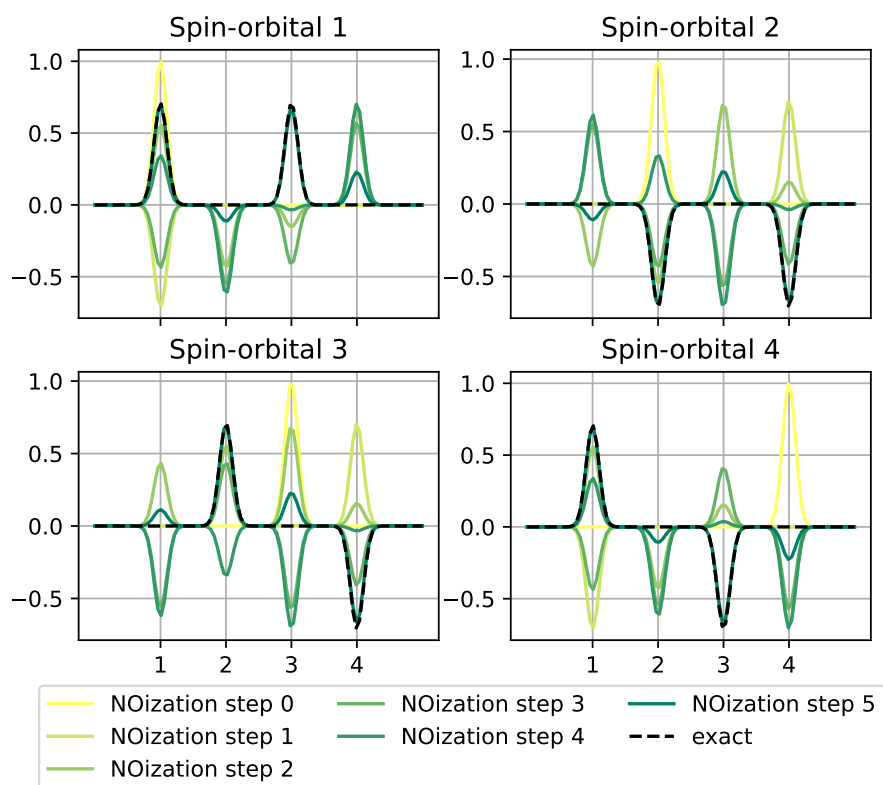


Figure 5.16: Evolution of spin-orbitals along the NOization procedure for the Hubbard dimer at $U = 1$.

Single-particle basis \ Model	Hubbard dimer	Hubbard plaquette
Site-spin	4/6	16 / 20
Natural Orbitals	12/12	388/388

Table 5.3: Number of Pauli terms in Jordan-Wigner representation of Hubbard Hamiltonians, for $U = 0$ (value on the left) and $U = 1$ (value on the right).

spond to linear combinations of the original spin-orbitals which are site-localized but were widened as gaussian functions for visualization purposes. Spin-orbital indices 1 and 2 correspond to the first site whereas indices 3 and 4 correspond to the second site, with a similar ordering of the spin species. We observe that in each spin sector we retrieve the bonding-antibonding basis with minor irregularities, confirming the ability of the procedure to propose relevant basis updates.

The drawback of going to Natural-Orbitals, or in general to divert from the localized basis, is an increase in the number of terms to be measured in the Jordan-Wigner-encoded Hamiltonian, as illustrated in Table 5.3 for the Hubbard model with two and four sites. However, at current noise levels this still constitutes an advantageous strategy rather than relying on deeper circuit ansätze.

5.3.3 Natural-Orbitalized two-impurity slave-boson scheme

We have successfully implemented a hybrid quantum-classical version of a rotationally-invariant slave-boson scheme with impurity cluster size $N_c = 2$, a size which had not been attained before. This corresponds to two impurities and two bath sites, which map within Jordan-Wigner encoding onto eight qubit. The paramagnetic phase at half-filling is tackled. The RISB embedding scheme was introduced in 3.7 and specifics about the two-impurity case are detailed in Appendix K. The method is rendered hybrid in our implementation in that we consider VQE (more specifically, Natural-Orbitalization) on noisy devices for the task of solving the embedded model. The whole scheme is depicted on Figure 5.18. Note that to reduce computation time, we actually implemented a 'NOized scheme' rather than a truly 'NOizing' one, in that we classically computed the Natural-Orbitals and ran VQE in these, exact orbitals rather than carrying out the iterative process of the Natural-Orbitalization algorithm.

We consider an iterative scheme which runs from $U = 0$ to larger values of U by taking as initial guess of (R, λ) for value U_{k+1} at step $k+1$ the converged parameters (R^*, λ^*) at U_k . Here, we only consider three points ($U = 0.05, 1$ and 2) initialized with classically converged parameters at $U = 0.05$.

The RISB embedding relies on an outer optimization loop which aims at converging the embedded model's parameters, namely matrices \mathcal{D} and λ^c . We solve the root formulation of the slave-boson Lagrange equations, as in e.g Reference [30]. Namely,

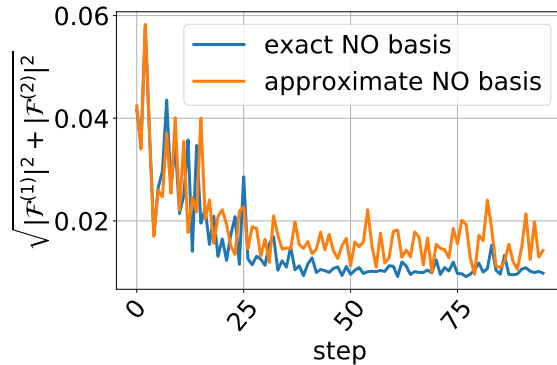


Figure 5.17: Cost function along the RISB loop for $N_c = 2$ at $U = 1$ within either MREP-ansatz based variational ground state preparation (labelled as 'exact NO basis'), or MREP-ansatz based Natural-Orbitalizing ground state preparation (labelled as 'approximate NO basis').

we seek to find the roots R and λ of the two functions

$$\mathcal{F}^{(1)}[R, \lambda] \equiv \langle \Phi | f_\beta f_\alpha^\dagger | \Phi \rangle - \Delta_{\alpha\beta}^p, \quad (5.30a)$$

$$\mathcal{F}^{(2)}[R, \lambda] \equiv \langle \Phi | c_\alpha^\dagger f_\beta | \Phi \rangle - R_{\gamma\alpha} \left[(\Delta^p (1 - \Delta^p))^{1/2} \right]_{\gamma\beta}, \quad (5.30b)$$

where $\mathcal{F}^{(1)}$ and $\mathcal{F}^{(2)}$ depend implicitly on R and λ . The computational bottleneck of the root-solving procedure is the solution of the impurity model, Equation (3.24d) that is needed to compute the 1-RDM elements $\langle \Phi | f_\beta f_\alpha^\dagger | \Phi \rangle$ and $\langle \Phi | c_\alpha^\dagger f_\beta | \Phi \rangle$ and then $\mathcal{F}^{(1)}$ and $\mathcal{F}^{(2)}$. Whereas it is usually solved with a classical impurity solver (for instance, by exact diagonalization of H_{emb}), we propose to solve it approximately using the hybrid quantum-classical VQE method combined with the NOization procedure. Due to the errors in the solving of the embedded model (arising from the simulated noisy VQE approach) being found detrimental to the root solving procedure, the root problem is turned back into a minimization problem with cost function $C = \sqrt{|\mathcal{F}^{(1)}|^2 + |\mathcal{F}^{(2)}|^2}$. We use the Nelder-Mead minimizer as it exhibits noise-resilience properties.

The results are summed up on Figure 5.20. In the inset, the non-convergence of the minimization scheme for the LDCA ansatz illustrates the ruling out of this ansatz at current noise levels. On the other hand, convergence is retained in the case of the noisy MREP ansatz in Natural Orbitals. Converged values of the quasiparticle weight Z and of the static self-energy shift $\tilde{\lambda}$ are relatively qualitatively accurate in the sense that there is a clear separation from the single-impurity case, and correlations acquire a spatial resolution. These results should remain valid in the context of genuine Natural-Orbitalization: in Figure 5.17 we plot the evolution of the cost function along the RISB loop at $U = 1$ for the NOized scheme as well as for the genuine NOization scheme and observe that the NOizing scheme converges in a similar fashion.

Nevertheless, the lowest- U results are unsatisfactory considering the relative simplicity of preparing ground states with low degrees of correlation. The NOized MREP

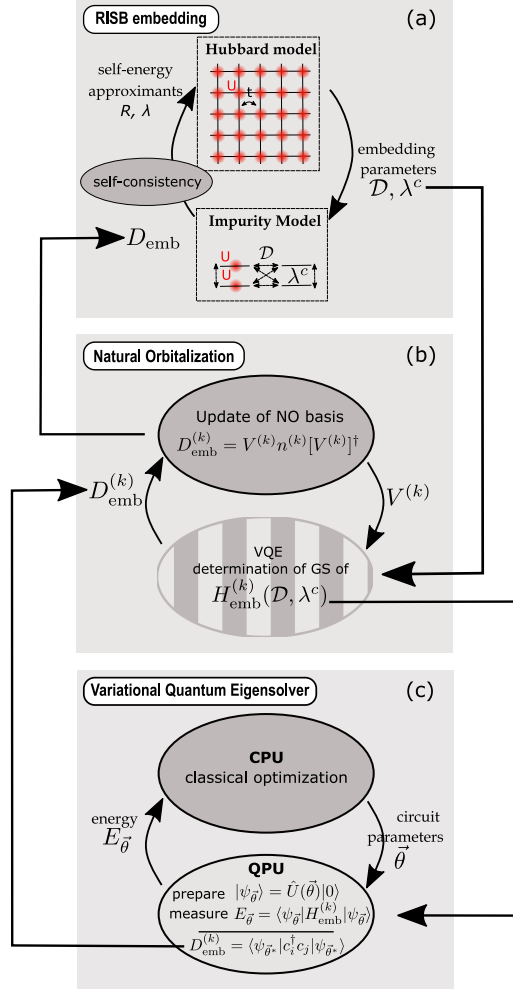


Figure 5.18: Hybrid NOized RISB scheme. The upper panel describes the RISB embedding scheme. The solving of the impurity model, which incorporates computations over a QPU in our hybrid implementation, is described by the two lower panels. It consists in a VQE scheme topped with single-particle orbital updates.

ansatz strategy seems ill-advised as the ansatz is too deep with regards to the requirements at this level of U . These results hint at the relevance of an adaptive strategy rather than the fixed-circuit strategy that was adopted here, which is what the NOA-VQE scheme consists of. Results for that latter scheme are presented in section 5.3.5.

Before considering adaptive ansatz construction strategies, we demonstrate that the fixed-circuit NOization strategy also enabled to boost the accuracy of a $N_c = 1$ slave boson scheme compared with previous state of the art. This example is also presented because as a two-electron problems it allows for an exact circuit representation in NO.

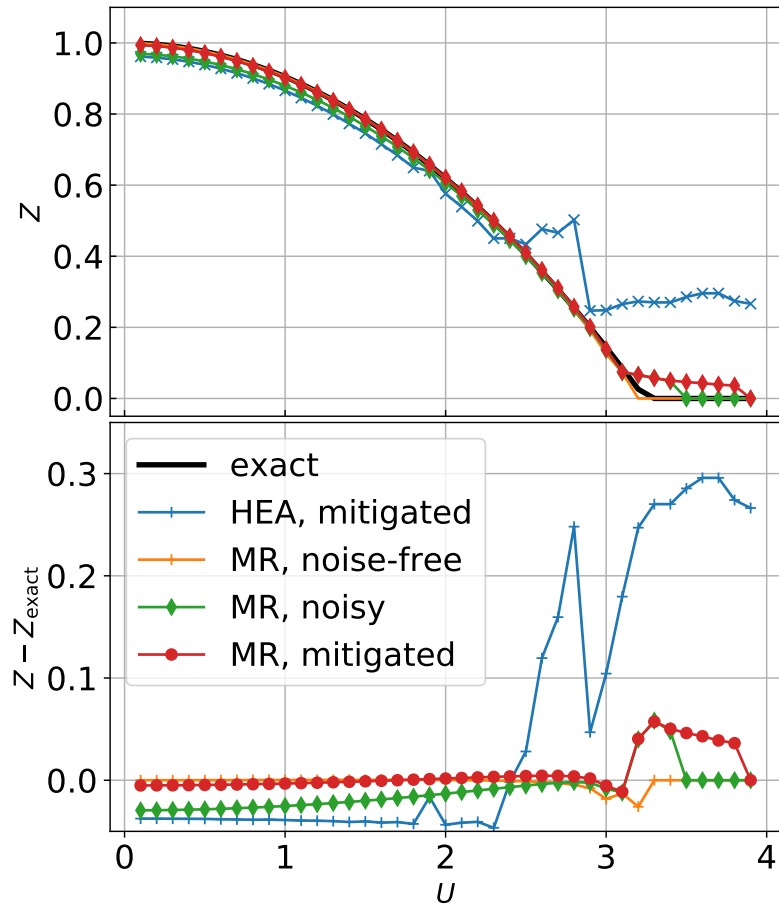


Figure 5.19: Evolution of the quasiparticle weight Z as a function of the Coulombic interaction U within a slave-boson loop for one impurity. Mitigated results correspond to zero-noise extrapolated results within a linear extrapolation scheme.

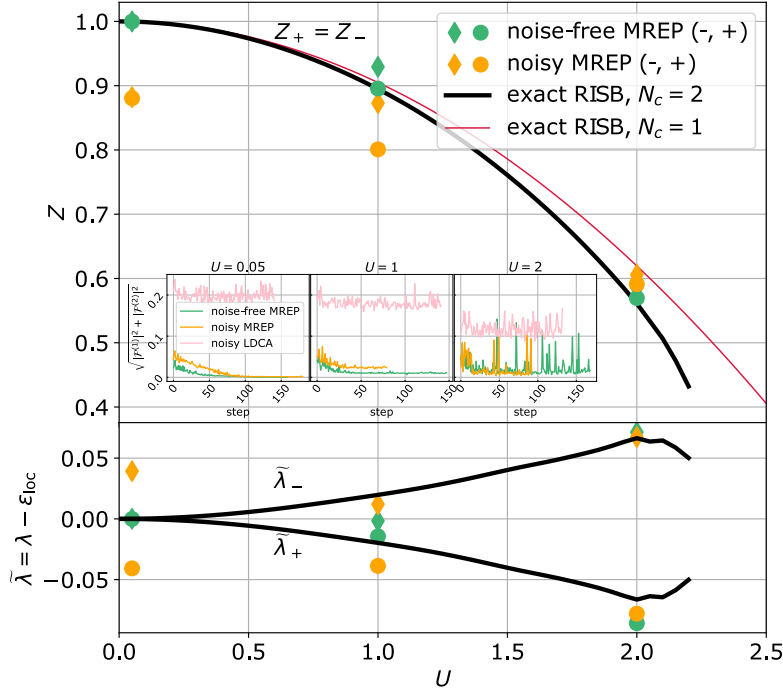


Figure 5.20: Convergence of the slave-boson scheme for different values of U with $N_c = 2$.

5.3.4 Single-impurity slave-boson scheme

We consider a paramagnetic, half-filled $N_c = 1$ embedding scheme. This two-electron case is enlightening to understand the interest of NOization – although here we do not rely on NOization *per se*, and was fully expanded in paragraph 5.1.4.

In this case, the transformation to the NO basis corresponds to the bonding/antibonding basis between the impurity site and the bath site in each spin sector, whichever the embedded model’s parameters. This transformation can be implemented on the chip, or off the chip. Remarkably, for this simple system when the NO basis is implied, it is easy to come up with an *exact*, single-parameter state preparation circuit, which we dubbed the *Multi-Reference* (MR) ansatz. The single-parameter nature of the circuit as well as the precise form of the gate which carries the parameter (a *RY* gate) further cuts the need for proper optimization, as the parameter-shift rule can be leveraged to find the optimal parameter from three distinct energy measurements. Details about parameter-shift-based optimization can be found in 4.4.1.3.

These results shed light on the successful implementation of two-site DMFT schemes with a quantum computer, which could rely on very shallow hardware-efficient ansatz (HEA) circuits which as we see, can even be simpler: working in NO brings about a small gate count reduction, increasing the overall performances of the scheme.

This is illustrated on Figure 5.19 where the quasiparticle weight at convergence is plotted against U both within raw noisy simulation and within Zero-Noise extrap-

olation, a light-touch error mitigation technique (in its simplest, linear form from a single additional measurement on a circuit with inflated noise, see 4.7). We observe high accuracy with the MR ansatz away from the Mott transition, which is also better captured compared with the Hardware-Efficient Ansatz (HEA) of [65], an eight-qubit circuit which was state of the art for the task at that time. Note that whereas the NO basis has a simple analytical form in this case, the plots with the MR ansatz were done in the NO basis associated to a converged VQE state (with the HEA ansatz circuit) minimizing the energy over an embedded Hamiltonian with parameters $U = 0$, $\mathcal{D} = -0.4$, $\lambda^c = 0.004$ typical of that encountered within RISB at low U .

5.3.5 Circuit-depth reduction with NOA-VQE

We consider reference states of the form $\prod_j RY_j(\theta_j)$, as attempts to start from a $\prod_j (X_j)^{\delta_j} |\bar{0}\rangle$ ansatz with the correct number $\sum_j \delta_j = M$ of particles (where M is the number of sites, and since we are considering half-filling) were not successful.

We consider the pool of single-qubit rotations and XY , ZZ and $XX + YY$ operators. The rationale behind the choice of two-qubit pool operators is to provide a particle-number preserving two-body excitation through $XX + YY$, a non particle-number preserving two-body excitation through XY (as we have a reference state which may not have the correct number of particles) and a density-density interaction through ZZ . This is explained in greater detail in Appendix L. The $XX + YY$ and XY excitations are present for all qubit pairs whereas the ZZ excitations are only considered for pairs of qubits indexed as $2k, 2k + 1$, reflecting the ordering as $1 \uparrow, 1 \downarrow, 2 \uparrow, 2 \downarrow \dots$ in the initial basis, so as to limit the count of pool operators. This is all the more so crucial that due to the Hamiltonian being transformed, the commutators between the Hamiltonian and pool operators must be updated after each single-particle basis rotation.

The NOA-VQE method is applied to find the ground state of the half-filled Hubbard plaquette at $U = 0$ and $U = 1$ (with $t = 1$), which is one of the two models considered to demonstrate expressivity enhancement with the Natural-Orbitalization algorithm in section 5.3.1. The optimization of the growing circuit instances are made with the COBYLA minimizer which is allowed a 10000 iteration budget. The initialization is set to the converged parameters of the gates that were present in a previous adaptive step whereas the parameter of the freshly-added gate is initialized to zero, in conformity with the rationale underlying the operator selection criterion. The results are plotted on Figure 5.21 and show dramatic reductions in circuits depths for a given energy threshold as the orbital rotations are carried out. In the presence of noise, in the last NOA-VQE steps addition of operators is found detrimental as noise picked along these deeper circuits degrade the performances.

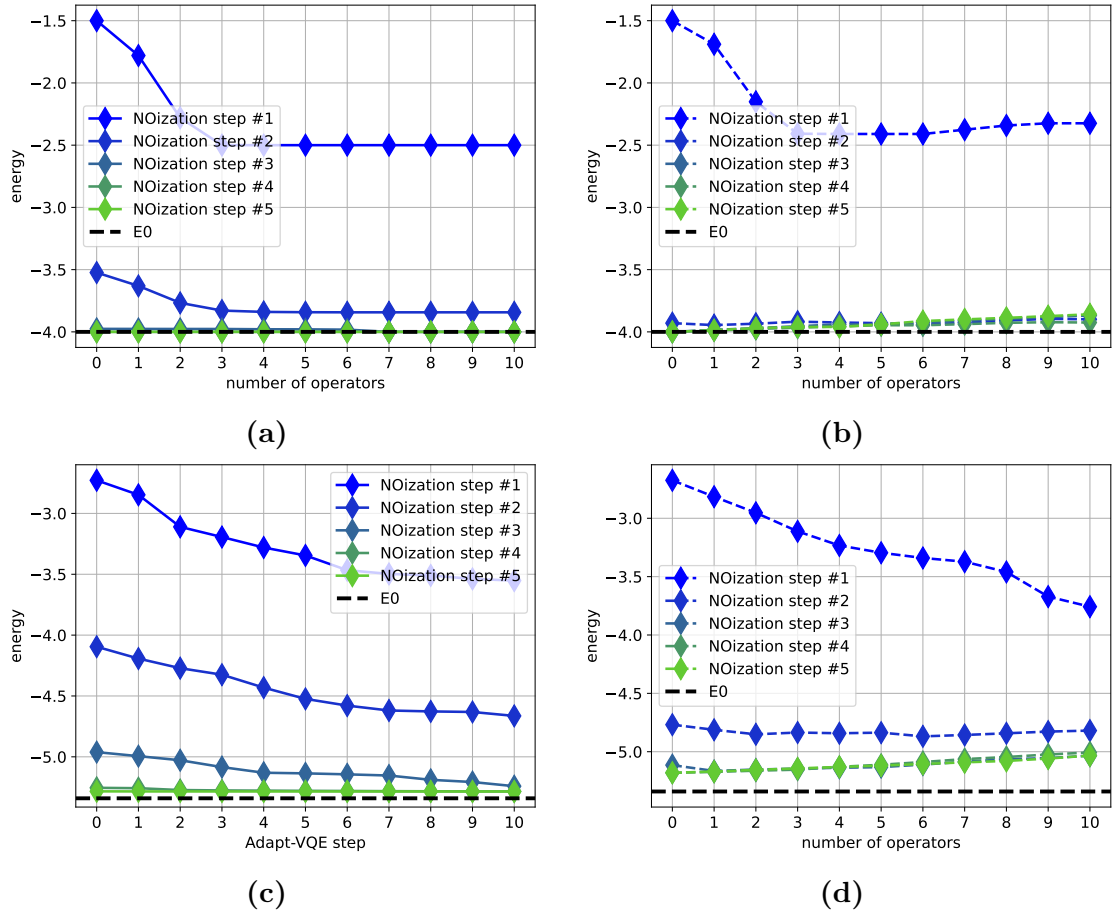


Figure 5.21: NOA VQE for Hubbard plaquette at $U = 0$ (top) and $U = 1$ (bottom), with (right, dashed lines) and without (left, solid lines) depolarizing noise.

5.4 Conclusion

This chapter's scope was to address circuit depth requirements for the variational ground state preparation of correlated many-body systems in order to accommodate noise levels representative of the NISQ era.

All in all, we proposed an iterative single-particle basis update scheme on top of the VQE algorithm which relies on the one-particle reduced density matrix (1-RDM) of the current converged variational state to dictate a new basis to rotate into for a subsequent VQE run. More specifically, the proposed algorithm consists in rotating onto the diagonalization basis of the 1-RDM, which constitutes the Natural Orbital basis of the converged variational state. The method contrasts with now widely explored orbital optimization schemes which continuously update the basis, putting the orbital optimization on an equal footing with that of the ansatz circuit's parameters. Our proposal is less measurement-heavy than these latter approaches, while offering a simple way to boost the expressibility of the circuit at hand. Evidence of this increase in the expressibility are provided, and leveraged to obtain spatial correlations through a slave-boson embedding scheme with two-impurity cells. Additionally, an adaptive version of the algorithm is investigated and demonstrates the ability of the orbital update scheme to reduce circuit depths.

Leveraging decoherence: dissipative bath approach to impurity solving

In the previous chapter, we saw how to reduce the depth of variational circuits to reach a given accuracy in the ground state preparation step of impurity solving. This corresponded to addressing the first limitation of DMFT, the impurity cluster size. The second limitation is the size of the bath. One needs a large number of bath sites to correctly fit the hybridizations that come up in a DMFT loop.

Here, we propose to use the noise inherent to current quantum devices as a resource to reduce the number of bath sites necessary to reach a given accuracy in the fit of a DMFT hybridization.

The chapter begins by presenting the motivation and the foundations for this noise-leveraging approach. We then introduce Keldysh formalism to tackle out-of-equilibrium many-body systems. It is within this formalism that the equations justifying the approach are stated afterwards. The form of the auxiliary hybridizations the scheme provides us with is then laid out. We then assess, for a set of toy equilibrium hybridizations at different temperatures, the quality of the fit as a function of the number of dissipative bath sites and the intensity of their dissipation. This allows us to spot regimes where a significant reduction of the size of the bath is achieved. Finally, since the dissipative processes considered here are not strictly that of qubit noise models, we compare the dynamics brought about by these two types of models in order to validate the portability of the devised approach to a quantum computing framework.

6.1 Philosophy

Exact diagonalization (ED) approaches to impurity solving are hindered by the harsh bath truncation that is necessary to indulge in for tractability. Indeed, the very limited number of bath sites severely limits the capacity to accurately fit the hybridization in the DMFT loop. Similarly, the traditional approach to hybrid quantum-classical DMFT relies on the Hamiltonian formulation of the impurity

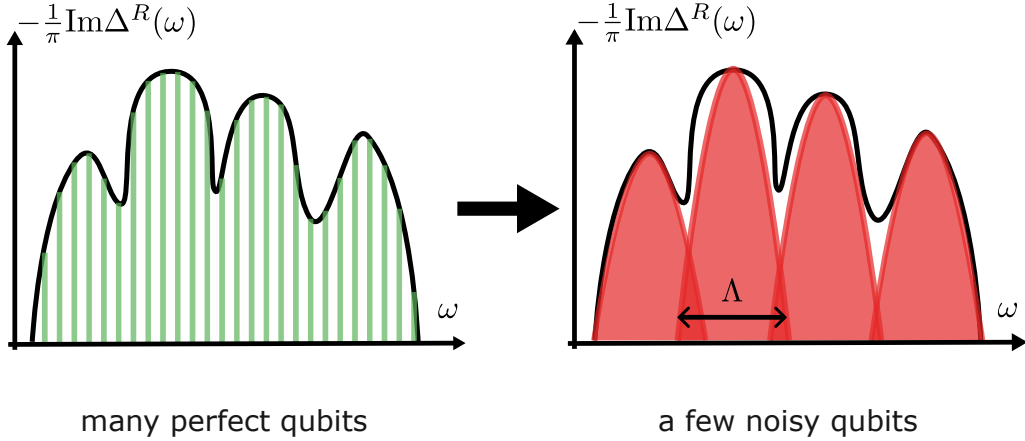


Figure 6.1: Fit of the spectral function $A(\omega) = -\frac{1}{\pi}\text{Im}\Delta^R(\omega)$ within a non-dissipative (left) or a dissipative (right) scheme for the impurity model’s bath. We propose to leverage the widening brought about by qubit dissipation.

problem and a maximal size for the bath is imposed by the number of qubits of the chip. It was proposed to extend the scope of ED approaches by considering dissipative bath sites instead [102, 103, 104]. In these works, a linear coupling of the bath to a reservoir is introduced and shown to provide widened peaks for the fit of the hybridization. This widening holds the promise of reduced requirements over the bath site count, as illustrated on Figure 6.1. In terms of computation, one trades the computation of a state vector with $4^{N_c+N_b}$ components, where N_c is the number of spin-degenerate impurities and N_b the number of spin-degenerate bath sites to that of a reduced density matrix with $4^{N_c+\tilde{N}_b} \times 4^{N_c+\tilde{N}_b}$ elements, with hopefully $\tilde{N}_b \ll N_b$. The solving of master equations implied here in order to compute the reduced dynamics constitutes the (still exponential) computational bottleneck of this method. We thus propose to render this scheme hybrid, combining classical computation with quantum computation to lift this exponential bottleneck. In our proposal, the impurity Green’s function is calculated with a quantum computer, where qubit interaction with the environment of the device naturally provides us with a dissipative bath framework. On the other hand, the impurity qubits, which should model non-dissipative sites, could be the point of focus of error-correction schemes. This is within the scope of a recently-proposed partial error correction paradigm known as clean-dirty [105]. Our proposed hybrid framework could allow for exponential speedups without the stringent requirements over qubit fidelity which hybrid quantum-classical algorithms usually come with. This work lays the ground for the scheme and investigates it from a proof-of-principle perspective.

6.2 Keldysh formalism for out-of-equilibrium many-body systems

Keldysh formalism is a tool which was developed in the 1960s by Keldysh along with Kadanoff, Baym and Schwinger, among others [106, 107], to tackle out-of-equilibrium strongly-correlated systems. As we shall see, the difference with the

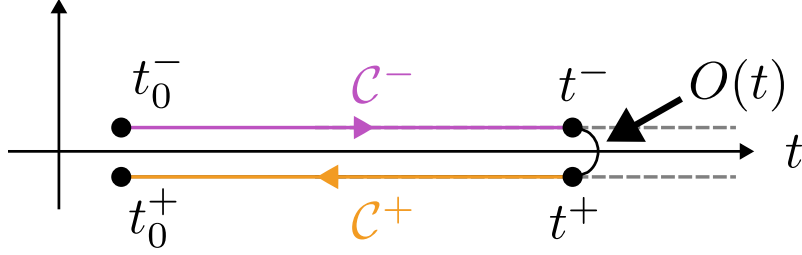


Figure 6.2: Keldysh contour. The superscript indices + and - are branch indices, indicating which branch, the forward-propagating branch \mathcal{C}^- or the backward-propagating branch \mathcal{C}^+ one must consider the time belongs to. The dashed lines materialize the fact that the contour may be extended to infinity so that it does not depend on t .

equilibrium situation is that out-of-equilibrium the occupation of states must be accounted for additionally to that of the accessible states which are described by the spectral function.

6.2.1 Keldysh contour

Keldysh formalism relies on the notion of *Keldysh contour* for integration, from which contour indices will be defined, and correspondingly, different Green's functions according to these indices. To understand how this contour is introduced, let's consider a time-dependent Hamiltonian $\mathcal{H}(t)$, and an observable $\mathcal{O}(t) = \text{Tr}(\rho(t)\mathcal{O})$, where ρ is the density matrix of the system. Suppose the system is initially in the state ρ_0 at some reference time $t_0 < t$. Then, the Heisenberg representation is expressed as $\rho(t) = U(t, t_0)\rho_0 U(t_0, t)$ with:

$$U(t, t_0) = \mathcal{T} \exp \left(-i \int_{t_0}^t \mathcal{H}(u) du \right) \quad (6.1)$$

where \mathcal{T} denotes the time-ordering operator. Note that:

$$U(t_0, t) = \bar{\mathcal{T}} \exp \left(-i \int_t^{t_0} \mathcal{H}(u) du \right) \left(= \bar{\mathcal{T}} \exp \left(i \int_{t_0}^t \mathcal{H}(u) du \right) \right) \quad (6.2)$$

where $\bar{\mathcal{T}}$ anti time-orders the operators it acts on.

Thus, using the cyclicity of the trace the expectation value of the observable at time t reads:

$$\begin{aligned} \mathcal{O}(t) &\equiv \text{Tr}(\rho_0 U(t_0, t) \mathcal{O} U(t, t_0)) \\ &= \langle U(t_0, t) \mathcal{O} U(t, t_0) \rangle \end{aligned}$$

where we have used the shorthand notation $\langle \bullet \rangle \equiv \text{Tr}(\rho_0 \bullet)$ in the second line. Introducing the Keldysh contour $\mathcal{C} = \mathcal{C}^- \cup \mathcal{C}^+$ represented on Figure 6.2, following

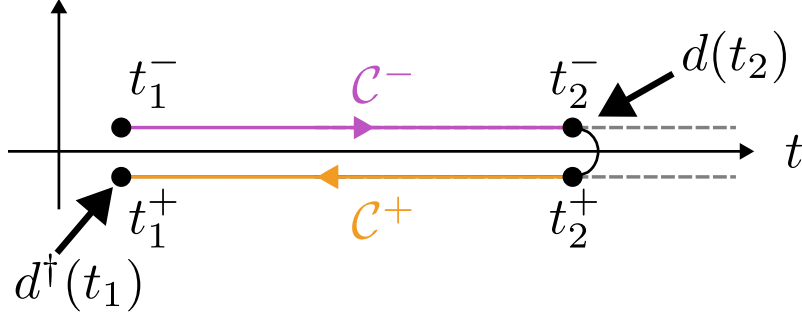


Figure 6.3: Visualization over the Keldysh contour of the calculation of $G_{-+}(t_2, t_1)$ for $t_2 > t_1$.

the convention of [108] for the labelling of the two branches¹, one can rewrite this quantity as (see Appendix M):

$$\mathcal{O}(t) = \left\langle \mathcal{T}_c \left(\exp \left(-i \int_c \mathcal{H}(s) ds \right) O(t) \right) \right\rangle \quad (6.3)$$

In this expression, \mathcal{T}_c is the contour-ordering operator which orders the expression it acts upon according to their position on the contour: earlier operators in terms of contour ordering are placed on the right. $O(t)$ stands for the operator O in Schrödinger representation, for which we retained the time label in order to lift any ambiguity with regards to the position of O in the expression ordered along the contour. More specifically, $O(t)$ stands, in terms of contour variables, for either $O(t^-)$ or $O(t^+)$. Finally, the notation s stands for times along the contour, which formally is rendered by two variables:

$$s = (t \in \mathbb{R}, \alpha \in \{-, +\}) \quad (6.4)$$

or alternatively, as we will do further on, setting the branch index as an upperscript:

$$s = t^\alpha, \quad t \in \mathbb{R}, \quad \alpha \in \{-, +\} \quad (6.5)$$

6.2.2 Contour-ordered Green's functions

Definitions In equilibrium systems, time-translation invariance ensures that the single particle Green's functions depend on a single time. Out of equilibrium, this is not true in general. In analogy with the time-ordered Green's function introduced in chapter 3 and that we recall here:

$$G_{ij}(t, t') = -i \left\langle \mathcal{T} d_i(t) d_j^\dagger(t') \right\rangle, \quad (6.6)$$

we introduce the contour-ordered local Green's function which depends on two times (s_1, s_2) on the contour as

$$G_{ij}(s_2, s_1) = -i \left\langle \mathcal{T}_c d_i(s_2) d_j^\dagger(s_1) \right\rangle \quad (6.7)$$

¹The opposite convention is often used.

We will cast G as a block matrix according to the branches indices α_1, α_2 carried by s_1 and s_2 . More specifically, we will note $\underline{G}(t_2, t_1)$ the following matrix whose entries depend on real variables t_1 and t_2 :

$$\begin{aligned}\underline{G}(t_2, t_1) &= \begin{pmatrix} G(t_2^-, t_1^-) & G(t_2^-, t_1^+) \\ G(t_2^+, t_1^-) & G(t_2^+, t_1^+) \end{pmatrix} \\ &= \begin{pmatrix} G_{--}(t_2, t_1) & G_{-+}(t_2, t_1) \\ G_{+-}(t_2, t_1) & G_{++}(t_2, t_1) \end{pmatrix}\end{aligned}\quad (6.8)$$

Let us suppose $t_2 > t_1$, $d_i = d_j \equiv d$ and expand $G_{-+}(t_2, t_1)$. Since $t_2^- <_c t_1^+$ (see Figure 6.3), we have:

$$\begin{aligned}G_{-+}(t_2, t_1) &= -i \langle \mathcal{T}_c d(t_2^-) d^\dagger(t_1^+) \rangle \\ &= i \langle d^\dagger(t_1^+) d(t_2^-) \rangle \\ &= i \langle d^\dagger(t_1) d(t_2) \rangle \\ &\equiv G^<(t_2, t_1)\end{aligned}$$

This latter quantity is called the *lesser* Green's function. If $t_2 < t_1$, we retrieve this Green's function as now the contour-ordering operator does not invert $d(t_2^-)$ and $d^\dagger(t_1^+)$, but we can still invert them applying the anticommutation rules. Recognizing other Green's functions which are listed in the formulary of Appendix C, all in all, whichever t_1 and t_2 :

$$\underline{G}(t_2, t_1) = \begin{pmatrix} G^{\mathcal{T}}(t_2, t_1) & G^<(t_2, t_1) \\ G^>(t_2, t_1) & G^{\bar{\mathcal{T}}}(t_2, t_1) \end{pmatrix}\quad (6.9)$$

There are actually only two independent elements in the matrix above, because:

$$\begin{aligned}G^{\mathcal{T}}(t_2, t_1) &= \Theta(t_2 - t_1) G^>(t_2, t_1) + \Theta(t_1 - t_2) G^<(t_2, t_1) \\ G^{\bar{\mathcal{T}}}(t_2, t_1) &= \Theta(t_1 - t_2) G^>(t_2, t_1) + \Theta(t_2 - t_1) G^<(t_2, t_1).\end{aligned}$$

Moreover, we will find convenient to write it in another basis, in which \underline{G} only displays three blocks. As listed in the appendix, we can indeed define the retarded Green's function G^R from $G^<$ and $G^>$ as:

$$G^R(t_2, t_1) = \Theta(t_2 - t_1) (G^>(t_2, t_1) - G^<(t_2, t_1))\quad (6.10)$$

as well as the *Keldysh* Green's function

$$G^K(t_2, t_1) = G^>(t_2, t_1) + G^<(t_2, t_1)\quad (6.11)$$

and the *advanced* Green's function

$$G^A(t_2, t_1) = G^R(t_2, t_1) - G^>(t_2, t_1) - G^<(t_2, t_1)\quad (6.12)$$

such that upon the basis change defined by the block matrix

$$P = \frac{1}{\sqrt{2}} \begin{pmatrix} 1 & 1 \\ 1 & -1 \end{pmatrix} \quad (6.13)$$

we have the similarity relation

$$\underline{G}(t_2, t_1) \sim \begin{pmatrix} G^K(t_2, t_1) & G^R(t_2, t_1) \\ G^A(t_2, t_1) & 0 \end{pmatrix} \quad (6.14)$$

To have an upper triangular form, we will prefer using a slightly modified transformation. We define \tilde{G} as

$$\tilde{G} \equiv P^{-1} \sigma_Z \underline{G}(t_2, t_1) P = \begin{pmatrix} G^R(t_2, t_1) & G^K(t_2, t_1) \\ 0 & G^A(t_2, t_1) \end{pmatrix} \quad (6.15)$$

where σ_Z is the block-matrix version of the Pauli- z matrix $\sigma_z = \begin{pmatrix} 1 & 0 \\ 0 & -1 \end{pmatrix}$. Finally, since the greater and lesser hybridizations obey the following symmetry upon time-reversal:

$$G^>(t_2, t_1)^\dagger = -G^>(t_1, t_2) \quad (6.16)$$

$$G^<(t_2, t_1)^\dagger = -G^<(t_1, t_2) \quad (6.17)$$

we may always assume a specific ordering of the real variables t_1 and t_2 and get all the necessary information.

Case of a steady-state We will consider the Green's functions introduced above are taken over a steady-state ρ_{NESS} . By definition, in a steady state time-translation invariance holds. We can thus define the usual Fourier transform for the (now single-time) Green's functions defined in the paragraph above, with the convention given in Appendix B. We will note

$$G^R(\omega) \equiv \lim_{\eta \rightarrow 0^+} G^R(\omega + i\eta) \quad (6.18)$$

$$G^A(\omega) \equiv \lim_{\eta \rightarrow 0^-} G^A(\omega + i\eta) = G^R(\omega)^\dagger \quad (6.19)$$

$$A(\omega) \equiv -\frac{1}{\pi} \text{Im} G^R(\omega) \quad (6.20)$$

and make use of the following relations:

$$G^K(\omega) = G^<(\omega) + G^>(\omega) \quad (6.21)$$

$$G^K(\omega)^\dagger = -G^K(\omega) \quad (6.22)$$

$$\text{Re} G^R(\omega) = \frac{1}{\pi} \text{P.V.} \int_{\mathbb{R}} d\omega' \frac{\text{Im} G^R(\omega')}{\omega' - \omega} \quad (6.23)$$



$$\Delta_{\text{aux}}^R(\omega) = (G_{V=0}^R)^{-1} - G^{-1} \quad \Delta_{\text{aux}}^R(\omega) = \left((G_{V=0, \Lambda=0}^R)^{-1} - \Sigma^R(\omega) \right) - G^{-1}$$

Figure 6.4: Illustration of the nesting property of hybridizations. On the left, the impurity is hybridized with coupling matrix V with a free fermion bath. On the right, it is coupled to a dissipative bath, whose dissipation is tuned by a reservoir-coupling parameter Λ . The resulting hybridization characterizing the effect of the dissipative bath onto the impurity picks an additional self-energy term. We resort to a Lindbladian linear dissipation to a reservoir in order to get a self-energy which provides an widening of the peaks for the fit of the DMFT hybridization.

The last relation is called the Kramers-Kronig relation, it holds for any causal Green's function as demonstrated in Appendix D.

In the usual Anderson impurity model DMFT maps the Hubbard model onto, we recall that the hybridization to the free-fermion bath at energies ϵ_p with couplings V_p reads

$$\Delta(i\omega_n) = \sum_p \frac{|V_p|^2}{i\omega_n - \epsilon_p}. \quad (6.24)$$

This expression is associated with a bath density of states which is made of delta peaks: the Plemelj-Sokhatski formula states that

$$\lim_{\eta \rightarrow 0^+} \frac{1}{\omega + i\eta} = \text{P.V} \left(\frac{1}{\omega} \right) - i\pi\delta(\omega) \quad (6.25)$$

with P.V the Cauchy principal value, so that after analytic continuation in 6.24

$$-\frac{1}{\pi} \text{Im}\Delta^R(\omega) = \sum_p |V_p|^2 \delta(\omega - \epsilon_p). \quad (6.26)$$

This strongly impacts Exact Diagonalization, which thus suffers from poor capabilities in terms of fit of the Weiss field. We thus turn to a dissipative bath scheme, which that we are ready to describe now that the Keldysh formalism was introduced.

6.3 Dissipative bath scheme

The goal of this section is to describe the dynamics brought about by dissipation in the bath, described within a Lindblad equation. This scheme was proposed in a classical computation context in [102, 103, 104] to describe the non-equilibrium steady state transport in a quantum dot. We follow closely and expand the argumentation

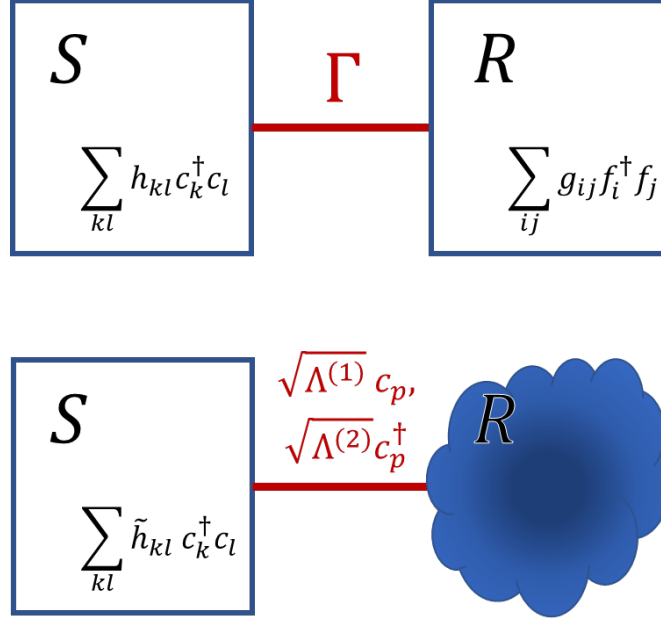


Figure 6.5: Two types of quadratic 'bath' systems. Upper panel: system connected to a non-dissipative reservoir. Lower panel: system connected to a dissipative reservoir. The reduced dynamics is rendered by Lindblad's equation with jump operators $\sqrt{\Lambda^{(1)}} c_p, \sqrt{\Lambda^{(2)}} c_p^\dagger$. The unitary part of the reduced dynamics is given by \tilde{h} , which includes Lamb shifts terms additionally to h .

of Reference [104]. We will denote by *system* the bath, whereas its traced out environment will be dubbed *reservoir*. First, we consider the tracing out of reservoir degrees of freedom where the system and the reservoir form a closed system, with known, quadratic unitary dynamics. This aims at illustrating the nesting property of the retarded hybridization characterizing the effect of a quadratic system onto a system it linearly couples with, as pictured on Figure 6.4, as well as the form of the Keldysh hybridization. These forms will be retained when the dissipation of the bath is of Lindblad type, within a linear coupling with reservoir degrees of freedom. Then, we turn to the proper Lindbladian dissipative scheme to sort out the form of the self-energy terms arising due to dissipation. The two models are depicted on Figure 6.5.

6.3.1 Steady-state Green's functions in the absence of dissipation

We consider first a closed system comprising a system of interest S which hybridizes with a reservoir R which was plugged at time 0, as pictured on Figure 6.5, upper panel. We consider the non-equilibrium steady state of the joint system. We suppose that the whole system is described by a quadratic Hamiltonian

$$H = \sum_{kl} h_{kl} c_k^\dagger c_l + \sum_{ij} g_{ij} f_i^\dagger f_j + \sum_{ik} \Gamma_{ik} (f_i^\dagger c_k + \text{h.c.}) \quad (6.27)$$

where c denotes the n_b system modes and f denotes reservoir modes. Let us order the modes so that the system modes come first, and then the reservoir modes. Then, the inverse of the Matsubara Green's function can be written in block form

$$G^{-1}(i\omega_n) \equiv i\omega_n - H_1 = \begin{pmatrix} i\omega_n - h & \Gamma^\dagger \\ \Gamma & i\omega_n - g \end{pmatrix} \quad (6.28)$$

(H_1 is the single-particle Hamiltonian).

The upperleft block of $G(i\omega_n)$, denoted $G_{[:n_b, :n_b]}(i\omega_n)$ in a pythonic notation, concerns the system of interest. With block matrix inversion, similar to that carried out to get the expression for the local Green's function of the resonant level model in Appendix E, it reads:

$$G_{[:n_b, :n_b]}(i\omega_n) = (i\omega_n - h - \Gamma^\dagger (i\omega_n - g)^{-1} \Gamma)^{-1} \quad (6.29)$$

Upon analytic continuation $i\omega_n \rightarrow \omega + i0^+$ we find that the retarded Green's function matrix for the system reads

$$G^R(\omega) = (\omega - h - \Sigma^R(\omega))^{-1} \quad (6.30)$$

where

$$\Sigma^R(\omega) \equiv \Gamma^\dagger (\omega + i0^+ - g)^{-1} \Gamma \quad (6.31)$$

encodes all the information about the effect of the 'traced-out' reservoir on the spectrum of the system.

The calculation for the Keldysh Green's function is more involved. We start from the big matrix of Keldysh components for subsystem S , $\underline{\tilde{G}} = \begin{pmatrix} G^R & G^K \\ 0 & G^A \end{pmatrix}$ introduced in 6.15. We define similarly to $\underline{\tilde{G}}$ the hybridization matrix in Keldysh notation $\underline{\tilde{\Sigma}} \equiv \begin{pmatrix} \Sigma^R & \Sigma^K \\ 0 & \Sigma^A \end{pmatrix}$.

It verifies Dyson's equation:

$$\underline{\tilde{\Sigma}} = \underline{\tilde{G}}_0^{-1} - \underline{\tilde{G}}^{-1} \quad (6.32)$$

where the lowercase $_0$ indicates Green's functions for the system of interest disconnected from the reservoir ($\Gamma = 0$ in 6.27). Carrying out once again block-matrix inversion we have

$$\begin{aligned} \underline{\tilde{G}}_0^{-1} &= \begin{pmatrix} G_0^R & G_0^K \\ 0 & G_0^A \end{pmatrix}^{-1} \\ &= \begin{pmatrix} (G_0^R)^{-1} & - (G_0^R)^{-1} G_0^K (G_0^A)^{-1} \\ 0 & (G_0^A)^{-1} \end{pmatrix} \end{aligned}$$

and similarly

$$\underline{\tilde{G}}^{-1} = \begin{pmatrix} (G^R)^{-1} & - (G^R)^{-1} G^K (G^A)^{-1} \\ 0 & (G^A)^{-1} \end{pmatrix}$$

We retrieve Equation 6.31 since $G_0^R(\omega) = \frac{1}{\omega + i0^+ - h}$ (free-fermion system). We also have a Dyson equation for the advanced component, $\Sigma^A = (G^A)^{-1} - (G_0^A)^{-1}$. On the other hand, for the Keldysh component, we have:

$$G^K = G^R \Sigma^K G^A + G^R (G_0^R)^{-1} G_0^K (G_0^A)^{-1} G^A \quad (6.33)$$

However, the second term can be neglected. We do not give any formal proof of this result, but we might give an intuition of why it is so: G_0^K contains information both about the spectrum and the occupation of the initial state, that of the disconnected system. We assume we connect to a reservoir which is way bigger than the system, and drives the system to a steady state which is unique. Thus, we can consider the second term disappears because otherwise the steady-state would exhibit a dependence on the initial state.

All in all, since in the steady state $G^A(\omega) = G^R(\omega)^\dagger$ we have

$$G^K(\omega) = G^R(\omega) \Sigma^K(\omega) G^R(\omega)^\dagger. \quad (6.34)$$

Now, what happens if we plug in dissipation onto the bath levels? More specifically, we will want to connect linearly – in a sense that will be made cleared later – each bath level to a Markovian reservoir. This corresponds to the situation sketched on the lower panel of Figure 6.5, and to the bath we aim at connecting the impurity to in a DMFT scheme, as depicted more specifically in Figure 6.6. This specific choice of Lindblad dissipative processes mirrors the modelling of qubit damping (see 4.5.1), except that in that latter case, within Jordan-Wigner encoding, as we shall see Z chains appear in the definition of the Lindblad jump operators which translate into a modified dynamics. This dynamics however retain the qualitative features associated to the 'fermionic' dissipation of the considered model.

Within Lindblad coupling to the reservoirs, a relation such as 6.31 does not hold anymore because the precise form of the reservoir dynamics is unknown. Instead, the hybridization to the reservoir degrees of freedom will bring about widened peaks in the hybridization between the impurity and the bath, as the Σ^R and Σ^K of Equations 6.30 and 6.34 will specify to

$$\Sigma^R(\omega) \rightarrow \Delta^{\text{Lamb}} - i\Lambda^{(+)} \quad (6.35)$$

$$\Sigma^K(\omega) \rightarrow -2i\Lambda^{(-)} \quad (6.36)$$

where $\Lambda^{(+)}$ and $\Lambda^{(-)}$ are related to the strengths of the Lindblad couplings and Δ^{Lamb} is a static self-energy shift. The remainder of this section is dedicated to deriving these relations.

For the sake of simplicity, we keep on considering a single spin species in what follows. We assume the bath sites are subject to damping at rates $\Lambda^{(1)}$ resp. $\Lambda^{(2)}$.

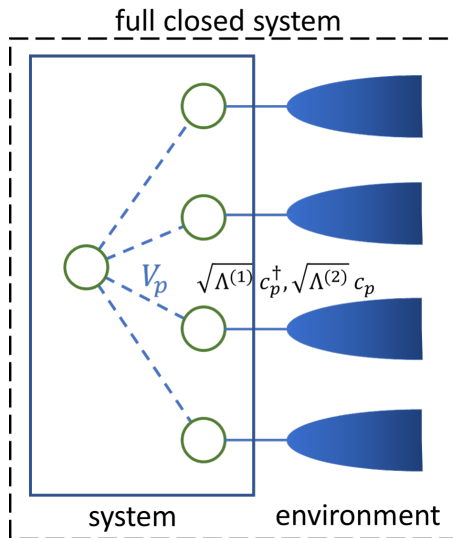


Figure 6.6: Structure of the considered system, comprising an impurity site connected to dissipative bath sites. Each bath site is connected linearly to a Markovian reservoir.

The jump operators are taken to be the $\sqrt{\Lambda^{(1)}}c_p$ and $\sqrt{\Lambda^{(2)}}c_p^\dagger$. Since they only display a single fermionic operator, we refer to this dissipative process as a *linear* coupling of the bath sites to the reservoirs. This system plus the reservoirs the bath sites are connected to form a closed system, and we are interested in the dynamics of the reduced system. The model is represented on Figure 6.6. We suppose that the dynamics with respect to the reservoirs is Markovian. Then we have a Lindblad equation driving the evolution of $\rho_S \equiv \text{Tr}_R(\rho_{SR})$ which will most of the time be denoted as ρ further on to lighten the notation. The precise form of the Lindblad equation is², for $t > 0$:

$$\dot{\rho} = -i[\tilde{H}, \rho] + \sum_p \Lambda^{(1)} (2c_p \rho c_p^\dagger - \{c_p^\dagger c_p, \rho\}) + \sum_p \Lambda^{(2)} (2c_p^\dagger \rho c_p - \{c_p c_p^\dagger, \rho\}). \quad (6.37)$$

Here, \tilde{H} denotes the unitary part of the evolution. ρ must be understood as $\rho(t)$.

How, within this Lindbladian evolution, do nonequilibrium Green's functions evolve? We will see that deriving the equations of motion of Green's functions out of equilibrium is not straightforward, and relies on so-called *Quantum Regression Theorems*. The reason behind this is that Lindblad's equation only tells us about the dynamics of the reduced system, but forgets about details about the environment, so that we cannot simply trace out environmental degrees of freedom within a unitary evolution.

²Note that the convention chosen here for the jump operators is not universal, and in particular is different from the one chosen in 4.5.2 to introduce the Lindblad master equation. The two conventions are related by a global rescaling of the jump operators.

6.3.2 Fermionic quantum regression theorem

We want to compute two-point correlators of the form

$$\langle A(t)B \rangle \equiv \text{Tr}(\rho A(t)B) \quad (6.38)$$

where ρ is the density matrix of the system S in the NESS (non-equilibrium steady state), A and B are fermionic operators of degree one (ie, A and B are each a single fermionic annihilation or creation operator) acting on the system S 's subspace, and the trace is taken over system S 's degrees of freedom.

For a closed system $S + R$ described by a Hamiltonian \hat{H} , extending the operators A and B to operators over the full system $S + R$ as \hat{A} and \hat{B} , we have:

$$\langle \hat{A}(t)\hat{B} \rangle \equiv \text{Tr}_{SR} \left(e^{i\hat{H}t} \hat{A} e^{-i\hat{H}t} \hat{B} \rho_{SR}(0) \right) \quad (6.39)$$

$$= \text{Tr}_S \left(\text{Tr}_R \left(e^{i\hat{H}t} \hat{A} e^{-i\hat{H}t} \hat{B} \rho_{SR}(0) \right) \right) \quad (6.40)$$

$$= \langle A(t)B \rangle \quad (6.41)$$

(for consistency) and associatedly

$$\partial_t \langle \hat{A}(t)\hat{B} \rangle = -i \text{Tr}_{SR} \left([\hat{A}, \hat{H}] \hat{B} \rho_{SR}(t) \right) \quad (6.42)$$

but this cannot be put to use in our situation, for the two following reasons:

- we do not know \hat{H} , instead we only know of the evolution of $\rho_S(t)$
- for a fermionic operator A , because of anticommutation the extension of A to an operator \hat{A} over the full joint system is not trivial, as opposed to the bosonic case where we would have $\hat{A} = A \otimes I_R$

For bosonic operators, the so-called *Quantum Regression Theorem* (QRT, [109]) – whose hypotheses are that supporting the Lindblad equation – states that if $\rho_S(t)$ evolves with Lindbladian \mathcal{L} ,

$$\dot{\rho}_S(t) = \mathcal{L}[\rho_S(t)] \quad (6.43)$$

of formal solution³

$$\rho_S(t) = G_{\mathcal{L}}^t[\rho_S(0)] \quad (6.44)$$

then we have:

$$\langle \hat{A}(t)\hat{B} \rangle \equiv \text{Tr}_{SR} \left(\hat{A} G_{-i[\hat{H}, \bullet]}^t[\hat{B} \rho_{SR}(0)] \right) = \langle A(t)B \rangle \equiv \text{Tr}_S \left(A G_{\mathcal{L}}^t[B \rho_S(0)] \right) \quad (6.45)$$

and similarly

$$\langle \hat{B}\hat{A}(t) \rangle = \text{Tr}_S \left(A G_{\mathcal{L}}^t[\rho_S(0)B] \right) \quad (6.46)$$

³We define $G_{\mathcal{L}}^t = e^{i\mathcal{L}t}$.

The fermionic case is however different. A fermionic version of the QRT is derived in [104]. Let C be a fermionic operator of degree one. We define the following operators acting in S :

$$\rho_C(t) \equiv \text{Tr}_R(\hat{\rho}_C(t)) \quad (6.47)$$

$$\rho'_C(t) \equiv \text{Tr}_R(\hat{\rho}'_C(t)) \quad (6.48)$$

where operators $\hat{\rho}_C(t)$ and $\hat{\rho}'_C(t)$ admit an Heisenberg representation similar to that of proper density matrices

$$\hat{\rho}_C(0) = C\hat{\rho} \quad (6.49)$$

$$\hat{\rho}_C(t) = e^{-i\hat{H}t} (C\hat{\rho}) e^{i\hat{H}t} \quad (6.50)$$

$$\hat{\rho}'_C(0) = \hat{\rho}C \quad (6.51)$$

$$\hat{\rho}'_C(t) = e^{-i\hat{H}t} (\hat{\rho}C) e^{i\hat{H}t} \quad (6.52)$$

We denote by \mathcal{L} the superoperator⁴ defining the right-hand side of Lindblad equation 6.37, which governs the evolution of the system's density matrix $\rho(t)$. We denote by $\bar{\mathcal{L}}$ the following superoperator

$$\bar{\mathcal{L}}[\rho] = -i[\tilde{H}, \rho] + \sum_p \Lambda^{(1)} (-2c_p \rho c_p^\dagger - \{c_p^\dagger c_p, \rho\}) + \sum_p \Lambda^{(2)} (-2c_p^\dagger \rho c_p - \{c_p c_p^\dagger, \rho\}). \quad (6.53)$$

Then, the fermionic version of the QRT reads

$$\langle A(t)C \rangle = \text{Tr}_S (AG_{\bar{\mathcal{L}}}^t[\rho_C(0)]) \quad (6.54)$$

$$\langle CA(t) \rangle = \text{Tr}_S (AG_{\mathcal{L}}^t[\rho'_C(0)]) \quad (6.55)$$

so that in the steady-state $\rho = \rho_{\text{NESS}}$,

$$\langle A(t)C \rangle = \text{Tr}_S (AG_{\bar{\mathcal{L}}}^t[C\rho_{\text{NESS}}]) \quad (6.56)$$

$$\langle CA(t) \rangle = \text{Tr}_S (AG_{\mathcal{L}}^t[\rho_{\text{NESS}}C]) \quad (6.57)$$

6.3.3 Out-of-equilibrium Green's functions in the presence of linear dissipation

Equipped with the fermionic QRT stated in 6.56, one can derive the steady-state equations of motion for $G^R(t)$ and $G^K(t)$. The calculation for $G^R(t)$ does not exhibit any technical or conceptual difficulty but is rather tedious. Fourier transforming the

⁴A superoperator is an operator over operators.

equations of motion, one finds the following relations which are the support for the dissipative bath approach:

$$G^R(\omega) = \frac{1}{\omega - \tilde{h} + i\Lambda^{(+)}} \quad (6.58)$$

$$G^K(\omega) = iG^R(\omega)2\Lambda^{(-)}G^R(\omega)^\dagger \quad (6.59)$$

where we have defined $\Lambda^{(+/-)} \equiv \Lambda^{(1)} \pm \Lambda^{(2)}$ and \tilde{h} is the matrix defining the terms of the quadratic Hamiltonian of the system, $H = \sum \tilde{h}_{kl}c_m^\dagger c_n = \sum (h_{kl} + \Delta_{kl}^{\text{Lamb}})c_m^\dagger c_n$. Alternatively, Equations 6.58 can be derived within the *superfermion* formalism, which consists in vectorizing the density matrix in an widened space [102].

The consequence of these dissipative processes on the hybridization function of such bath levels connected to a non-interacting impurity site is a lorentzian widening of peaks, as is expanded in the next section.

6.4 Auxiliary hybridization associated with the dissipative scheme

We are aiming at fitting some given $\Delta^<$ and $\Delta^>$. We consider a 'star' geometry, meaning that the bath levels are not connected between themselves. As we shall see the two fits may be done separately, with the help of two sets of bath levels, corresponding to either empty or full levels. The impurity and its connection with the dissipative bath levels are depicted on Figure 6.7. The two sets will be characterized by different Lindblad operators, but with the same Lindblad rates. We make the hypothesis that the qubits are only affected by amplitude damping (relaxation), which means that the effective temperature of their environment is supposed to be low enough that it does not incur excitation effects. Then, by changing the encoding, we will be able to represent excitation through the amplitude damping channel of the qubits.

We aim to derive the specific form of the auxiliary hybridizations we will get provided with to fit the physical hybridization within a DMFT loop:

$$i\Delta_{\text{aux}}^>(\omega) = -\sum_{g=1}^{n_b/2} |V_g|^2 (-ig_g^>(\omega)) = \sum_{g=1}^{n_b/2} \frac{2\Lambda|V_g|^2}{(\omega - \epsilon_g)^2 + \Lambda^2} \quad (6.60)$$

$$-i\Delta_{\text{aux}}^<(\omega) = \sum_{l=1}^{n_b/2} |V_l|^2 (-ig_l^>(\omega)) = \sum_{l=1}^{n_b/2} \frac{2\Lambda|V_l|^2}{(\omega - \epsilon_l)^2 + \Lambda^2} \quad (6.61)$$

We start from the expressions for the Green's function elements in Keldysh formalism for a single dissipative bath site lying at energy ϵ_p (Equations 6.58, but involving scalars)

$$g^R(\omega) = \frac{1}{\omega - \epsilon_p + i\Lambda^{(+)}} \quad (6.62)$$

$$g^K(\omega) = 2ig^R(\omega)\Lambda^{(-)}g^R(\omega)^\dagger \quad (6.63)$$

Then since $g^>(\omega) = \frac{1}{2}(g^K(\omega) + 2i\text{Im}g^R(\omega))$ (see Appendix C) we have that $g^>(\omega)$ is purely imaginary and that

$$\begin{aligned} -ig^>(\omega) &= i\text{Im}g^>(\omega) = i\frac{1}{2}(\text{Im}g^K(\omega) + 2\text{Im}g^R(\omega)) \\ &= \frac{1}{2}(2|g^R(\omega)|^2\Lambda^{(-)} + 2\text{Im}g^R(\omega)) \\ &= \frac{1}{|\omega - \epsilon_q + i\Lambda^{(+)}|^2}(\Lambda^{(-)} - \text{Im}(\omega - \epsilon_q + i\Lambda^{(+)})) \\ &= \frac{1}{(\omega - \epsilon_p)^2 + \Lambda^{(+)^2}}(\Lambda^{(-)} - \Lambda^{(+)}) \end{aligned} \quad (6.64)$$

using that for $z = \frac{1}{z'}$ we have $\text{Im}z = -\text{Im}z'/|z'|^2$ and $|z| = 1/|z'|$.

Similarly, since $g^<(\omega) = \frac{1}{2}(g^K(\omega) - 2i\text{Im}g^R(\omega))$ we have

$$-ig^<(\omega) = i\text{Im}g^<(\omega) = \frac{1}{(\omega - \epsilon_p)^2 + \Lambda^{(+)^2}}(\Lambda^{(-)} + \Lambda^{(+)}) \quad (6.65)$$

Replacing $\Lambda^{(+)}$ and $\Lambda^{(-)}$ by their expressions, we get

$$-ig^>(\omega) = -\frac{2\Lambda^{(2)}}{(\omega - \epsilon_p)^2 + (\Lambda^{(1)} + \Lambda^{(2)})^2} \quad (6.66)$$

$$-ig^<(\omega) = \frac{2\Lambda^{(1)}}{(\omega - \epsilon_p)^2 + (\Lambda^{(1)} + \Lambda^{(2)})^2} \quad (6.67)$$

Let's consider half of the bath sites (indexed by g) are subject to dissipation with the $\Lambda^{(2)}$ channel (excitation), and the other half (indexed by l), with the $\Lambda^{(1)}$ channel (amplitude damping), as pictured on Figure 6.7. Let Λ be the decay rate for each. Then we have

$$-ig_g^>(\omega) = -\frac{2\Lambda}{(\omega - \epsilon_g)^2 + \Lambda^2} \quad (6.68)$$

$$-ig_g^<(\omega) = 0 \quad (6.69)$$

whereas

$$ig_l^>(\omega) = 0 \quad (6.70)$$

$$-ig_l^<(\omega) = \frac{2\Lambda}{(\omega - \epsilon_l)^2 + \Lambda^2} \quad (6.71)$$

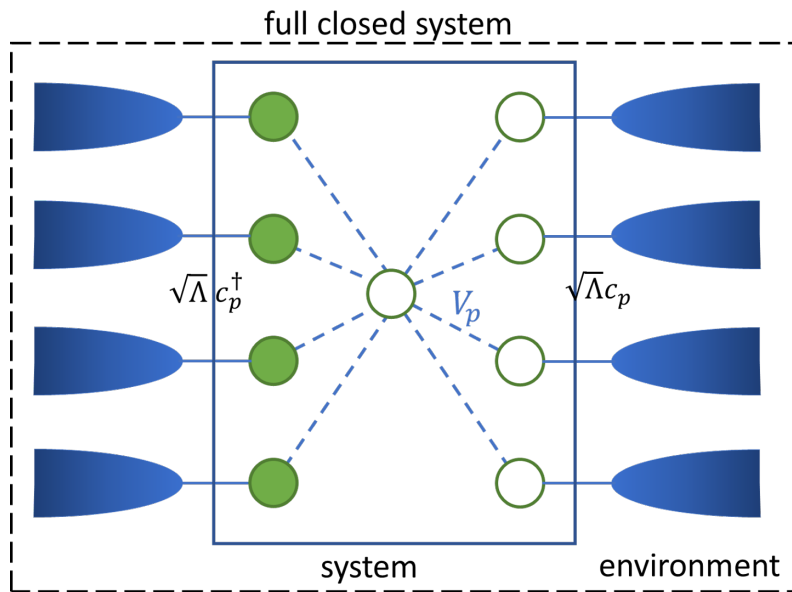


Figure 6.7: Chosen geometry of the bath. The bath sites come in two sets, each displaying a single of the two dissipative processes. Half of the sites are used to fit the lesser part $<$, and half are used to fit the greater part $>$ of the DMFT hybridization. The damped bath sites (on the right) are initialized to being all empty, which corresponds to their steady-state in the absence of coupling to the impurity. For the same reason, the excited bath sites (on the left) are initialized to being all occupied.

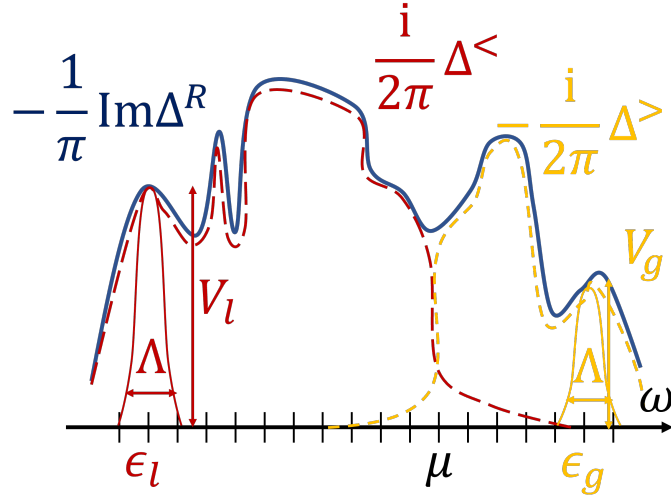


Figure 6.8: Cartoon representation of the fit of the DMFT hybridization. The DMFT bath spectral function decomposes as $-\frac{1}{\pi}\text{Im}\Delta^R(\omega) = \frac{i}{2\pi}\Delta^<(\omega) - \frac{i}{2\pi}\Delta^>(\omega)$. The lesser part and the greater part are fitted separately, with different sets of dissipative bath sites. On this picture, it is implied that the DMFT hybridization is that of an equilibrium system, so that the fluctuation-dissipation theorem holds.

which are Lorentzian centered around the energy of the site and with width Λ .

Let us now consider a non-interacting impurity is connected to the dissipative bath system, with real couplings V_p . With a derivation similar to 6.31, we can readily show that the auxiliary hybridization to the dissipative system reads

$$i\Delta_{\text{aux}}^>(\omega) = -\sum_{g=1}^{n_b/2} |V_g|^2 (-ig_g^>(\omega)) = \sum_{g=1}^{n_b/2} \frac{2\Lambda|V_g|^2}{(\omega - \epsilon_g)^2 + \Lambda^2} \quad (6.72)$$

$$-i\Delta_{\text{aux}}^<(\omega) = \sum_{l=1}^{n_b/2} |V_l|^2 (-ig_l^<(\omega)) = \sum_{l=1}^{n_b/2} \frac{2\Lambda|V_l|^2}{(\omega - \epsilon_l)^2 + \Lambda^2} \quad (6.73)$$

The fitting procedure is illustrated on Figure 6.8.

The knobs for the fits are:

- the energies of the bath levels, ϵ_p
- the couplings V_p

The joint optimization of these two sets of parameters was investigated in [103]. However, as the number of bath sites increases, the optimization quickly becomes difficult and the authors had to turn to a Markov Chain Monte-Carlo method rather than standard optimization methods for as few as six bath sites. To simplify, one can consider a fixed grid of energies ϵ_p and only tune the couplings V_p . The only knobs then become the V_l and V_g .

One needs to minimize $\|\Delta^{</>}(\omega) - \Delta_{\text{aux}}^{</>}(\omega)\|$. This can be done by setting a fine ω grid and looking at both functions of these points. One can define the following cost functions:

$$\chi_g(\{V_g\}) = \sum_i \Delta\omega (\text{Im}\Delta^>(\omega_i) - \text{Im}\Delta_{\text{aux}}^>(\omega_i, \{V_g\}))^2 \quad (6.74)$$

$$\chi_l(\{V_l\}) = \sum_i \Delta\omega (\text{Im}\Delta^<(\omega_i) - \text{Im}\Delta_{\text{aux}}^<(\omega_i, \{V_l\}))^2 \quad (6.75)$$

and minimize them with standard methods to get the optimal couplings V_p and V_l .

6.5 Hybrid quantum-classical algorithm for DMFT with a dissipative bath

DMFT admits a non-equilibrium formulation [110] that readily generalizes the equilibrium version by considering self-consistency at the level of each of the Keldysh components of the Green's functions. We assume that the qubits are subject to the dissipative process described in this section, with noise strength Λ . This is a strong assumption: most importantly we assume that the qualitative dynamics associated to qubit damping is similar to that of the dissipative process studied beforehand, which was shown to provide widened peaks for the hybridization of the impurity model. The validity of this assumption is beyond the scope of this work, although in the next section we give a quick glimpse at the effect of modelling qubit noise with qubit jump operators rather than fermionic jump operators. Note that quantum computers of fermionic nature are now emerging [111], and might be leveraged for this algorithm.

We propose, either for equilibrium systems or out of equilibrium the following hybrid quantum-classical impurity solver:

- Being given $\Delta^<$ and $\Delta^>$, adjust the parameters of the impurity model \mathcal{H}_{AIM} , ϵ_p and V_p , by considering two batches: (V_l, ϵ_l) for the lesser hybridization and (V_g, ϵ_g) for the greater component. For instance, the energies can be fixed by equispacing over the support of each hybridization, and the hoppings can be optimized through standard minimization of the cost functions 6.74.
- Initialize the bath qubits devoted to the fit of $\Delta^<$ (resp. $\Delta^>$) as being in occupied state $|1\rangle$ (resp. empty state $|0\rangle$). This corresponds to the steady state of the bath.
- Implement on the quantum chip the time evolution driven by \mathcal{H}_{AIM} . This might be done through trotterization (see section 4.4.2).
- Allow for a sufficient initialization time so that the system { impurity + bath } reaches the steady-state.

- Once the steady regime is established, measure the interacting impurity's Green's function on the chip. For instance, in the equilibrium case, one can use the method proposed in [112] which relies on an auxiliary qubit to carry out measurements in the frequency domain reminiscent of ARPES experiments.
- Apply the DMFT self-consistency relation 3.20, $\mathcal{G}_0^{-1}(i\omega_n) = G_{\text{loc}}^{-1}(i\omega_n) + \Sigma_{\text{imp}}(i\omega_n)$, to get new lesser and greater hybridizations stemming from $\Delta^R(i\omega_n) = i\omega_n + \mu - \mathcal{G}_0^{-1}(i\omega_n)$ for the fit.
- Stop when the hybridizations get stabilized.

6.6 Quality of the fits with the bath size and the strength of dissipation

We consider we want to fit the lesser and greater components of a hybridization at equilibrium, at inverse temperature $\beta = 1/T$. We assume that the Fermi energy is set to $\mu = 0$. Thus, the fluctuation-dissipation theorem holds, and:

$$\Delta^<(\omega) = -e^{\beta\omega} \Delta^>(\omega) \quad (6.76)$$

As a consequence, since the bath spectral function reads $A(\omega) = \frac{1}{2\pi} (i\Delta^<(\omega) - i\Delta^>(\omega))$ one can readily show that

$$\frac{\Delta^<(\omega)}{2i\pi} = A(\omega)f(\omega) \quad (6.77)$$

$$\frac{\Delta^>(\omega)}{-2i\pi} = A(\omega)(1 - f(\omega)) \quad (6.78)$$

where $f(\omega)$ is the Fermi distribution at inverse temperature β :

$$f(\omega) = \frac{1}{1 + e^{\beta\omega}} \quad (6.79)$$

We consider the fit of the imaginary part of the greater hybridization, $-i\Delta^>(\omega)$, associated with a semi-circular spectral function $A(\omega)$ of unit bandwidth $D = 1$, namely:

$$A(\omega) = \frac{4}{\pi D} \sqrt{1 - \left(\frac{2\omega}{D}\right)^2} \quad (6.80)$$

so that we aim at fitting

$$-i\Delta^>(\omega) = \frac{8}{D} \sqrt{1 - \left(\frac{2\omega}{D}\right)^2} (1 - f(\omega)) \quad (6.81)$$

with a number n_b of bath sites dissipating at rate Λ . We plot the value of the optimized cost function (optimized with the COBYLA minimizer) as a function of n_b for up to 20 sites and as a function of Λ , for different values of $\beta = 0.1, 10, 100$. We

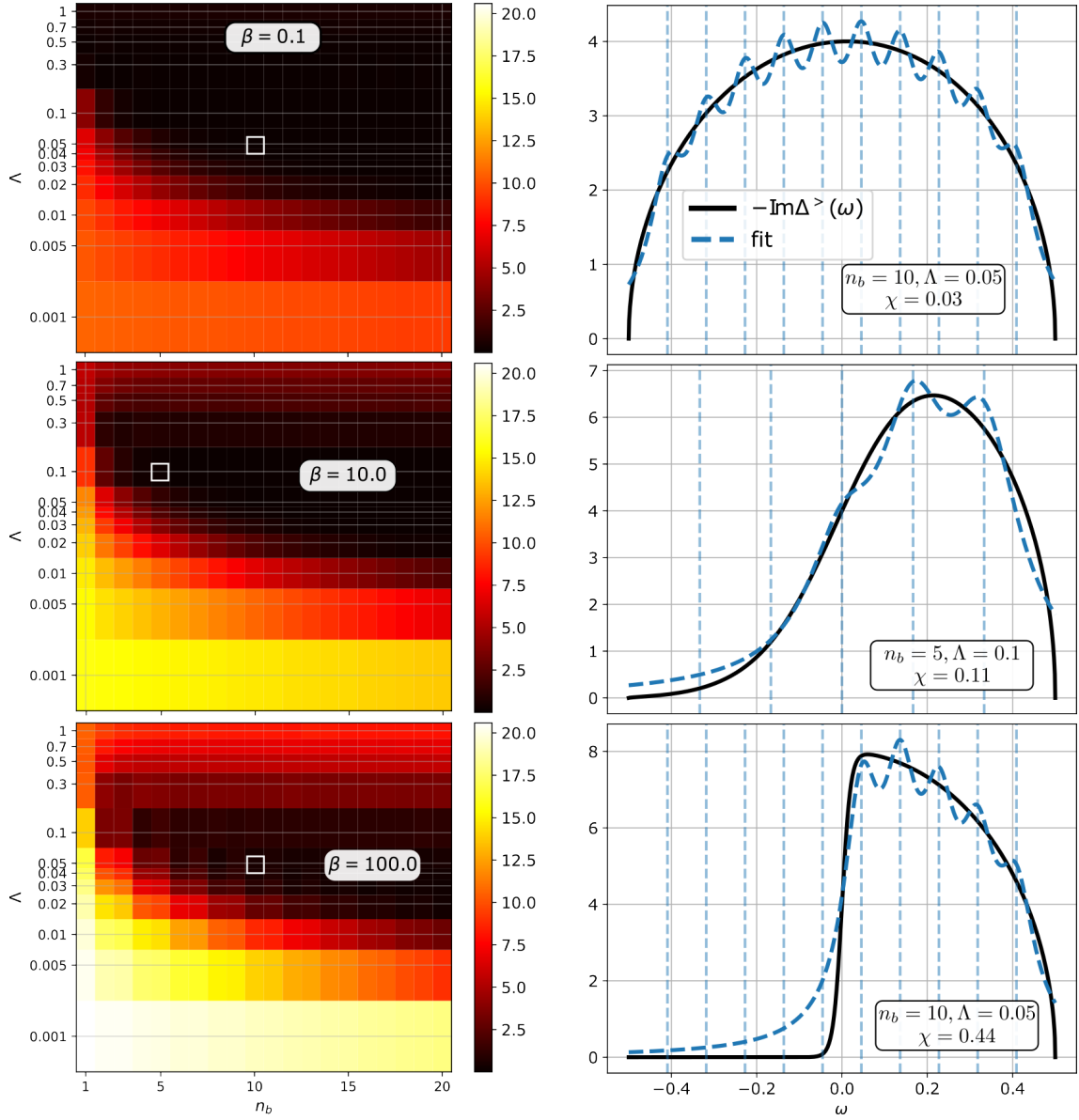


Figure 6.9: Cost functions associated with optimal fit as a function of the number of bath sites n_b and the intensity of dissipation Λ , for different temperatures (left). Optimization done with COBYLA minimizer, fixed grid of energies. The scale of the y axis is logarithmic. On the right, the fits corresponding to the white squares on the left are displayed. The dashed lines materialize the energies of the bath levels.

obtain the results plotted on Figure 6.9. We observe that the fit becomes more and more difficult as the temperature increases. The quality of the fit is lowest when Λ is close to 0, and when n_b is small. Turning dissipation on is shown to have a favourable effect. Yet, at some point, noise becomes detrimental to the fit: although this is not visible in the $\beta = 0.1$ plot due to the restricted range of Λ values investigated, we observe that at a given number of bath sites, the quality of the fit increases with Λ but then decreases. This mirrors the fact that the peaks are then too wide to resolve the quickly-varying parts of the hybridization. All in all, the advantage of having dissipative bath sites is validated in all three settings. Qubit noise might indeed be a valuable resource in the end!

This, of course, simply constitutes a first proof-of-principle of the approach. The fit of hybridizations arising from a DMFT loop should be tested for. Then, a second step would be to observe the dissipative bath approach within the DMFT loop: how do the fit errors impact the convergence of the DMFT loop? Finally, the method should be tested on real quantum hardware. Since the optimization procedure for the fit relies on the assumption that the jump operators are fermionic operators, whether the optimized parameters will remain good parameters for the fit in a realistic setting is an open question. If not, one might still be able to derive Equations similar to Equations 6.58 for the qubit dissipation, and thus the scheme might successfully be adapted.

6.7 Influence of the encoding onto the dissipative dynamics

Using numerical integration, we can solve the master equations associated with both types of two-point correlators involved in the Green's functions (see Equations 6.54, 6.55) and in the time evolution of the density matrix.

We consider here the minimal { impurity + bath } system for which the form of the jump operators, either the Jordan-Wigner-transformed c_p^\dagger, c_p associated with bath modes or the ladder operators Q_p^\dagger, Q_p (introduced in 4.2 and recalled below), might have an impact. We consider spinless fermions. The impurity, associated with creation and annihilation operators d, d^\dagger , is taken to be uncorrelated so that the Hamiltonian remains quadratic. We define:

$$\mathcal{H} = \sum_{p=1}^2 V (d^\dagger c_p + \text{h.c.}) \quad (6.82)$$

where $V = 1$. The impurity is indexed 0.

The jump operators in Lindblad equation are the L_k which are either:

1. $\{L_k\} = \{\Lambda c_p^\dagger, \Lambda c_p\}$ which map onto $\{\Lambda (\otimes Z)^{p-1} \otimes Q_p^\dagger, \Lambda (\otimes Z)^{p-1} \otimes Q_p\}$
2. $\{L_k\} = \{\Lambda Q_p^\dagger, \Lambda Q_p\}$, to be understood as $\{L_k\} = \{\Lambda (\otimes I_2)^{p-1} \otimes Q_p^\dagger, \Lambda (\otimes I_2)^{p-1} \otimes Q_p\}$

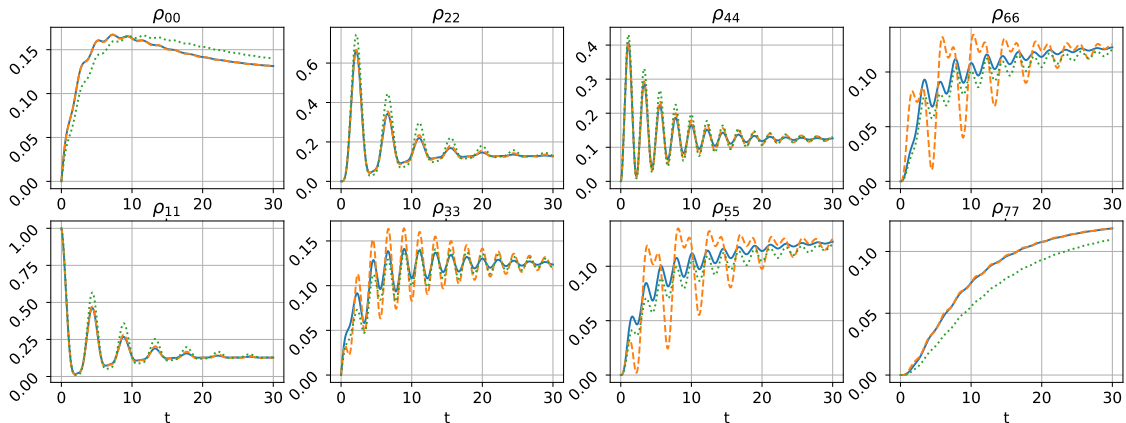


Figure 6.10: Evolution of real part of diagonal density matrix elements with t , for a 2 bath-site system with fermionic dissipation (in blue) and qubit dissipation (in orange), $\Lambda = 0.1$, starting from the same state. The dotted green line represents the dynamics with qubit dissipation, rescaled as $\Lambda' = \frac{\Lambda}{\sqrt{2}}$.

with Q_p^\dagger the qubit operator

$$Q_p^\dagger = |1\rangle \langle 0|_p = \frac{1}{2} (X_p - iY_p). \quad (6.83)$$

and $\Lambda = 0.1$. We will refer to the first process as *fermionic dissipation*. It was modelled as dissipation over qubits through Jordan-Wigner encoding, introduced in 4.2. The second method will be referred to as *qubit dissipation*: compared with the latter, we simply drop the Z chains of the Jordan-Wigner-encoded jump operators.

The diagonal elements of the density matrix at time t are displayed for the two kinds of dissipation on Figure 6.10. The systems were initialized in the same state ρ_0 where $(\rho_0)_{11} = 1$ and $(\rho_0)_{ij} = 0$ for $(i, j) \neq (1, 1)$. $\rho_{ii}(t)$ gives the probability to measure the system in basis state i . We adopt the little-endian convention: the highest-weight qubit is on the right of the bistring. Thus, state 1 corresponds to $|100\rangle$ which according to the ordering convention of the modes corresponds to the impurity being occupied whereas the bath sites are empty. We observe that the two-fermion basis states differ the most between the two processes. The effect of the chains of Z operators is observed to be that oscillations are more damped. However, the two systems share the same steady-state (the non-diagonal elements of $\rho(t)$, not displayed here, also tend to the same values). These observations are in accordance with that reported in [113].

Finally, by rescaling the fermionic dissipative process by setting $\Lambda = 0.1 \rightarrow \Lambda' = \frac{0.1}{\sqrt{2}}$ (dashed green lines in Figure 6.10) we can make the two-fermion states display similar dynamics, but at the expense of the other states. Thus, the two processes seem qualitatively similar but quantitatively different. As a consequence, the possibility to adapt this fermionic dissipative bath scheme to dissipative bath sites represented on a qubit register picking up environmental noise remains open. In particular, the encoding technique provides a lever which may be put to advantage.

6.8 Conclusion

In this chapter, we tackled the problem of bath truncation by considering a dissipative bath scheme. We adapted the algorithm of [102, 103, 104] to a quantum-classical context, by devising a quantum-classical DMFT algorithm which uses hardware noise as a resource for the fit of the DMFT hybridizations. Noise provides widened peaks which are associated to reduced requirements over the bath site count in terms of quality of the fit. This was illustrated on toy hybridizations at several temperatures. The method should now be tested on a wider variety of hybridizations, such as the set of hybridizations arising along a given DMFT loop. Then, the stability of the method within the DMFT loop should be assessed.

At the more fundamental level, the method assumes that qubits relax with fermionic jump operators. That contradicts the spin nature of qubits, but it is the work hypothesis which underlies the derivation of the form of the auxiliary hybridization brought about by the dissipative bath. It is not excluded that qubit damping exhibits rescaled dynamics compared with the fermionic process. Otherwise, one should either turn to recently-proposed fermionic platforms [111] or might play with the encoding to get similar dynamics.

Conclusion

In this thesis, we have described new algorithms for the hybrid quantum-classical study of strongly-correlated systems in the presence of noise at the level of the quantum hardware.

The scope of this thesis was embedding methods such as the celebrated Dynamical Mean-Field Theory (DMFT) method. DMFT solves the Hubbard model by mapping it to a proxy impurity model, which consists in a cell of a few correlated impurities exchanging particles with a free-fermion bath. Spatial resolution of correlation effects is achieved through the resorting to a multiple-impurity model, the size of the cell constituting a lever for systematic improvement. Moreover, the DMFT construction implies an infinite bath, as bath truncation significantly diminishes the representational power of the impurity model. In this thesis we addressed both of these impediments to DMFT.

We first put forth an algorithmic strategy which tops plain-vanilla variational quantum state preparation with single-particle basis updates which increase the quality of the variational approximation to the target state. We proposed an alternative scheme in which the variational state preparation step is adaptive, so as to allow for reduced gate count along the single-particle basis update procedure. Conversely to other methods proposed recently, our method does not properly speaking optimize for the single-particle basis, but updates it sequentially, guided by one-particle reduced density matrix information. These methods were shown to display nearly-systematic improvement in terms of energy of the attained state, and enabled us to run successfully for the first time a two-impurity embedding scheme. On the flip side, orbital updates are associated with a measurement overhead due to the multiplication of the number of terms in the Hamiltonian to be measured which limits their scope to noise levels above a certain threshold.

Secondly, we tackled the problem of bath truncation by considering a dissipative bath scheme. Originally devised in a classical computation context, this scheme is argued to lend for a very promising quantum-classical implementation. The proposed scheme consists in leveraging the dissipation which is naturally at work in current quantum platforms in order to get widened peaks for the fit of the DMFT

hybridization. We show on a toy set of hybridizations that the extended capabilities in terms of fit enabled by dissipative bath sites allows to reduce the bath site count. The proof-of-principle of the algorithm remains to be further investigated, along with the impact of considering the effective dissipation processes at work in qubits.

Published work

I have published the two following papers:

- P.Besserve and T.Ayral, *Unraveling correlated materials' properties with noisy quantum computers: Natural-orbitalized variational quantum eigensolving of extended impurity models within a slave-boson approach*, Physical Review B 105 (11) (2022) 115108, publisher: American Physical Society,
- T.Ayral, P.Besserve, D.Lacroix and A.E. Ruiz-Guzman, *Quantum computing with and for many-body physics*, preprint (Mar 2023), <https://arxiv.org/abs/2303.04850>, in press (European Physical Journal A),

which are appended below.

Additionally, I have two manuscripts in preparation:

- *Noise-robust circuit and representation learning : Natural-Orbitalizing Adaptive Variational Quantum Eigensolver (NOA-VQE)*,
- *Noise-assisted impurity solving.*

Appendices

Appendix A

Diagonalization of quadratic Hamiltonians

Here we show that a quadratic Hamiltonian, of the form

$$\mathcal{H} = \sum_{p,q} h_{pq} c_p^\dagger c_q \quad (\text{A.1})$$

(where $h = h^\dagger$) can be diagonalized, and that its eigenstates follow naturally.

There are two equivalent ways to diagonalize \mathcal{H} . The first, more mathematical, consists simply in remarking that since h is hermitian, it can be diagonalized:

$$h = h^\dagger \implies h = P\Delta P^\dagger, \Delta = \text{diag}(\varepsilon_1, \dots, \varepsilon_m)$$

Plugging this decomposition of h into Equation A.1 one gets

$$\begin{aligned} \mathcal{H} &= \sum_{p,q} \sum_k P_{pk} \varepsilon_k (P^\dagger)_{kq} c_p^\dagger c_q \\ &= \sum_k \varepsilon_k \underbrace{\left(\sum_p P_{pk} c_p^\dagger \right)}_{\tilde{c}_k^\dagger} \underbrace{\left(\sum_q P_{qk}^* c_q \right)}_{\tilde{c}_k} \\ &= \sum_k \varepsilon_k \tilde{c}_k^\dagger \tilde{c}_k \end{aligned}$$

The second method, not expanded here, is more physical and holds for translationally-invariant $h_{pq} = h_{|p-q|}$. It consists in writing the creation/annihilation operators, which corresponds to spatially-localized modes, in the Fourier basis.

$$c_p^\dagger = \frac{1}{\sqrt{N}} \sum_{\mathbf{k}} e^{i\mathbf{k}\cdot\mathbf{p}} c_{\mathbf{k}}^\dagger \quad (\text{A.2})$$

where \mathbf{k} corresponds to points in the first Brillouin zone of the reciprocal space and N corresponds to the number of spatial modes. It becomes clear then why we chose to label with k the diagonalization basis of \mathcal{H} .

The eigenstates are then simply obtained by filling the k modes with increasing energies $\sum_{k \in \text{filled}} \epsilon_k$. Filling modes $j = 0, \dots, m - 1$ among the k modes is associated with energy $\sum_j \epsilon_j$. In particular, the ground state reads:

$$|\psi_0\rangle = \left(\prod_{k/\epsilon_k < 0} \tilde{c}_k^\dagger \right) |\bar{0}\rangle \quad (\text{A.3})$$

Appendix **B**

Fourier transform

We take the following convention for the Fourier transform: let $f(t)$ be a time-dependent function, we define its Fourier transform in the frequency-domain as

$$F(\omega) = \int_{-\infty}^{+\infty} dt e^{i\omega t} f(t) \quad (\text{B.1})$$

and we make the notational simplification $F(\omega) \rightarrow f(\omega)$.

For two-time functions verifying time-translation invariance $G(t, t') = G(t - t', 0)$ we define similarly

$$G(\omega) = \int_{-\infty}^{+\infty} dt e^{i\omega t} G(t, 0) \quad (\text{B.2})$$

Reciprocally to Equation B.1, we have

$$f(t) = \frac{1}{2\pi} \int_{-\infty}^{+\infty} dt e^{-i\omega t} f(\omega). \quad (\text{B.3})$$

Appendix C

List of definitions of Green's functions

Let's recall the expressions for all local two-time Green's functions relative to some level d (to be thought here as one of the spin components of the impurity level):

$$G^R(t, t') = -i\Theta(t - t')\langle\{d(t), d^\dagger(t')\}\rangle \quad (\text{C.1})$$

$$G^A(t, t') = +i\Theta(t' - t)\langle\{d(t), d^\dagger(t')\}\rangle \quad (\text{C.2})$$

$$G^K(t, t') = i\langle[d^\dagger(t'), d(t)]\rangle \quad (\text{C.3})$$

$$G^T(t, t') = -i\langle\mathcal{T}d(t)d^\dagger(t')\rangle \quad (\text{C.4})$$

$$G^{\bar{T}}(t, t') = -i\langle\bar{\mathcal{T}}d(t)d^\dagger(t')\rangle \quad (\text{C.5})$$

$$G^<(t, t') = i\langle d^\dagger(t')d(t)\rangle \quad (\text{C.6})$$

$$G^>(t, t') = -i\langle d(t)d^\dagger(t')\rangle \quad (\text{C.7})$$

where \mathcal{T} is the time ordering operator¹, so that for fermion operators A and B we have $\mathcal{T}A(t)B(t') = A(t)B(t')$ if $t > t'$ but $\mathcal{T}A(t)B(t') = -B(t')A(t)$ if $t < t'$. $\bar{\mathcal{T}}$ is the anti-time ordering operator. These definitions readily extend to non-local Green's functions, with site indices i and j .

We define $\langle A \rangle \equiv \text{Tr}(\rho A)$, which in this work will correspond either to $\langle \psi_0 | A | \psi_0 \rangle$ with $|\psi_0\rangle$ the ground state of the system, or to $\text{Tr}(\rho_{\text{NESS}} A)$ with ρ_{NESS} the non-equilibrium steady-state.

The greater $G^>$ and lesser $G^<$ Green's functions are sometimes referred to as (Kadanoff-Baym's) electron resp. hole propagators, they fully characterize the single-electron dynamics in the solid.

These functions are related as

¹The corresponding Green's function is sometimes called the Feynman propagator.

$$G^R(t, t') = \Theta(t - t')(G^>(t, t') - G^<(t, t')) \quad (\text{C.8})$$

$$G^K(t, t') = G^T(t, t') + G^{\bar{T}}(t, t') = G^<(t, t') + G^>(t, t') \quad (\text{C.9})$$

$$G^R(t, t') - G^A(t, t') = G^>(t, t') - G^<(t, t') \quad (\text{C.10})$$

$$G^T(t, t') = \Theta(t - t')G^>(t, t') + \Theta(t' - t)G^<(t, t') \quad (\text{C.11})$$

Both in equilibrium and in a steady state we have time-translation invariance, so that $G(t, t') = G(t - t', 0)$ and we can write the Fourier transforms of these functions (see Appendix B).

In Fourier space we have the relations

$$G^R(\omega) \equiv \lim_{\eta \rightarrow 0^+} G^R(\omega + i\eta) \quad (\text{C.12})$$

$$G^A(\omega) \equiv \lim_{\eta \rightarrow 0^-} G^A(\omega + i\eta) = G^R(\omega)^\dagger \quad (\text{C.13})$$

$$A(\omega) \equiv -\frac{1}{\pi} \text{Im}G^R(\omega) \quad (\text{C.14})$$

$$G^K(\omega) = G^<(\omega) + G^>(\omega) \quad (\text{C.15})$$

$$G^K(\omega)^\dagger = -G^K(\omega) \quad (\text{C.16})$$

$$\text{Re}G^R(\omega) = \frac{1}{\pi} \text{P.V.} \int_{\mathbb{R}} d\omega' \frac{\text{Im}G^R(\omega')}{\omega' - \omega} \quad (\text{C.17})$$

where $A(\omega)$ is the so-called *spectral function*. The last equation involves Cauchy principal value. It is the Kramers-Kronig relation, relating real and imaginary parts of the Fourier transform of a causal function. It is only a consequence of the analyticity in the upper-half plane of such functions.

Combining Eqs (C.14), (C.13) and (C.10) we have $2i\text{Im}G^R(\omega) = G^>(\omega) - G^<(\omega)$ and thus

$$A(\omega) = \frac{1}{2\pi} (iG^<(\omega) - iG^>(\omega)) \quad (\text{C.18})$$

Equivalence between analyticity in the upper half-plane and causality, Kramers-Kronig relations

We want to prove that a causal function, $\gamma(t) \propto \Theta(t)$, admits a Fourier transform $\gamma(\omega)$ which upon prolongation to the complex plane is analytic in the upper-half complex plane, and reciprocally. We then show Kramers-Kronig relations, which connect the real and the imaginary parts of $\gamma(\omega)$.

Let's prove first that if the Fourier transform $\gamma(\omega)$ of $\gamma(t)$ prolonged to the complex plane is analytic in the upper-half complex plane, then $\gamma(t) = 0 \forall t < 0$. We decompose the complex variable $\omega = \omega_1 + i\omega_2$:

$$\gamma(t) = \int_{-\infty}^{+\infty} \frac{d\omega}{2\pi} e^{-i\omega_1 t + \omega_2 t} \gamma(\omega) = \lim_{R \rightarrow \infty} \int_{-R}^{+R} \frac{d\omega}{2\pi} e^{-i\omega_1 t + \omega_2 t} \gamma(\omega) \quad (\text{D.1})$$

Then for $t < 0$ and $\omega_2 > 0$, $|e^{\omega_2 t}| \rightarrow 0$ as $\omega_2 \rightarrow \infty$ and we can thus close the contour with an arc in the upper-half plane (a semi-circle of radius R) without changing the value of the integral (in virtue of Jordan's lemma). The integrated function being analytical in the enclosed surface by hypothesis, there are no poles there and Cauchy theorem ensures that:

$$\gamma(t) = \oint \frac{d\omega}{2\pi} e^{-i\omega_1 t + \omega_2 t} \gamma(\omega) = 0 \quad (\text{D.2})$$

Conversely, suppose $\gamma(t) = 0 \forall t < 0$. Then

$$\gamma(\omega) = \int_0^{+\infty} dt e^{i\omega t} \gamma(t) \quad (\text{D.3})$$

is well-defined for any $\omega = \omega_1 + i\omega_2$ with $\omega_2 > 0$ due to the vanishing exponential $e^{-\omega_2 t}$. For $\omega_2 = 0$, meaning $\omega \in \mathbb{R}$, the integral is well-defined as the Fourier transform is.

Now, let's see how this translates into the Kramers-Kronig relation, meaning it implies that the real and imaginary parts of γ causal are linked (each being more specifically the Hilbert transform of the other).

For that we consider the integral $\oint_{\mathcal{C}} \frac{d\omega'}{2\pi} \frac{\gamma(\omega')}{\omega' - \omega}$ where the contour \mathcal{C} consists of three parts:

- two branches on the real axis, one from $-R$ to $\omega - \delta$ and the other one from $\omega + \delta$ to $+R$
- the half-circle of radius δ , \mathcal{C}^δ , circling ω in the upper-half plane
- the half-circle of radius R , \mathcal{C}^R , going in the upper-half-plane

Due to the analyticity of $\gamma(\omega)$ in the upper-half-plane and the fact that the contour avoids the pole ω due to the denominator of the integrand, Cauchy theorem ensures that

$$\oint_{\mathcal{C}} \frac{d\omega'}{2\pi} \frac{\gamma(\omega')}{\omega' - \omega} = 0 \quad (\text{D.4})$$

We suppose that $|\gamma(\omega)|$ vanishes as ω goes to zero (otherwise one has to subtract $\gamma(\infty)$ to $\gamma(\omega')$ in the formula for the proof to go on), so that we can extend the contour with $R \rightarrow \infty$ and $\delta \rightarrow 0$. Then:

- the real-axis part of the integral yields P.V. $\int_{\mathbb{R}} \frac{d\omega'}{2\pi} \frac{\gamma(\omega')}{\omega' - \omega}$ where P.V. indicates we take the Cauchy principal value (this operation consists in giving a value to an otherwise undefined integral by considering a symmetric avoiding of its pole and taking the limit as we go closer to the pole)
- the \mathcal{C}_δ gives $\lim_{\delta \rightarrow 0} \int_{\pi}^0 \frac{i\delta e^{i\theta}}{2\pi} \frac{\gamma(\omega + \delta e^{i\theta})}{\delta e^{i\theta}} = -\frac{i}{2}\gamma(\omega)$
- the \mathcal{C}_R part vanishes due to the vanishing of the integrand (Jordan's lemma).

We are left with

$$\frac{i}{2}\gamma(\omega) = \text{P.V.} \int_{\mathbb{R}} \frac{d\omega'}{2\pi} \frac{\gamma(\omega')}{\omega' - \omega} \quad (\text{D.5})$$

By decomposing $\gamma(\omega)$ into a real and an imaginary part $\gamma(\omega) = \gamma'(\omega) + i\gamma''(\omega)$ and identifying the real and imaginary parts in the formula above, we get the Kramers-Kronig relations:

$$\gamma'(\omega) = \frac{1}{\pi} \text{P.V.} \int_{\mathbb{R}} d\omega' \frac{\gamma''(\omega')}{\omega' - \omega} \quad (\text{D.6})$$

$$\gamma''(\omega) = -\frac{1}{\pi} \text{P.V.} \int_{\mathbb{R}} d\omega' \frac{\gamma'(\omega')}{\omega' - \omega} \quad (\text{D.7})$$

Appendix E

Resonant level model

In this Appendix, in order to highlight the physical content of the self-energy we turn to a simple model of a non-interacting site, the 'resonant level', coupling with a conduction band.

We consider the following non-interacting Hamiltonian describing one site d coupled to "bath" sites c :

$$H = \epsilon_d d^\dagger d + \sum_k \epsilon_k c_k^\dagger c_k + t \sum_k (c_k^\dagger d + d^\dagger c_k) \quad (\text{E.1})$$

(since we do not consider any interaction on the site d , we do not consider the spin degeneracy of the levels).

Self-energy The local Green's function in Matsubara frequencies is defined as the matrix element

$$G_d(i\omega_n) = [(i\omega_n - H_1)^{-1}]_{00} \quad (\text{E.2})$$

where H_1 is the single-particle Hamiltonian whose definition will become clear from the calculation below.

Writing the matrix $i\omega_n - H_1$ in block form

$$i\omega_n - H_1 = \begin{pmatrix} A & B \\ C & D \end{pmatrix} \quad (\text{E.3})$$

with

$$\begin{aligned}
A &= (i\omega_n - \epsilon_d) \\
B &= (-t \quad -t \quad \dots \quad -t) \\
C &= B^T \\
D &= \begin{pmatrix} i\omega_n - \epsilon_1 & 0 & 0 & \dots & 0 \\ 0 & i\omega_n - \epsilon_2 & 0 & & 0 \\ \vdots & & & & \\ 0 & & & & i\omega_n - \epsilon_K \end{pmatrix}
\end{aligned}$$

it is easy to find $G_d(i\omega_n)$, the top-left corner coefficient of its inverse:

$$\begin{aligned}
G_d(i\omega_n) &= (A - BD^{-1}C)^{-1} \\
&= \frac{1}{i\omega_n - \epsilon_d - t^2 \sum_k \frac{1}{i\omega_n - \epsilon_k}}
\end{aligned}$$

To get the retarded Green's function, we carry out an analytic continuation to the real axis, $i\omega_n \rightarrow \omega + i\eta$ with $\eta = 0^+$:

$$G_d^R(\omega) = \frac{1}{(\omega - \epsilon_d - \Sigma'(\omega)) + i(\eta - \Sigma''(\omega))} \quad (\text{E.4})$$

where we have defined the self-energy $\Sigma(\omega) \equiv t^2 \sum_k \frac{1}{\omega + i\eta - \epsilon_k} = \Sigma'(\omega) + i\Sigma''(\omega)$. In this context, the self-energy is also called the *hybridization*.

Spectral function The spectral function is defined as $S(\omega) = -\frac{1}{\pi} \text{Im}(G_d^R(\omega))$. In the illustration plots, we consider a model with $\epsilon_d = 0$, $\epsilon_k = [-1, -1, 1, 1]$ and $t = 1$.

Here we get from the definition above:

$$S(\omega) = \frac{1}{\pi} \frac{\eta - \Sigma''(\omega)}{(\omega - \epsilon_d - \Sigma'(\omega))^2 + (\eta - \Sigma''(\omega))^2} \quad (\text{E.5})$$

Here the η factor makes sense only numerically: it corresponds to the Lorentzian widening of the delta peaks. It must be chosen according to the ω resolution.

Poles the spectral function will have a pole at $\omega = \omega_p$ if the following conditions are satisfied:

- $\Sigma'(\omega_p) = \omega_p - \epsilon_d$
- $\Sigma''(\omega_p)$ is finite, the closer to zero, the more pronounced the peak since if the condition above is satisfied, $S(\omega_p) \simeq \frac{1}{\Sigma''(\omega_p)}$

This can be visualized on Figure E.1.

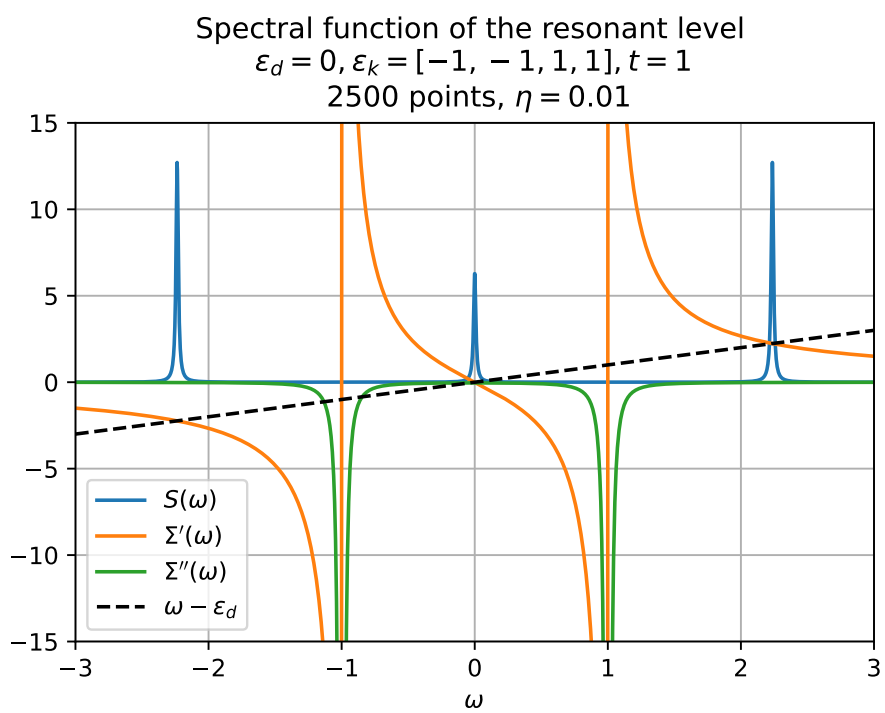


Figure E.1: Spectral function and self-energy elements associated with the model E.1.

Appendix **F**

Grassmann variables

Grassmann variables are the eigenvalues of the annihilation operators associated to so-called 'coherent states' (which are not physical states in the case of fermions, but also span the Fock space, as an alternative to Slater permanents/determinants). They are characterized by their algebra $[\eta_1, \eta_2]_\xi = 0$ where, with $\xi = +1$ for bosons and $\xi = -1$ for fermions, we define $[\cdot, \cdot]_1 = [\cdot, \cdot]$ and $[\cdot, \cdot]_{-1} = \{\cdot, \cdot\}$. For bosons, they are simply complex numbers. Just as z and z^* are independent in complex analysis, η and η^\dagger denote independent variables.

Importantly, Grassmann variables obey the following relations:

$$\begin{aligned}\eta^2 &= 0 \\ \int d\eta &= 0 \\ \int d\eta \eta &= 1\end{aligned}$$

Deriving and integrating with regards to a Grassmann variable is thus the same operation. Any function of Grassman variables is at most of order one in any of the variables.

Appendix G

Gaussian integral

Real case Let $A \in \mathcal{S}_n(\mathbb{R})^{++}$ be a positive definite matrix and $\mathbf{b} \in \mathbb{R}^n$ a vector. Then

$$\int_0^{+\infty} d\mathbf{x} e^{-\frac{1}{2}\mathbf{x} \cdot A \mathbf{x} + \mathbf{b} \cdot \mathbf{x}} = e^{\frac{1}{2}\mathbf{b} \cdot A^{-1} \mathbf{b}} \frac{(2\pi)^{n/2}}{\sqrt{\det A}} \quad (\text{G.1})$$

Proof: The first change of variable $\mathbf{y} = \mathbf{x} - A^{-1}\mathbf{b}$ allows to see that the linear term yields a prefactor. Then, one just has to work in the diagonalization basis of A , which is a transformation with unity Jacobian, to transform the multivariate integral into a product of one-variable integral of the form $\int_0^{+\infty} dx^{-ax^2} = \sqrt{\frac{\pi}{a}}$.

In Grassmann variables The Gaussian integral in Grassman/complex variables reads [114]:

$$\int d\mu(\xi) e^{-\sum_{\alpha,\beta} \xi_\alpha^\dagger A_{\alpha\beta} \xi_\beta + \sum_\alpha (\eta_\alpha^\dagger \xi_\alpha + \eta_\alpha \xi_\alpha^\dagger)} = (\det(A))^{-\zeta} e^{\sum_{\alpha,\beta} \eta_\alpha^\dagger (A^{-1})_{\alpha\beta} \eta_\beta} \quad (\text{G.2})$$

with $\zeta = -1$ for fermions/ $\zeta = 1$ for bosons, A any invertible matrix for fermions but one with a positive definite hermitian part for bosons, and the integration measure $d\mu(\xi) = \prod_j d\xi_j^\dagger d\xi_j$ for fermions, $d\mu(\xi) = \frac{1}{2\pi i} \prod_j d\xi_j^\dagger d\xi_j$ for bosons. The second term in the exponential that makes the integrand corresponds to so-called *source fields*.

Appendix **H**

Tracing out bath degrees of freedom in an action-based representation

Here, we want to show that by integrating out the bath degrees of freedom in the partition function associated to an impurity model (where the bath sites lie at energies ϵ_p and couple to the impurity with hoppings V_p), we are left with an action displaying an hybridization $\Delta(i\omega_n) = \sum_p \frac{|V_p|^2}{i\omega_n - \epsilon_p}$.

The derivation is based on [114]. To work through the integration of the fermionic fields, we need a powerful tool which are Grassmann variables introduced in Appendix F as well as the evaluation of the Gaussian integral which is presented in Appendix G.

We consider the following Hamiltonian of a correlated impurity coupled to a fermionic bath:

$$H = U d_{\uparrow}^{\dagger} d_{\uparrow} d_{\downarrow}^{\dagger} d_{\downarrow} - \mu (d_{\uparrow}^{\dagger} d_{\uparrow} + d_{\downarrow}^{\dagger} d_{\downarrow}) + \sum_{p\sigma} \epsilon_p f_{p\sigma}^{\dagger} f_{p\sigma} + \sum_{p\sigma} V_p (f_{p\sigma}^{\dagger} d_{\sigma} + \text{h.c.}) \quad (\text{H.1})$$

Let's integrate out all bath degrees of freedom (corresponding to f terms) in the partition function

$$Z = \text{Tr}(e^{-\beta\mathcal{H}}) \equiv \int dq \langle q | e^{-\beta\mathcal{H}} | q \rangle = \int_{\xi_j(0)=\zeta \xi_j(\beta)} \mathcal{D}[\{\xi_j^{\dagger}, \xi_j\}] e^{-S[\{\xi_j^{\dagger}, \xi_j\}]} \quad (\text{H.2})$$

In the above, q refers to a generalized coordinate in phase space whereas the last equality corresponds to Feynman's construction of the path integral, it is a 'sum over all paths' stemming from the insertion of many resolutions of the identity. Note that we have taken $\hbar = 1$.

We recall that the imaginary-time, 'euclidean' action is obtained from the Hamiltonian (rather than the Lagrangian in real time) as

$$S = \int_0^{\beta} d\tau \left(\sum_j \xi_j^{\dagger} \partial_{\tau} \xi_j + H(\xi_j^{\dagger}, \xi_j) \right) \quad (\text{H.3})$$

where the ξ_j denote either Grassmann variables (for fermionic fields) or complex numbers (for bosonic ones) and the \dagger superscript corresponds to conjugation in the corresponding algebra. The Hamiltonian term corresponds to the operator Hamiltonian in which we have replaced the annihilation/creation operators by their coherent state counterpart. Here the integration over imaginary time is the continuum limit, but in accordance with Feynman's construction of the path integral the expression must be seen as a big vector-matrix-vector product, with continuous variable τ corresponding to a set of variables τ_i . One can thus write the integral and work with a superindex for the fields that corresponds both to the different modes and to the different times instead.

The derivation relies on the Gaussian integral presented in Appendix G: we thus just have to identify A and the source fields to carry out the integration.

We first make the imaginary time integration disappear by going to Matsubara space, expanding the operators in Fourier series $\eta(\tau) = \frac{1}{\beta} \sum_n \eta(i\omega_n) e^{-i\omega_n \tau}$. For given indices p, σ :

$$\begin{aligned} \int d\tau f_{p\sigma}^\dagger(\tau) (\partial\tau + \epsilon_p) f_{p\sigma}(\tau) &= \frac{1}{\beta^2} \int d\tau \left(\sum_n f_{p\sigma}^\dagger(i\omega_n) e^{i\omega_n \tau} \right) (\partial\tau + \epsilon_p) \left(\sum_m f_{p\sigma}(i\omega_m) e^{-i\omega_m \tau} \right) \\ &= \frac{1}{\beta^2} \sum_{mn} \left(\underbrace{\int d\tau e^{i(\omega_n - \omega_m)\tau}}_{\beta \delta_{mn}} \right) f_{p\sigma}^\dagger(i\omega_n) (-i\omega_m + \epsilon_p) f_{p\sigma}(i\omega_m) \\ &= \frac{1}{\beta} \sum_n f_{p\sigma}^\dagger(i\omega_n) (-i\omega_n + \epsilon_p) f_{p\sigma}(i\omega_n) \end{aligned}$$

and similarly

$$\int d\tau V_p (f_{p\sigma}^\dagger(\tau) d_\sigma(\tau) + h.c.) = \frac{1}{\beta} \sum_m V_p (f_{p\sigma}^\dagger(i\omega_m) d_\sigma(i\omega_m) + h.c.)$$

The term in the gaussian exponential to integrate for f fields is thus (omitting the β factor)

$$- \sum_{jj'} f_j^\dagger A_{jj'} f_{j'} + \sum_j (f_j^\dagger (V_j d_j) + h.c.)$$

where we have introduced a superindex $j = (\sigma, p, n)$. The matrix A is diagonal and invertible, and its elements are of the form $i\omega_n - \epsilon_p$ ¹. Now we can apply Formula

¹Note the change in the signs, coming from the fact we want to put the integrand in the correct form for Gaussian integration. Also, note how we have displaced the coefficients V_j to identify the fields our fields to integrate out couple with.

G.2 to find that up to a proportionality coefficient, the integrating out of f fields leaves us with $e^{\sum_{np\sigma} f_{p\sigma}^\dagger(i\omega_n)\Delta_{p\sigma}(i\omega_n)f_{p\sigma}(i\omega_n)}$ where

$$\Delta_{p\sigma}(i\omega_n) = \frac{|V_p|^2}{i\omega_n - \epsilon_p}. \quad (\text{H.4})$$

Finally, note that by going by to imaginary time we have to define a retarded hybridization

$$\Delta_{p\sigma}(\tau - \tau') = \sum_{nk} e^{-i(\tau - \tau')\omega_n} \frac{|V_p|^2}{i\omega_n - \epsilon_p} \quad (\text{H.5})$$

hence the effect of the bath to bring about a dynamics onto hopping processes.

Computation of Green's function elements

Here we show that $T_{kl} \equiv \langle \psi_0 | U^\dagger(t) \sigma^k U(t) \sigma^l | \psi_0 \rangle$ with $U(t) = e^{-iHt}$ is accessible upon measurements over the ancillary qubit of circuit 4.3 as:

$$T_{kl} = \langle Z \rangle + i \langle Y \rangle \quad (\text{I.1})$$

The state at the end of the circuit reads:

$$|\psi\rangle = \frac{1}{2}(|0\rangle \otimes |\alpha\rangle + |1\rangle \otimes |\beta\rangle)$$

with

$$\begin{aligned} \alpha &= U(t)(I + V(t)) |\psi_0\rangle \\ \beta &= U(t)(I - V(t)) |\psi_0\rangle \\ V(t) &= U^\dagger(t) \sigma^k U(t) \sigma^l \end{aligned}$$

so that

$$\begin{aligned} \langle Z \rangle &= \text{Tr}(Z |\psi\rangle \langle \psi|) \\ &= \text{Tr}(|0\rangle \langle 0| - |1\rangle \langle 1|) |\psi\rangle \langle \psi| \\ &= \langle \psi | 0 \rangle \langle 0 | \psi \rangle - \langle \psi | 1 \rangle \langle 1 | \psi \rangle \\ &= \frac{1}{4} (\langle \alpha | \alpha \rangle - \langle \beta | \beta \rangle) \end{aligned}$$

Since

$$\begin{aligned} \langle \alpha | \alpha \rangle &= \langle \psi_0 | (I + V^\dagger(t))(I + V(t)) | \psi_0 \rangle \\ &= 2 + \underbrace{\langle \psi_0 | V^\dagger(t) | \psi_0 \rangle + \langle \psi_0 | V(t) | \psi_0 \rangle}_{(\langle \psi_0 | V(t) | \psi_0 \rangle)^*} \\ &= 2 + 2\text{Re}(\langle \psi_0 | V(t) | \psi_0 \rangle) \\ &= 2 + 2\text{Re}(T_{kl}) \end{aligned}$$

and

$$\begin{aligned}\langle\beta|\beta\rangle &= \langle\psi_0|(I - V^\dagger(t))(I - V(t))|\psi_0\rangle \\ &= 2 - 2\text{Re}(T_{kl})\end{aligned}$$

it follows that

$$\langle Z \rangle = \text{Re}(T_{kl})$$

whereas

$$\begin{aligned}\langle Y \rangle &= -i\langle\psi|1\rangle\langle 0|\psi\rangle + i\langle\psi|0\rangle\langle 1|\psi\rangle \\ &= -i\frac{1}{4}(\langle\beta|\alpha\rangle - \langle\alpha|\beta\rangle) \\ &= -\frac{1}{2}\text{Im}(\langle\alpha|\beta\rangle)\end{aligned}$$

From

$$\begin{aligned}\langle\alpha|\beta\rangle &= \langle\psi_0|(I + V^\dagger(t))(I - V(t))|\psi_0\rangle \\ &= \langle\psi_0|V^\dagger(t)|\psi_0\rangle - \langle\psi_0|V(t)|\psi_0\rangle \\ &= -2i\text{Im}(T_{kl})\end{aligned}$$

we get that $\langle Y \rangle = \text{Im}(T_{kl})$, from which the result follows.

Proof of the correlation entropy-minimization property of natural orbitals

Let's introduce the so-called *correlation entropy*, defined for any matrix M with non-negative diagonal entries as

$$S_{\text{corr}}(M) \equiv - \sum_j M_{jj} \log M_{jj} \quad (\text{J.1})$$

From definition 5.9, such a quantity is well-defined for $D^{(c)}$ since diagonal elements are occupation numbers associated to the single-particle orbitals defined by the set of creation/annihilation operators $\{c_i^\dagger, c_i\}_i$. It provides a measure of the spread of the distribution onto the different orbitals of the $\text{Tr}(D^{(c)}) \equiv n$ particles $|\psi\rangle$ describes the state of.

We aim at showing that the transformation to NO yields a minimal correlation entropy 1-RDM (and thus, a maximally localized occupation numbers distribution in a sense that will be made clearer later). Let us denote as U the transformation to NO among all the unitary transformations $V \in U_N$, the result to be proven reads

$$U = \arg \min_{V \in U_N} (S_{\text{corr}}(V^\dagger D^{(c)} V)) \quad (\text{J.2})$$

or, in other words,

$$S_{\text{corr}}(D^{(c)}) \geq S_{\text{corr}}(n) \quad (\text{J.3})$$

with n the diagonal matrix $D^{(c)}$ is similar to, as defined in 5.11.

In what follows, we will summon well-known quantities in quantum information theory which are defined for density matrices and apply them to hermitian, positive matrices whose trace is however not unity. This does not change the applicability of the definitions, but we take the liberty not to write down rescaling factors such as $\frac{1}{\text{Tr}(D^{(c)})}$ to be able to apply these definitions. The derivation below is inspired from

[115].

Since n is diagonal we have that

$$S_{\text{corr}}(n) = -\text{Tr}(n \log n) \equiv S(n) \quad (\text{J.4})$$

where S denotes the von-Neumann entropy. Since the von-Neumann entropy is invariant under unitary transformation, we also have

$$S(n) = S(D^{(c)}). \quad (\text{J.5})$$

Conversely,

$$S_{\text{corr}}(D^{(c)}) = S(D_{\text{diag}}^{(c)}) \quad (\text{J.6})$$

with $D_{\text{diag}}^{(c)}$ referring to the diagonal matrix obtained from $D^{(c)}$ by setting its off-diagonal elements to 0.

Let's introduce the quantum relative entropy between density matrices $D^{(c)}$ and δ^1

$$S(D^{(c)}||\delta) \equiv \text{Tr}(D^{(c)} \log D^{(c)}) - \text{Tr}(D^{(c)} \log \delta), \quad (\text{J.7})$$

Let M be a square matrix and Δ a diagonal, similar-shape matrix. Then, we can easily show that if $M_{ii} = 0 \forall i$, then $\text{Tr}(M\Delta) = 0$:

$$\begin{aligned} \text{Tr}(M\Delta) &= \sum_{i,k} M_{ik} \Delta_{ki} \\ &= \sum_i \left(\underbrace{M_{ii}}_{=0} \Delta_{ii} + \sum_{k \neq i} M_{ik} \underbrace{\Delta_{ki}}_{=0} \right) \\ &= 0 \end{aligned}$$

which we can equivalently state as

$$\text{Tr}(M\Delta) = \text{Tr}(M_{\text{diag}}\Delta) \quad (\text{J.8})$$

We thus have that for δ a diagonal matrix with non-negative entries (corresponding to the density matrix of an incoherent state $\delta = \sum_i p_i |i\rangle \langle i|$), since $\log \delta$ is also a diagonal matrix, $\text{Tr}(D^{(c)} \log \delta) = \text{Tr}(D_{\text{diag}}^{(c)} \log \delta)$ which allows to rewrite the second term of the relative entropy introduced in J.7. Combined with the definition of $S(D_{\text{diag}}^{(c)}||\delta)$, we have at this point

$$\begin{aligned} S(D^{(c)}||\delta) &= \text{Tr}(D^{(c)} \log D^{(c)}) - \text{Tr}(D_{\text{diag}}^{(c)} \log \delta) \\ &= -S(D^{(c)}) + S(D_{\text{diag}}^{(c)}||\delta) + S(D_{\text{diag}}^{(c)}). \end{aligned}$$

¹This function has values in $\mathbb{R}^+ \cup \{+\infty\}$. Its non-negativity is rederived further in this Appendix.

Applying this relation with $\delta = D_{\text{diag}}^{(c)}$, the second term vanishes and we are left with

$$\begin{aligned} S(D^{(c)}||D_{\text{diag}}^{(c)}) &= -S(D^{(c)}) + S(D_{\text{diag}}^{(c)}) \\ &= S_{\text{corr}}(D^{(c)}) - S_{\text{corr}}(n) \end{aligned}$$

The non-negativity of the quantum relative entropy yields the result:

$$S_{\text{corr}}(D^{(c)}) - S_{\text{corr}}(n) = S(D^{(c)}||D_{\text{diag}}^{(c)}) \geq 0 \quad (\text{J.9})$$

Finally, let's prove this latter property, namely $S(\rho||\sigma) \geq 0$ whichever density matrices ρ and σ .

From the spectral theorem, $\rho = U\Delta^{(\rho)}U^\dagger$ and $\sigma = V\Delta^{(\sigma)}V^\dagger$ with $UU^\dagger = VV^\dagger = I$, so that

$$\begin{aligned} S(\rho||\sigma) &= \text{Tr}(\rho \log \rho) - \text{Tr}(\rho \log \sigma) \\ &= \sum_i \Delta_{ii}^{(\rho)} \log \Delta_{ii}^{(\rho)} - \text{Tr}(\rho \log \sigma) \\ &= \sum_i \Delta_{ii}^{(\rho)} \log \Delta_{ii}^{(\rho)} - \text{Tr}(U\Delta^{(\rho)}U^\dagger \log(V\Delta^{(\sigma)}V^\dagger)) \end{aligned} \quad (\text{J.10})$$

Using $\log(A = P\Delta P^{-1}) = P \log \Delta P^{-1}$ as well as the cyclicity of the trace, the second term can be expressed as

$$\begin{aligned} \text{Tr}(U\Delta^{(\rho)}U^\dagger \log(V\Delta^{(\sigma)}V^\dagger)) &= \text{Tr}(U\Delta^{(\rho)}U^\dagger V(\log \Delta^{(\sigma)})V^\dagger) \\ &= \text{Tr}(V^\dagger U\Delta^{(\rho)}U^\dagger V(\log \Delta^{(\sigma)})) \\ &= \text{Tr}(W\Delta^{(\rho)}W^\dagger(\log \Delta^{(\sigma)})) \end{aligned}$$

with $W \equiv V^\dagger U$. Since $\log \Delta^{(\sigma)}$ is diagonal, applying J.8 we further have

$$\begin{aligned} \text{Tr}(U\Delta^{(\rho)}U^\dagger \log(V\Delta^{(\sigma)}V^\dagger)) &= \text{Tr}\left(\left(W\Delta^{(\rho)}W^\dagger\right)_{\text{diag}}(\log \Delta^{(\sigma)})\right) \\ &= \sum_{i,j} |W_{ij}|^2 \Delta_{jj}^{(\rho)} \log \Delta_{ii}^{(\sigma)} \end{aligned}$$

Injecting in J.10, we get

$$S(\rho||\sigma) = \sum_i \left(\Delta_{ii}^{(\rho)} \left(\log \Delta_{ii}^{(\rho)} - \sum_j |W_{ji}|^2 \log \Delta_{jj}^{(\sigma)} \right) \right) \quad (\text{J.11})$$

Since $WW^\dagger = I$ we have $\sum_j |W_{ji}|^2 = 1 \forall i$ and convexity inequalities on convex function $-\log$ yield

$$S(\rho||\sigma) \geq \sum_i \left(\Delta_{ii}^{(\rho)} \left(\log \Delta_{ii}^{(\rho)} - \log \left(\sum_j |W_{ji}|^2 \Delta_{jj}^{(\sigma)} \right) \right) \right) \quad (\text{J.12})$$

Since $\Delta_{ii}^{(\rho)}$ and $\sum_j |W_{ji}|^2 \Delta_{jj}^{(\sigma)}$ are probability distributions ($\sum_i \left(\sum_j |W_{ji}|^2 \Delta_{jj}^{(\sigma)} \right) = \sum_j \left(\sum_i |W_{ji}|^2 \right) \Delta_{jj}^{(\sigma)} = \sum_j \Delta_{jj}^{(\sigma)} = 1$), the non-negativity of the classical relative entropy brings the result.

Appendix **K**

Specifics of the two-impurity slave-boson scheme

In this work, we considered the 2D Hubbard model with a square lattice of lattice constant $a = 1$ and applied the RISB scheme with $N_c = 2$ -site cells. We define the superlattice as

$$\mathbf{R} = 2m \underbrace{\begin{pmatrix} 1 \\ 0 \end{pmatrix}}_{\mathbf{u}_0} + n \underbrace{\begin{pmatrix} 0 \\ 1 \end{pmatrix}}_{\mathbf{u}_1}, (m, n) \in \mathbb{Z}^2 \quad (\text{K.1})$$

as represented on Figure K.1.

Energy dispersion The energy dispersion relation referred to in Equations 3.24a and 3.24b is, considering a given spin sector, a 2×2 matrix whose terms are obtained from the energy in real space of the superlattice as

$$[\varepsilon_{\mathbf{k}}]_{pq} = \sum_{\mathbf{R} \in \text{SL}} e^{-i\mathbf{k} \cdot \mathbf{R}} [\varepsilon_{\mathbf{R}}]_{pq} \quad (\text{K.2})$$

where $p \in \{0, 1\}$ denotes which site within the considered supercell is considered and $q \in \{0, 1\}$, which site within the other supercell - the same supercell or a neighbouring supercell due to the fact that there is only nearest-neighbour hopping in the Hubbard model. Vector \mathbf{k} denotes a vector of the first Brillouin zone of the superlattice. As seen on Figure K.1, site 0 is taken as the origin so that

$$\begin{aligned} [\varepsilon_{\mathbf{k}}]_{00} &= t (e^{-i\mathbf{k} \cdot \mathbf{u}_1} + e^{-i\mathbf{k} \cdot (-\mathbf{u}_1)}) \\ &= t (e^{-ik_y a} + e^{ik_y a}) \\ &= 2t \cos(k_y a) \end{aligned}$$

and similarly $[\varepsilon_{\mathbf{k}}]_{00} = 2t \cos(k_y a) = [\varepsilon_{\mathbf{k}}]_{00}$. For non diagonal elements one has

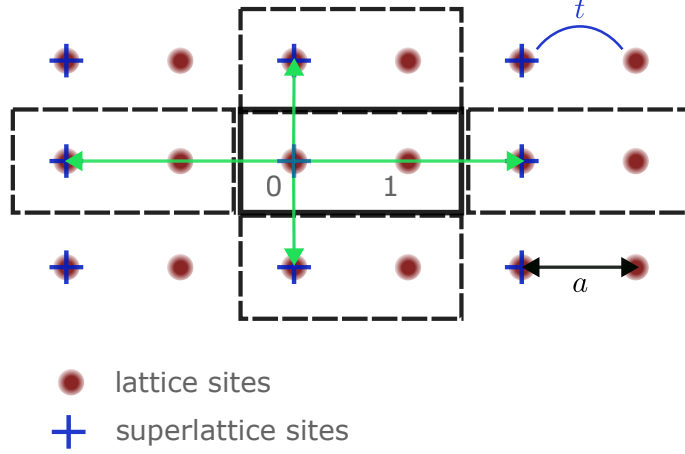


Figure K.1: Lattice (2D square Hubbard model with lattice spacing $a = 1$, nearest-neighbour hopping $t = 0.25$) and $N_c = 2$ superlattice considered in this work. The green arrows materialize the positions of the supercells interacting with the central supercell.

$$\begin{aligned} [\varepsilon_{\mathbf{k}}]_{01} &= t (e^{-i\mathbf{k}\cdot\mathbf{0}} + e^{-i\mathbf{k}\cdot(-2\mathbf{u}_0)}) \\ &= t (1 + e^{2ik_x a}) \end{aligned}$$

and can readily show that $[\varepsilon_{\mathbf{k}}]_{10} = ([\varepsilon_{\mathbf{k}}]_{01})^*$.

Symmetry considerations In each spin sector, we considered matrices transformed into the basis adapted to the dimer symmetry in order to reduce the number of free parameters. The general procedure to this end is explicated in Reference [116] and relies on the irreducible representation of finite groups, but here we can explain it in simpler terms. Since the two sites 0 and 1 of the supercell are equivalent (as opposed for instance to a bipartite lattice where the two sites could correspond to different atoms), matrices $R, \lambda, \epsilon_{\mathbf{k}}$ are of the form

$$M = \begin{pmatrix} a & b \\ b^* & a \end{pmatrix}$$

then with

$$P = \frac{1}{\sqrt{2}} \begin{pmatrix} 1 & 1 \\ 1 & -1 \end{pmatrix} \quad (\text{K.3})$$

we have that

$$PMP^{-1} = \begin{pmatrix} a + \frac{b+b^*}{2} & \frac{b^*-b}{2} \\ \frac{b-b^*}{2} & a - \frac{b+b^*}{2} \end{pmatrix} \quad (\text{K.4})$$

which for real matrices R and λ is diagonal. We will note $R^+ = R_{00} + R_{01}$ and $R^- = R_{00} - R_{01}$ and use similar definitions for λ^+ and λ^- .

Appendix **L**

Nature of the qubit pool operators in NOA-VQE

We recall that ADAPT-VQE [98] stems from the trotterized UCCSD ansatz, which applies single and double excitations over a reference state. Here we have made the choice to use $XX + YY$, XY and ZZ two-qubit operators as well as all of the single-qubit rotations. We explain the form retained for the two-qubit excitations.

Single excitations correspond to hopping terms of the form $c_k^\dagger c_l$ which map, within Jordan-Wigner encoding, onto chains comprising $X_k X_l$, $Y_k Y_l$ as well as $X_k Y_l$ and $Y_k X_l$ terms:

$$c_k^\dagger c_l \xrightarrow{\text{JW}} \frac{1}{2} (X_k - iY_k) \frac{1}{2} (X_l + iY_l) = \frac{1}{4} (X_k X_l + Y_k Y_l + i(X_k Y_l - Y_k X_l))$$

First, let's underline that the operators XX and YY commute. To see it, reintroducing the tensor products \otimes as well as usual matrix product denoted here $.$ in the notation we have:

$$\begin{aligned} [X \otimes X, Y \otimes Y] &= (X \otimes X) . (Y \otimes Y) - (Y \otimes Y) . (X \otimes X) \\ &= (X.Y) \otimes (X.Y) - (Y.X) \otimes (Y.X) \\ &= iZ \otimes iZ - (-iZ) \otimes (-iZ) \\ &= 0. \end{aligned}$$

We thus have

$$\begin{aligned} e^{-i\theta/2(XX+YY)} &= e^{-i\theta/2XX} e^{-i\theta/2YY} \\ &= (\cos \theta/2I - i \sin \theta/2XX) (\cos \theta/2I - i \sin \theta/2YY) \\ &= \cos^2 \theta/2I - i \sin \theta/2 \cos \theta/2 (XX + YY) - \sin^2 \theta/2 XX.YY \\ &= \cos^2 \theta/2I - i \sin \theta/2 \cos \theta/2 (XX + YY) - \sin^2 \theta/2 X.Y \otimes X.Y \\ &= \cos^2 \theta/2I - i \sin \theta/2 \cos \theta/2 (XX + YY) + \sin^2 \theta/2 ZZ \end{aligned}$$

and since $XX = \begin{pmatrix} 0 & 0 & 0 & 1 \\ 0 & 0 & 1 & 0 \\ 0 & 1 & 0 & 0 \\ 1 & 0 & 0 & 0 \end{pmatrix}$, $YY = \begin{pmatrix} 0 & 0 & 0 & -1 \\ 0 & 0 & 1 & 0 \\ 0 & 1 & 0 & 0 \\ -1 & 0 & 0 & 0 \end{pmatrix}$ and $ZZ = \begin{pmatrix} 1 & 0 & 0 & 0 \\ 0 & -1 & 0 & 0 \\ 0 & 0 & -1 & 0 \\ 0 & 0 & 0 & 1 \end{pmatrix}$

we can write

$$\begin{aligned}
e^{-i\theta/2(XX+YY)} &= \begin{pmatrix} \cos^2 \theta/2 + \sin^2 \theta/2 & 0 & 0 & 0 \\ 0 & \cos^2 \theta/2 - \sin^2 \theta/2 & -2i \sin \theta/2 \cos \theta/2 & 0 \\ 0 & -2i \sin \theta/2 \cos \theta/2 & \cos^2 \theta/2 - \sin^2 \theta/2 & 0 \\ 0 & 0 & 0 & \cos^2 \theta/2 + \sin^2 \theta/2 \end{pmatrix} \\
&= \begin{pmatrix} 1 & 0 & 0 & 0 \\ 0 & \cos \theta & -i \sin \theta & 0 \\ 0 & -i \sin \theta & \cos \theta & 0 \\ 0 & 0 & 0 & 1 \end{pmatrix} \tag{L.1}
\end{aligned}$$

which is a particle-number preserving gate.

On the other hand, we retain XY to change the number of particles in the state. Indeed,

$$e^{-i\theta XY} = \begin{pmatrix} \cos \theta & 0 & 0 & -\sin \theta \\ 0 & \cos \theta & \sin \theta & 0 \\ 0 & -\sin \theta & \cos \theta & 0 \\ \sin \theta & 0 & 0 & \cos \theta \end{pmatrix} \tag{L.2}$$

Finally, the ZZ excitations mirror density-density interactions at work in correlated states:

$$c_k^\dagger c_k c_l^\dagger c_l \xrightarrow{\text{JW}} \left(\frac{1 - Z_k}{2} \right) \left(\frac{1 - Z_l}{2} \right) \tag{L.3}$$

Appendix M

Keldysh contour formalism

Suppose $t \geq t_0 \in \mathbb{R}^+$. We want to show that

$$\mathcal{O}(t) = \text{Tr} (U(t_0, t)O(t)U(t, t_0)\rho_0) \quad (\text{M.1})$$

can be written compactly by means of so-called *contour integration* over the *Keldysh contour* \mathcal{C} :

$$\mathcal{O}(t) = \left\langle \mathcal{T}_{\mathcal{C}} \left(\exp \left(-i \int_{\mathcal{C}} \mathcal{H}(s) ds \right) O(t) \right) \right\rangle \quad (\text{M.2})$$

with $\langle \bullet \rangle \equiv \text{Tr}(\rho_0 \bullet)$. We follow the derivation of [108]. Additionally we refer the reader to the thesis referenced as [117] for more details.

We can interpret the right-hand side of formula M.1 as starting from the reference state ρ_0 , evolving up to time t , picking the operator $O(t)$ ¹, going back to time t_0 and computing the overlap between the state reached doing so and the initial state ρ_0 . This can be pictured with a path along a contour. The path consists of a forward branch \mathcal{C}_- from t_0 to t (represented on the upper plane for clarity) and a backward branch \mathcal{C}_+ from t to t_0 (displaced to the lower plane), as depicted on Figure 6.2 in the main text.

Let's consider a parameter s that describes points along the whole contour $\mathcal{C} = \mathcal{C}^- \cup \mathcal{C}^+$. We can define (fermionic) operators of this variable: $A(s) = A_-(s)$ if $s \in \mathcal{C}^-$, $A(s) = A_+(s)$ if $s \in \mathcal{C}^+$ with A_- that may be a different operator than A_+ (that won't be the case for us). For $t \in \mathbb{R}$, according to the setting where t intervenes (which evolution), we may consider we have to deal either with $s = t_-$ (being on the upper branch) or $s = t_+$ (being on the lower branch). Contour variables are ordered according to how early they appear along the contour: if s_1 comes up before s_2 , we'll say that s_1 is *earlier* than s_2 and note $s_1 \leq_{\mathcal{C}} s_2$. Whenever we will not use the \mathcal{C} lowerscript, we will refer to the ordering of real numbers rather than this contour ordering.

¹As explicited in the main text, this is indeed O in Schrödinger representation; not in Heisenberg's. The time label is there to indicate where to place O in the contour-ordered expression.

We can introduce a contour integral according to the following rules:

- $\int_{s_1}^{s_2} A(s)ds = \int_{s_1}^{s_2} A_-(s)ds$ for $s_1 < s_2$, $s_1, s_2 \in \mathcal{C}^-$
- $\int_{s_1}^{s_2} A(s)ds = \int_{s_1}^{s_2} A_+(s)ds$ for $s_1 > s_2$, $s_1, s_2 \in \mathcal{C}^+$
- $\int_{s_1}^{s_2} A(s)ds = \int_{s_1}^{s'} A_-(s)ds + \int_{s'}^{s_2} A_+(s)ds$ for $s_1 \in \mathcal{C}^-$, $s_2 \in \mathcal{C}^+$

and $\int_{s_1}^{s_2} A(s)ds = -\int_{s_2}^{s_1} A(s)ds$ for $s_1 \geq_{\mathcal{C}} s_2$.

Let's write $\int_{\mathcal{C}^-} \equiv \int_{t_0^-}^{t^-}$ and $\int_{\mathcal{C}^+} \equiv \int_{t^+}^{t_0^+}$. We define integration over the Keldysh contour as

$$\int_{\mathcal{C}} \equiv \int_{t_0^-}^{t^-} + \int_{t^+}^{t_0^+}. \quad (\text{M.3})$$

Let's go back to our observable's expectation value:

$$\begin{aligned} \mathcal{O}(t) &= \left\langle \bar{\mathcal{T}} \exp \left(-i \int_t^{t_0} \mathcal{H}(u)du \right) O(t) \mathcal{T} \exp \left(-i \int_{t_0}^t \mathcal{H}(u)du \right) \right\rangle \\ &= \left\langle \bar{\mathcal{T}} \exp \left(-i \int_{\mathcal{C}^+} \mathcal{H}(s)ds \right) O(t) \mathcal{T} \exp \left(-i \int_{\mathcal{C}^-} \mathcal{H}(s)ds \right) \right\rangle \\ &= \left\langle \mathcal{T}_{\mathcal{C}} \exp \left(-i \int_{\mathcal{C}^+} \mathcal{H}(s)ds \right) O(t) \mathcal{T}_{\mathcal{C}} \exp \left(-i \int_{\mathcal{C}^-} \mathcal{H}(s)ds \right) \right\rangle \end{aligned}$$

where we have introduced the contour-ordering operator $\mathcal{T}_{\mathcal{C}}$, that acts as \mathcal{T} on the upper branch \mathcal{C}^- , and as $\bar{\mathcal{T}}$ on the lower branch \mathcal{C}^+ . For mixed variables we have of course that if $s_1 \in \mathcal{C}^-$, $s_2 \in \mathcal{C}^+$, $\mathcal{T}_{\mathcal{C}} A(s_1)A(s_2) = -A(s_2)A(s_1)$, whereas $\mathcal{T}_{\mathcal{C}}$ has no effect on such an expression if $s_1 \in \mathcal{C}^+$, $s_2 \in \mathcal{C}^-$.

Now that we have a single type of ordering operator in the expression, we can gather the terms, use the commutation inside the ordered expression and gather the integrals (licit thanks to the presence of the contour ordering operator) to get the final expression:

$$\begin{aligned} \mathcal{O}(t) &= \left\langle \mathcal{T}_{\mathcal{C}} \left(\exp \left(-i \int_{\mathcal{C}^+} \mathcal{H}(s)ds \right) O(t) \exp \left(-i \int_{\mathcal{C}^-} \mathcal{H}(s)ds \right) \right) \right\rangle \\ &= \left\langle \mathcal{T}_{\mathcal{C}} \left(\exp \left(-i \int_{\mathcal{C}^+} \mathcal{H}(s)ds \right) \exp \left(-i \int_{\mathcal{C}^-} \mathcal{H}(s)ds \right) O(t) \right) \right\rangle \\ &= \left\langle \mathcal{T}_{\mathcal{C}} \left(\exp \left(-i \int_{\mathcal{C}} \mathcal{H}(s)ds \right) O(t) \right) \right\rangle \end{aligned}$$

Note that to get rid of the dependence of the form (length) of the contour on the time t , we can extend it to infinity (one gets the proper *Keldysh contour*), this does not change the expressions.

List of Figures

2.1	Characterization of the quasiparticle weight Z across the Fermi surface in presence of interactions within Fermi liquid theory. The discontinuity in ground state momentum density at the Fermi momentum k_F is reduced from 1 to Z as interactions are turned on.	6
2.2	Representation of the Hubbard model. Only onsite repulsion and nearest-neighbour hopping are taken into account, with respective strengths U and $-t$. The scheme represents a 2D square lattice. Figure adapted from [9].	8
2.3	Phase diagram of the Hubbard model at finite temperature, for intermediate interaction strength U/t . Figure taken from [11].	9
3.1	Typical density of states of the DMFT solution of the Hubbard model at zero temperature and half-filling. One can observe the free-electron DOS at $U = 0$ which is semi-circular and centered around the Fermi level E_F , whereas as U is increased, the so-called <i>quasiparticle peak</i> near the Fermi level shrinks in favour of <i>Hubbard bands</i> which are a signature of interactions. For large values of U only the Hubbard bands remain: the system is a Mott insulator. Illustration taken from [12].	12
3.2	Depiction of the Dynamical Mean Field Theory viewpoint. Within DMFT, a lattice site is singled-out and regarded as an atom exchanging electrons with the remainder regarded as a bath, parametrized by the Weiss field \mathcal{G}_0 . The valence transition of the atomic sites are studied through the proxy impurity model, hence the <i>dynamical</i> character of the theory. Inset adapted from [12].	16
3.3	The DMFT iterative scheme. Image adapted from [19].	19
3.4	Two directions along which DMFT results can be improved. The first direction is investigated in chapter 5; the second one, in chapter 6. . .	21
3.5	The different models – original lattice, effective and embedded – considered within RISB. Image taken from [30].	22
4.1	Symbol of the CNOT gate. The top qubit is the control qubit, whereas the bottom one is the target qubit.	32
4.2	Conversion of measurements in X or Y bases into measurements in the Z basis.	33

4.3	Circuit \mathcal{C}_{kl} enabling the calculation of Green's functions elements $T_{kl} = \langle \psi_0 e^{iHt} \sigma^k e^{-iHt} \sigma^l \psi_0 \rangle$	35
4.4	Principle of the Variational Quantum Eigensolver (VQE) algorithm. An approximation to the ground state is prepared by optimizing a variational circuit.	37
4.5	Flowchart of the Variational Quantum Eigensolver (VQE) algorithm, a quantum-classical hybrid algorithm.	38
4.6	Study of the influence of each noise source on the distance of the probability vector $\mathbf{p}_{\text{noisy}} = (\rho_{11}, \rho_{22}, \rho_{33}, \rho_{44})$ to its statevector, noise-free simulation counterpart. Average over 10 runs corresponding to different random parametrizations of the circuit. The error corresponds to the standard deviation.	46
4.7	Principle of zero-noise extrapolation illustrated with a linear ansatz for inference. Occurrences of two-qubit gates G are followed by a number r of resolutions of the identity $I = GG^\dagger$ to scale the noise to a factor $(2r + 1)$. A noiseless observable value can be inferred from the noisy observables measured on the original circuit and the circuit with $r = 1$ by linearly extrapolating to $r = -1/2$. Image published in Reference [46].	48
5.1	Orbital occupancies in the original basis (symmetry-adapted) and in the Natural-Orbital basis for $N_c = 2$ typical embedded models at different levels of Coulomb interaction U	53
5.2	Effect of stacking fSim layers on the natural orbital occupancies.	56
5.3	Attained orbital occupancies for ten different random parametrizations of a fSim circuit, with different numbers of fSim cycles. Dashed lines: occupancies in site-spin basis, solid lines: corresponding NOONs. The layered structure of the circuits is explicated on Figure 5.2a.	56
5.4	Quantum routine allowing to rotate into the bonding/antibonding basis.	58
5.5	Multireference (MR) ansatz for $N_c = 1$ in natural orbitals.	58
5.6	Circuits investigated for the ground state preparation of $N_c = 2$ embedded models. (a) Multi-Reference Excitation Preserving (MREP) circuit. (b) Eight-qubit, one-cycle Low-Depth Circuit Ansatz (LDCA) circuit.	60
5.7	Comparison between runs in the original, site-spin basis (dashed lines) and in the NO basis (solid lines), with and without noise, for two-impurity converged embedded Hamiltonians, at different levels of Coulombic interaction U . The ansätze considered are the one-cycle compressed LDCA circuit and the MREP ansatz, whose structures are explicated in Figure 5.6. Each VQE optimization is repeated three times, with different random initializations so as to highlight sensitivity to the initialization. The VQE optimization is carrying out allowing for up to 10000 steps of the BFGS algorithm.	62

5.8	Illustration of the capability of the transformation to natural orbitals, \mathcal{U} , to enhance the expressibility of a variational ansatz manifold \mathcal{V} . The different shades of blue represent different degrees of complexity corresponding to different parametrizations of the circuit, from product states in light blue to the most entangled states of the manifold in deep blue.	63
5.9	Different strategies to modify the scope of a variational ansatz $U(\boldsymbol{\theta})$ through a single-particle orbitals rotation whose effect on the states is represented with the unitary \mathcal{U} . The strategies differ in the associated overheads: strategy 5.9a, in which \mathcal{U} is implemented with quantum gates, comes with a gate overhead whereas strategy 5.9b, where the effect of \mathcal{U} is included in the measurement process, incurs a measurement overhead as typically \mathcal{U} does not preserve the sparsity of \mathcal{H}	64
5.10	Principle of the Natural-Orbitalization algorithm, as well as the Natural-Orbitalizing Adaptive VQE (NOA-VQE) scheme.	65
5.11	Converged VQE energies along the Natural-Orbitalization procedure for two-impurity converged embedded Hamiltonians, at different levels of Coulombic interaction U , within the MREP ansatz. For each case the NO energy reference corresponds to the best run of Figure 5.7.	69
5.12	Circuits investigated within the Natural-Orbitalization algorithm. (a) Product circuit. (b) fSim circuit. (c) Four-qubit, one-cycle Low-Depth Circuit Ansatz (LDCA) circuit.	70
5.13	VQE traces within the Natural-Orbitalization algorithm applied to the ground state preparation of the Hubbard dimer, with (bottom) and without (top) depolarizing noise.	71
5.14	Same as 5.13, but for the Hubbard plaquette.	72
5.15	Converged VQE energies along the Natural-Orbitalization procedure for the Hubbard dimer (top) and the Hubbard plaquette (bottom), with (dashed lines) and without (solid lines) depolarizing noise. These plots present the final energies attained in the plots of Figure 5.13 and 5.14.	73
5.16	Evolution of spin-orbitals along the NOization procedure for the Hubbard dimer at $U = 1$	74
5.17	Cost function along the RISB loop for $N_c = 2$ at $U = 1$ within either MREP-ansatz based variational ground state preparation (labelled as 'exact NO basis'), or MREP-ansatz based Natural-Orbitalizing ground state preparation (labelled as 'approximate NO basis').	76
5.18	Hybrid NOized RISB scheme. The upper panel describes the RISB embedding scheme. The solving of the impurity model, which incorporates computations over a QPU in our hybrid implementation, is described by the two lower panels. It consists in a VQE scheme topped with single-particle orbital updates.	77

5.19	Evolution of the quasiparticle weight Z as a function of the Coulombic interaction U within a slave-boson loop for one impurity. Mitigated results correspond to zero-noise extrapolated results within a linear extrapolation scheme.	78
5.20	Convergence of the slave-boson scheme for different values of U with $N_c = 2$	79
5.21	NOA VQE for Hubbard plaquette at $U = 0$ (top) and $U = 1$ (bottom), with (right, dashed lines) and without (left, solid lines) depolarizing noise.	81
6.1	Fit of the spectral function $A(\omega) = -\frac{1}{\pi}\text{Im}\Delta^R(\omega)$ within a non-dissipative (left) or a dissipative (right) scheme for the impurity model's bath. We propose to leverage the widening brought about by qubit dissipation.	84
6.2	Keldysh contour. The superscript indices $+$ and $-$ are branch indices, indicating which branch, the forward-propagating branch \mathcal{C}^- or the backward-propagating branch \mathcal{C}^+ one must consider the time belongs to. The dashed lines materialize the fact that the contour may be extended to infinity so that it does not depend on t	85
6.3	Visualization over the Keldysh contour of the calculation of $G_{-+}(t_2, t_1)$ for $t_2 > t_1$	86
6.4	Illustration of the nesting property of hybridizations. On the left, the impurity is hybridized with coupling matrix V with a free fermion bath. On the right, it is coupled to a dissipative bath, whose dissipation is tuned by a reservoir-coupling parameter Λ . The resulting hybridization characterizing the effect of the dissipative bath onto the impurity picks an additional self-energy term. We resort to a Lindbladian linear dissipation to a reservoir in order to get a self-energy which provides an widening of the peaks for the fit of the DMFT hybridization.	89
6.5	Two types of quadratic 'bath' systems. Upper panel: system connected to a non-dissipative reservoir. Lower panel: system connected to a dissipative reservoir. The reduced dynamics is rendered by Lindblad's equation with jump operators $\sqrt{\Lambda^{(1)}}c_p, \sqrt{\Lambda^{(2)}}c_p^\dagger$. The unitary part of the reduced dynamics is given by \tilde{h} , which includes Lamb shifts terms additionally to h	90
6.6	Structure of the considered system, comprising an impurity site connected to dissipative bath sites. Each bath site is connected linearly to a Markovian reservoir.	93
6.7	Chosen geometry of the bath. The bath sites come in two sets, each displaying a single of the two dissipative processes. Half of the sites are used to fit the lesser part $<$, and half are used to fit the greater part $>$ of the DMFT hybridization. The damped bath sites (on the right) are initialized to being all empty, which corresponds to their steady-state in the absence of coupling to the impurity. For the same reason, the excited bath sites (on the left) are initialized to being all occupied.	98

6.8	Cartoon representation of the fit of the DMFT hybridization. The DMFT bath spectral function decomposes as $-\frac{1}{\pi}\text{Im}\Delta^R(\omega) = \frac{i}{2\pi}\Delta^<(\omega) - \frac{i}{2\pi}\Delta^>(\omega)$. The lesser part and the greater part are fitted separately, with different sets of dissipative bath sites. On this picture, it is implied that the DMFT hybridization is that of an equilibrium system, so that the fluctuation-dissipation theorem holds.	99
6.9	Cost functions associated with optimal fit as a function of the number of bath sites n_b and the intensity of dissipation Λ , for different temperatures (left). Optimization done with COBYLA minimizer, fixed grid of energies. The scale of the y axis is logarithmic. On the right, the fits corresponding to the white squares on the left are displayed. The dashed lines materialize the energies of the bath levels.	102
6.10	Evolution of real part of diagonal density matrix elements with t , for a 2 bath-site system with fermionic dissipation (in blue) and qubit dissipation (in orange), $\Lambda = 0.1$, starting from the same state. The dotted green line represents the dynamics with qubit dissipation, rescaled as $\Lambda' = \frac{\Lambda}{\sqrt{2}}$	104
E.1	Spectral function and self-energy elements associated with the model	
E.1.	121
K.1	Lattice (2D square Hubbard model with lattice spacing $a = 1$, nearest-neighbour hopping $t = 0.25$) and $N_c = 2$ superlattice considered in this work. The green arrows materialize the positions of the supercells interacting with the central supercell.	134

List of Tables

4.1	Two leading ansatz design strategies for VQE circuits.	39
4.2	Description of quantum systems. The master equation for open systems referred to here, Lindblad's equation, relies on several assumptions.	45
4.3	Specifications of IBM Melbourne as of March 2020, and noise rescaling details. r stands for the noise rescaling factor.	46
5.1	Characteristics of the four-qubit circuits used within the Natural-Orbitalization algorithm.	70
5.2	Characteristics of the eight-qubit circuits used within the Natural-Orbitalization algorithm.	70
5.3	Number of Pauli terms in Jordan-Wigner representation of Hubbard Hamiltonians, for $U = 0$ (value on the left) and $U = 1$ (value on the right).	75

Bibliography

- [1] F. Arute, K. Arya, R. Babbush, D. Bacon, J. C. Bardin, R. Barends, R. Biswas, S. Boixo, F. G. S. L. Brandao, D. A. Buell, B. Burkett, Y. Chen, Z. Chen, B. Chiaro, R. Collins, W. Courtney, A. Dunsworth, E. Farhi, B. Foxen, A. Fowler, C. Gidney, M. Giustina, R. Graff, K. Guerin, S. Habegger, M. P. Harrigan, M. J. Hartmann, A. Ho, M. Hoffmann, T. Huang, T. S. Humble, S. V. Isakov, E. Jeffrey, Z. Jiang, D. Kafri, K. Kechedzhi, J. Kelly, P. V. Klimov, S. Knysh, A. Korotkov, F. Kostritsa, D. Landhuis, M. Lindmark, E. Lucero, D. Lyakh, S. Mandrà, J. R. McClean, M. McEwen, A. Megrant, X. Mi, K. Michielsen, M. Mohseni, J. Mutus, O. Naaman, M. Neeley, C. Neill, M. Y. Niu, E. Ostby, A. Petukhov, J. C. Platt, C. Quintana, E. G. Rieffel, P. Roushan, N. C. Rubin, D. Sank, K. J. Satzinger, V. Smelyanskiy, K. J. Sung, M. D. Trevithick, A. Vainsencher, B. Villalonga, T. White, Z. J. Yao, P. Yeh, A. Zalcman, H. Neven, J. M. Martinis, Quantum supremacy using a programmable superconducting processor, *Nature* 574 (7779) (2019) 505–510, number: 7779 Publisher: Nature Publishing Group. doi:10.1038/s41586-019-1666-5.
URL <https://www.nature.com/articles/s41586-019-1666-5>
- [2] U. Wolff, Collective monte carlo updating for spin systems, *Physical Review Letters* 62 (4) (1989) 361–364. doi:10.1103/physrevlett.62.361.
- [3] P. A. M. Dirac, R. H. Fowler, Quantum mechanics of many-electron systems, *Proceedings of the Royal Society of London. Series A, Containing Papers of a Mathematical and Physical Character* 123 (792) (1929) 714–733. arXiv:<https://royalsocietypublishing.org/doi/pdf/10.1098/rspa.1929.0094>, doi:10.1098/rspa.1929.0094.
URL <https://royalsocietypublishing.org/doi/abs/10.1098/rspa.1929.0094>
- [4] P. Coleman, *Introduction to Many-Body Physics*, Cambridge University Press, 2015. doi:10.1017/CB09781139020916.
- [5] P. Hohenberg, W. Kohn, Inhomogeneous electron gas, *Physical Review* 136 (3B) (1964). doi:10.1103/physrev.136.b864.

- [6] W. Kohn, L. J. Sham, Self-consistent equations including exchange and correlation effects, *Physical Review* 140 (4A) (1965). doi:10.1103/physrev.140.a1133.
- [7] A. Georges, G. Kotliar, W. Krauth, M. J. Rozenberg, Dynamical mean-field theory of strongly correlated fermion systems and the limit of infinite dimensions, *Reviews of Modern Physics* 68 (1) (1996) 13–125. doi:10.1103/RevModPhys.68.13.
URL <https://link.aps.org/doi/10.1103/RevModPhys.68.13>
- [8] R. T. Scalettar (2016). [link].
URL <https://www.cond-mat.de/events/correl16/manuscripts/scalettar.pdf>
- [9] S. Yamada, T. Imamura, M. Machida, High performance lobpcg method for solving multiple eigenvalues of hubbard model: Efficiency of communication avoiding neumann expansion preconditioner, in: R. Yokota, W. Wu (Eds.), *Supercomputing Frontiers*, Springer International Publishing, Cham, 2018, pp. 243–256.
- [10] J. M. Tomczak, S. Biermann, Optical Properties of Correlated Materials – or Why Intelligent Windows may look Dirty, *physica status solidi (b)* 246 (9) (2009) 1996–2005, arXiv: 0907.1575. doi:10.1002/pssb.200945231.
URL <http://arxiv.org/abs/0907.1575>
- [11] M. Qin, T. Schäfer, S. Andergassen, P. Corboz, E. Gull, The hubbard model: A computational perspective, *Annual Review of Condensed Matter Physics* 13 (1) (2022) 275–302. doi:10.1146/annurev-conmatphys-090921-033948.
- [12] G. Kotliar, D. Vollhardt, Strongly Correlated Materials: Insights From Dynamical Mean-Field Theory, *Physics Today* 57 (3) (2004) 53–59. arXiv:<https://pubs.aip.org/physicstoday/article-pdf/57/3/53/11004005/53\1\online.pdf>, doi:10.1063/1.1712502.
URL <https://doi.org/10.1063/1.1712502>
- [13] A. Damascelli, Probing the electronic structure of complex systems by arpes, *Physica Scripta* 2004 (T109) (2004) 61. doi:10.1238/Physica.Topical.109a00061.
URL <https://dx.doi.org/10.1238/Physica.Topical.109a00061>
- [14] H. Bruus, K. Flensberg, *Many-body quantum theory in Condensed matter physics: An introduction*, Oxford University Press, 2020.
- [15] G. Kotliar, D. Vollhardt, Strongly Correlated Materials: Insights From Dynamical Mean-Field Theory, *Physics Today* 57 (3) (2004) 53–59. arXiv:<https://pubs.aip.org/physicstoday/article-pdf/57/3/53/11004005/53\1\online.pdf>, doi:10.1063/1.1712502.
URL <https://doi.org/10.1063/1.1712502>

- [16] J. Kondo, Resistance Minimum in Dilute Magnetic Alloys, *Progress of Theoretical Physics* 32 (1) (1964) 37–49. arXiv:<https://academic.oup.com/ptp/article-pdf/32/1/37/5193092/32-1-37.pdf>, doi:10.1143/PTP.32.37. URL <https://doi.org/10.1143/PTP.32.37>
- [17] L. Kouwenhoven, L. Glazman, Revival of the kondo effect, *Physics World* 14 (1) (2001) 33–38. doi:10.1088/2058-7058/14/1/28.
- [18] P. W. Anderson, Localized magnetic states in metals, *Physical Review* 124 (1) (1961) 41–53. doi:10.1103/physrev.124.41.
- [19] A. Georges, Strongly correlated electron materials: Dynamical mean-field theory and electronic structure (Mar 2004). URL <https://arxiv.org/abs/cond-mat/0403123>
- [20] M. Caffarel, W. Krauth, Exact diagonalization approach to correlated fermions in infinite dimensions: Mott transition and superconductivity, *Physical Review Letters* 72 (10) (1994) 1545–1548. doi:10.1103/PhysRevLett.72.1545. URL <https://link.aps.org/doi/10.1103/PhysRevLett.72.1545>
- [21] C. Lanczos, An iteration method for the solution of the eigenvalue problem of linear differential and integral operators, *Journal of research of the National Bureau of Standards* 45 (1950) 255–282. URL <https://api.semanticscholar.org/CorpusID:478182>
- [22] S. Bi, L. Huang, N.-H. Tong, Natural Orbital-Based Lanczos Method for Anderson Impurity Models, *Computer Physics Communications* 235 (2019) 196–209, arXiv: 1802.02340. doi:10.1016/j.cpc.2018.09.002. URL <http://arxiv.org/abs/1802.02340>
- [23] E. Gull, A. J. Millis, A. I. Lichtenstein, A. N. Rubtsov, M. Troyer, P. Werner, Continuous-time monte-carlo methods for quantum impurity models, *Reviews of Modern Physics* 83 (2) (2011) 349–404. doi:10.1103/revmodphys.83.349.
- [24] K. G. Wilson, The renormalization group: Critical phenomena and the kondo problem, *Reviews of Modern Physics* 47 (4) (1975) 773–840. doi:10.1103/revmodphys.47.773.
- [25] G. Kotliar, S. Y. Savrasov, G. Pálsson, G. Biroli, Cellular Dynamical Mean Field Approach to Strongly Correlated Systems, *Physical Review Letters* 87 (18) (2001) 186401. doi:10.1103/PhysRevLett.87.186401. URL <https://link.aps.org/doi/10.1103/PhysRevLett.87.186401>
- [26] M. H. Hettler, M. Mukherjee, M. Jarrell, H. R. Krishnamurthy, Dynamical cluster approximation: Nonlocal dynamics of correlated electron systems, *Physical Review B* 61 (19) (2000) 12739–12756. doi:10.1103/physrevb.61.12739.
- [27] T. Maier, M. Jarrell, T. Pruschke, M. H. Hettler, Quantum cluster theories, *Reviews of Modern Physics* 77 (3) (2005) 1027–1080. doi:10.1103/revmodphys.77.1027.

- [28] B. Bauer, D. Wecker, A. J. Millis, M. B. Hastings, M. Troyer, Hybrid quantum-classical approach to correlated materials, *Physical Review X* 6 (3) (2016) 031045, arXiv: 1510.03859. doi:10.1103/PhysRevX.6.031045.
URL <http://arxiv.org/abs/1510.03859>
- [29] J. M. Kreula, L. García-Álvarez, L. Lamata, S. R. Clark, E. Solano, D. Jaksch, Few-qubit quantum-classical simulation of strongly correlated lattice fermions, *EPJ Quantum Technology* 3 (1) (2016). doi:10.1140/epjqt/s40507-016-0049-1.
- [30] T. Ayrál, T.-H. Lee, G. Kotliar, Dynamical Mean Field Theory, Density-Matrix Embedding Theory and Rotationally Invariant Slave Bosons: a Unified Perspective, *Physical Review B* 96 (23) (2017) 235139, arXiv: 1710.07773. doi:10.1103/PhysRevB.96.235139.
URL <http://arxiv.org/abs/1710.07773>
- [31] F. Lechermann, A. Georges, G. Kotliar, O. Parcollet, Rotationally-invariant slave-boson formalism and momentum dependence of the quasiparticle weight, *Physical Review B* 76 (15) (2007) 155102, arXiv: 0704.1434. doi:10.1103/PhysRevB.76.155102.
URL <http://arxiv.org/abs/0704.1434>
- [32] T.-H. Lee, T. Ayrál, Y.-X. Yao, N. Lanata, G. Kotliar, Rotationally invariant slave-boson and density matrix embedding theory: A unified framework and a comparative study on the 1D and 2D Hubbard Model, *Physical Review B* 99 (11) (2019) 115129, arXiv: 1812.09820. doi:10.1103/PhysRevB.99.115129.
URL <http://arxiv.org/abs/1812.09820>
- [33] G. Kotliar, A. E. Ruckenstein, New Functional Integral Approach to Strongly Correlated Fermi Systems: The Gutzwiller Approximation as a Saddle Point, *Physical Review Letters* 57 (11) (1986) 1362–1365. doi:10.1103/PhysRevLett.57.1362.
URL <https://link.aps.org/doi/10.1103/PhysRevLett.57.1362>
- [34] J. Hubbard, Calculation of partition functions, *Physical Review Letters* 3 (2) (1959) 77–78. doi:10.1103/physrevlett.3.77.
- [35] N. Lanatà, Y. Yao, C.-Z. Wang, K.-M. Ho, G. Kotliar, Phase Diagram and Electronic Structure of Praseodymium and Plutonium, *Physical Review X* 5 (1) (2015) 011008. doi:10.1103/PhysRevX.5.011008.
URL <https://link.aps.org/doi/10.1103/PhysRevX.5.011008>
- [36] S. Aaronson, Np-complete problems and physical reality (2005). arXiv: quant-ph/0502072.
- [37] R. P. Feynman, Simulating physics with computers, *International Journal of Theoretical Physics* 21 (6–7) (1982) 467–488. doi:10.1007/bf02650179.

- [38] J. Preskill, Quantum Computing in the NISQ era and beyond, *Quantum* 2 (2018) 79, arXiv: 1801.00862. doi:10.22331/q-2018-08-06-79.
URL <http://arxiv.org/abs/1801.00862>
- [39] D. P. DiVincenzo, IBM, The Physical Implementation of Quantum Computation, *Fortschritte der Physik* 48 (9-11) (2000) 771–783, arXiv:quant-ph/0002077. doi:10.1002/1521-3978(200009)48:9/11<771::AID-PROP771>3.0.CO;2-E.
URL <http://arxiv.org/abs/quant-ph/0002077>
- [40] A. Browaeys, T. Lahaye, *Many-body physics with individually controlled Rydberg atoms*, *Nat. Phys.* 16 (2020) 132. doi:10.1038/s41567-019-0733-z.
- [41] L. Henriët, L. Beguin, A. Signoles, T. Lahaye, A. Browaeys, G.-O. Reymond, C. Jurczak, *Quantum computing with neutral atoms*, *Quantum* 4 (2020) 327. arXiv:2006.12326, doi:10.22331/q-2020-09-21-327.
- [42] B. Foxen, C. Neill, A. Dunsworth, P. Roushan, B. Chiaro, A. Megrant, J. Kelly, Z. Chen, K. Satzinger, R. Barends, F. Arute, K. Arya, R. Babbush, D. Bacon, J. C. Bardin, S. Boixo, D. Buell, B. Burkett, Y. Chen, R. Collins, E. Farhi, A. Fowler, C. Gidney, M. Giustina, R. Graff, M. Harrigan, T. Huang, S. V. Isakov, E. Jeffrey, Z. Jiang, D. Kafri, K. Kechedzhi, P. Klimov, A. Korotkov, F. Kostritsa, D. Landhuis, E. Lucero, J. McClean, M. McEwen, X. Mi, M. Mohseni, J. Y. Mutus, O. Naaman, M. Neeley, M. Niu, A. Petukhov, C. Quintana, N. Rubin, D. Sank, V. Smelyanskiy, A. Vainsencher, T. C. White, Z. Yao, P. Yeh, A. Zalcman, H. Neven, J. M. Martinis, Demonstrating a continuous set of two-qubit gates for near-term quantum algorithms, *Phys. Rev. Lett.* 125 (2020) 120504. doi:10.1103/PhysRevLett.125.120504.
URL <https://link.aps.org/doi/10.1103/PhysRevLett.125.120504>
- [43] P. Jordan, E. Wigner, *Über das Paulische Äquivalenzverbot*, *Z. Physik* 47 (1928) 631. doi:10.1007/BF01331938.
- [44] S. B. Bravyi, A. Y. Kitaev, *Fermionic quantum computation*, *Ann. Phys.* 298 (2002) 210. doi:10.1006/aphy.2002.6254.
- [45] J. T. Seeley, M. J. Richard, P. J. Love, *The Bravyi-Kitaev transformation for quantum computation of electronic structure*, *J. Chem. Phys.* 137 (2012) 224109. doi:10.1063/1.4768229.
- [46] T. Ayrál, P. Besserve, D. Lacroix, E. A. R. Guzman, Quantum computing with and for many-body physics (Mar 2023).
URL <https://arxiv.org/abs/2303.04850>
- [47] A. Peruzzo, J. McClean, P. Shadbolt, M.-H. Yung, X.-Q. Zhou, P. J. Love, A. Aspuru-Guzik, J. L. O’Brien, A variational eigenvalue solver on a photonic quantum processor, *Nature Communications* 5 (1) (2014) 4213, number: 1 Publisher: Nature Publishing Group. doi:10.1038/ncomms5213.
URL <https://www.nature.com/articles/ncomms5213>

- [48] J. R. McClean, S. Boixo, V. N. Smelyanskiy, R. Babbush, H. Neven, Barren plateaus in quantum neural network training landscapes, *Nature Communications* 9 (1) (2018) 4812, arXiv: 1803.11173. doi:10.1038/s41467-018-07090-4.
URL <http://arxiv.org/abs/1803.11173>
- [49] J. Romero, R. Babbush, J. R. McClean, C. Hempel, P. J. Love, A. Aspuru-Guzik, *Strategies for quantum computing molecular energies using the unitary coupled cluster ansatz*, *Quantum Sci. Technol.* 4 (2018) 014008. doi:10.1088/2058-9565/aad3e4.
- [50] P.-L. Dallaire-Demers, J. Romero, L. Veis, S. Sim, A. Aspuru-Guzik, Low-depth circuit ansatz for preparing correlated fermionic states on a quantum computer, *Quantum Science and Technology* 4 (4) (2019) 045005, publisher: IOP Publishing. doi:10.1088/2058-9565/ab3951.
URL <https://doi.org/10.1088/2058-9565/ab3951>
- [51] K. Mitarai, M. Negoro, M. Kitagawa, K. Fujii, Quantum circuit learning, *Physical Review A* (Sep 2018).
URL <https://journals.aps.org/prabstract/10.1103/PhysRevA.98.032309>
- [52] M. J. Powell, A direct search optimization method that models the objective and constraint functions by linear interpolation, *Advances in Optimization and Numerical Analysis* (1994) 51–67doi:10.1007/978-94-015-8330-5_4.
- [53] J. Nocedal, S. J. Wright, *Numerical optimization*, Springer, 2006.
- [54] J. A. Nelder, R. Mead, A Simplex Method for Function Minimization, *The Computer Journal* 7 (4) (1965) 308–313. arXiv:<https://academic.oup.com/comjnl/article-pdf/7/4/308/1013182/7-4-308.pdf>, doi:10.1093/comjnl/7.4.308.
URL <https://doi.org/10.1093/comjnl/7.4.308>
- [55] M. Ostaszewski, E. Grant, M. Benedetti, Structure optimization for parameterized quantum circuits, *Quantum* 5 (2021) 391, publisher: Verein zur Förderung des Open Access Publizierens in den Quantenwissenschaften. doi:10.22331/q-2021-01-28-391.
URL <https://quantum-journal.org/papers/q-2021-01-28-391/>
- [56] S. Lloyd, Universal Quantum Simulators, *Science* 273 (5278) (1996) 1073–1078, eprint: <https://www.science.org/doi/pdf/10.1126/science.273.5278.1073>. doi:10.1126/science.273.5278.1073.
URL <https://www.science.org/doi/abs/10.1126/science.273.5278.1073>
- [57] D. W. Berry, G. Ahokas, R. Cleve, B. C. Sanders, *Efficient quantum algorithms for simulating sparse Hamiltonians*, *Commun. Math. Phys.* 270 (2006) 359. doi:10.1007/s00220-006-0150-x.

- [58] M. A. Nielsen, I. L. Chuang, *Quantum computation and quantum information*, 2010. doi:10.1017/CB09780511976667.
- [59] E. Magesan, J. M. Gambetta, J. Emerson, Characterizing quantum gates via randomized benchmarking, *Physical Review A* 85 (4) (2012) 042311. doi: 10.1103/PhysRevA.85.042311.
URL <https://link.aps.org/doi/10.1103/PhysRevA.85.042311>
- [60] S. Martiel, T. G. de Brugière, Architecture aware compilation of quantum circuits via lazy synthesis, arXiv:2012.09663 [quant-ph]ArXiv: 2012.09663 (Dec. 2020).
URL <http://arxiv.org/abs/2012.09663>
- [61] P. Czarnik, A. Arrasmith, P. J. Coles, L. Cincio, Error mitigation with Clifford quantum-circuit data, arXiv:2005.10189 [quant-ph]ArXiv: 2005.10189 (Feb. 2021).
URL <http://arxiv.org/abs/2005.10189>
- [62] A. He, B. Nachman, W. A. de Jong, C. W. Bauer, Zero-noise extrapolation for quantum-gate error mitigation with identity insertions, *Physical Review A* 102 (1) (2020) 012426, publisher: American Physical Society. doi:10.1103/PhysRevA.102.012426.
URL <https://link.aps.org/doi/10.1103/PhysRevA.102.012426>
- [63] A. Kandala, K. Temme, A. D. Córcoles, A. Mezzacapo, J. M. Chow, J. M. Gambetta, Error mitigation extends the computational reach of a noisy quantum processor, *Nature* 567 (7749) (2019) 491–495, number: 7749 Publisher: Nature Publishing Group. doi:10.1038/s41586-019-1040-7.
URL <https://www.nature.com/articles/s41586-019-1040-7>
- [64] I. Rungger, N. Fitzpatrick, H. Chen, C. H. Alderete, H. Apel, A. Cowtan, A. Patterson, D. M. Ramo, Y. Zhu, N. H. Nguyen, E. Grant, S. Chretien, L. Wossnig, N. M. Linke, R. Duncan, Dynamical mean field theory algorithm and experiment on quantum computers, arXiv:1910.04735 [cond-mat, physics:quant-ph]ArXiv: 1910.04735 (Jan. 2020).
URL <http://arxiv.org/abs/1910.04735>
- [65] T. Keen, T. Maier, S. Johnston, P. Lougovski, Quantum-classical simulation of two-site dynamical mean-field theory on noisy quantum hardware, *Quantum Science and Technology* 5 (3) (2020) 035001. doi:10.1088/2058-9565/ab7d4c.
URL <https://iopscience.iop.org/article/10.1088/2058-9565/ab7d4c>
- [66] B. Jaderberg, A. Agarwal, K. Leonhardt, M. Kiffner, D. Jaksch, Minimum Hardware Requirements for Hybrid Quantum-Classical DMFT, *Quantum Science and Technology* 5 (3) (2020) 034015, arXiv: 2002.04612. doi: 10.1088/2058-9565/ab972b.
URL <http://arxiv.org/abs/2002.04612>

- [67] Y. Yao, F. Zhang, C.-Z. Wang, K.-M. Ho, P. P. Orth, Gutzwiller hybrid quantum-classical computing approach for correlated materials, *Physical Review Research* 3 (1) (2021) 013184. doi:10.1103/PhysRevResearch.3.013184.
URL <https://link.aps.org/doi/10.1103/PhysRevResearch.3.013184>
- [68] C. M. Goringe, D. R. Bowler, E. Hernández, Tight-binding modelling of materials, *Reports on Progress in Physics* 60 (12) (1997) 1447–1512. doi:10.1088/0034-4885/60/12/001.
- [69] G. H. Wannier, The structure of electronic excitation levels in insulating crystals, *Physical Review* 52 (3) (1937) 191–197. doi:10.1103/physrev.52.191.
- [70] D. J. Thouless, Stability conditions and nuclear rotations in the Hartree-Fock theory, *Nuclear Physics* 21 (1960) 225–232. doi:10.1016/0029-5582(60)90048-1.
URL <http://www.sciencedirect.com/science/article/pii/0029558260900481>
- [71] I. O. Sokolov, P. K. Barkoutsos, P. J. Ollitrault, D. Greenberg, J. Rice, M. Pistoia, I. Tavernelli, Quantum Orbital-Optimized Unitary Coupled Cluster Methods in the Strongly Correlated Regime: Can Quantum Algorithms Outperform their Classical Equivalents?, *The Journal of Chemical Physics* 152 (12) (2020) 124107, arXiv: 1911.10864. doi:10.1063/1.5141835.
URL <http://arxiv.org/abs/1911.10864>
- [72] W. Mizukami, K. Mitarai, Y. O. Nakagawa, T. Yamamoto, T. Yan, Y.-y. Ohnishi, Orbital optimized unitary coupled cluster theory for quantum computer, *Physical Review Research* 2 (3) (2020) 033421, arXiv: 1910.11526. doi:10.1103/PhysRevResearch.2.033421.
URL <http://arxiv.org/abs/1910.11526>
- [73] C. E. P. Robin, M. J. Savage, Quantum Simulations in Effective Model Spaces (I): Hamiltonian Learning-VQE using Digital Quantum Computers and Application to the Lipkin-Meshkov-Glick Model, *Tech. Rep.* arXiv:2301.05976, arXiv, arXiv:2301.05976 [nucl-th, physics:quant-ph] (Jan. 2023).
URL <http://arxiv.org/abs/2301.05976>
- [74] J. R. Moreno, J. Cohn, D. Sels, M. Motta, Enhancing the expressivity of variational neural, and hardware-efficient quantum states through orbital rotations (Feb 2023).
URL <https://arxiv.org/abs/2302.11588>
- [75] P.-O. Löwdin, Quantum Theory of Many-Particle Systems. I. Physical Interpretations by Means of Density Matrices, Natural Spin-Orbitals, and Convergence Problems in the Method of Configurational Interaction, *Physical Review* 97 (6) (1955) 1474–1489. doi:10.1103/PhysRev.97.1474.
URL <https://link.aps.org/doi/10.1103/PhysRev.97.1474>

- [76] I. Schur, Über eine klasse von mittelbildungen mit anwendungen die determinanten—theorie, Sitzungsber. Berlin. Math. Gesellschaft 22 (1923).
- [77] P.-O. Löwdin, H. Shull, Natural orbitals in the quantum theory of two-electron systems, Physical Review Journals Archive (Mar 1956).
URL <https://link.aps.org/doi/10.1103/PhysRev.101.1730>
- [78] A. J. Ferris, Fourier transform for fermionic systems and the spectral tensor network, Physical Review Letters (Jul 2014).
URL <https://journals.aps.org/prl/abstract/10.1103/PhysRevLett.113.010401>
- [79] R.-Q. He, Z.-Y. Lu, Quantum Renormalization Groups Based on Natural Orbitals, Physical Review B 89 (8) (2014) 085108, arXiv:1306.3662 [cond-mat, physics:physics, physics:quant-ph]. doi:10.1103/PhysRevB.89.085108.
URL <http://arxiv.org/abs/1306.3662>
- [80] W. Kutzelnigg, J. Smith, Vedene H., On Different Criteria for the Best Independent-Particle Model Approximation, The Journal of Chemical Physics 41 (3) (2004) 896–897. arXiv:https://pubs.aip.org/aip/jcp/article-pdf/41/3/896/11095559/896\1\1_online.pdf, doi:10.1063/1.1725981.
URL <https://doi.org/10.1063/1.1725981>
- [81] F. Arute, K. Arya, R. Babbush, D. Bacon, J. C. Bardin, R. Barends, S. Boixo, M. Broughton, B. B. Buckley, D. A. Buell, B. Burkett, N. Bushnell, Y. Chen, Z. Chen, B. Chiaro, R. Collins, W. Courtney, S. Demura, A. Dunsworth, E. Farhi, A. Fowler, B. Foxen, C. Gidney, M. Giustina, R. Graff, S. Habegger, M. P. Harrigan, A. Ho, S. Hong, T. Huang, W. J. Huggins, L. Ioffe, S. V. Isakov, E. Jeffrey, Z. Jiang, C. Jones, D. Kafri, K. Kechedzhi, J. Kelly, S. Kim, P. V. Klimov, A. Korotkov, F. Kostritsa, D. Landhuis, P. Laptev, M. Lindmark, E. Lucero, O. Martin, J. M. Martinis, J. R. McClean, M. McEwen, A. Megrant, X. Mi, M. Mohseni, W. Mroczkiewicz, J. Mutus, O. Naaman, M. Neeley, C. Neill, H. Neven, M. Y. Niu, T. E. O’Brien, E. Ostby, A. Petukhov, H. Putterman, C. Quintana, P. Roushan, N. C. Rubin, D. Sank, K. J. Satzinger, V. Smelyanskiy, D. Strain, K. J. Sung, M. Szalay, T. Y. Takeshita, A. Vainsencher, T. White, N. Wiebe, Z. J. Yao, P. Yeh, A. Zalcman, Hartree-Fock on a superconducting qubit quantum computer, arXiv:2004.04174 [physics, physics:quant-ph]ArXiv: 2004.04174 (Apr. 2020).
URL <http://arxiv.org/abs/2004.04174>
- [82] A. A. Klyachko, Quantum marginal problem and N-representability, Journal of Physics: Conference Series 36 (2006) 72–86. doi:10.1088/1742-6596/36/1/014.
URL <https://iopscience.iop.org/article/10.1088/1742-6596/36/1/014>
- [83] Y. Lu, X. Cao, P. Hansmann, M. W. Haverkort, Natural-Orbital Impurity Solver and Projection Approach for Green’s Function, Physical Review B

- 100 (11) (2019) 115134, arXiv: 1909.02757. doi:10.1103/PhysRevB.100.115134.
 URL <http://arxiv.org/abs/1909.02757>
- [84] C. L. Benavides-Riveros, C. Schilling, Natural Extension of Hartree-Fock through extremal $\mathbb{1}$ -fermion information: Overview and application to the lithium atom, *Zeitschrift für Physikalische Chemie* 230 (5-7) (2016) 703–717, arXiv:1711.09129 [cond-mat, physics:quant-ph]. doi:10.1515/zpch-2015-0732.
 URL <http://arxiv.org/abs/1711.09129>
- [85] C. Schilling, C. L. Benavides-Riveros, A. Lopes, T. Maciażek, A. Sawicki, Implications of pinned occupation numbers for natural orbital expansions: I. Generalizing the concept of active spaces, *New Journal of Physics* 22 (2) (2020) 023001, publisher: IOP Publishing. doi:10.1088/1367-2630/ab64b0.
 URL <https://dx.doi.org/10.1088/1367-2630/ab64b0>
- [86] D. R. Alcoba, A. Torre, L. Lain, G. E. Massaccesi, O. B. Oña, Seniority number in spin-adapted spaces and compactness of configuration interaction wave functions, *The Journal of Chemical Physics* 139 (8) (2013) 084103. doi:10.1063/1.4818755.
 URL <http://aip.scitation.org/doi/10.1063/1.4818755>
- [87] J. R. Moreno, J. Cohn, D. Sels, M. Motta, Enhancing the Expressivity of Variational Neural, and Hardware-Efficient Quantum States Through Orbital Rotations, Tech. Rep. arXiv:2302.11588, arXiv, arXiv:2302.11588 [cond-mat, physics:quant-ph] (Feb. 2023).
 URL <http://arxiv.org/abs/2302.11588>
- [88] E. Koridon, S. Yalouz, B. Senjean, F. Buda, T. E. O’Brien, L. Visscher, Orbital transformations to reduce the 1-norm of the electronic structure Hamiltonian for quantum computing applications, arXiv:2103.14753 [quant-ph]ArXiv: 2103.14753 (Oct. 2021). doi:10.1103/PhysRevResearch.3.033127.
 URL <http://arxiv.org/abs/2103.14753>
- [89] D. Wecker, M. B. Hastings, M. Troyer, Towards Practical Quantum Variational Algorithms, *Physical Review A* 92 (4) (2015) 042303, arXiv: 1507.08969. doi:10.1103/PhysRevA.92.042303.
 URL <http://arxiv.org/abs/1507.08969>
- [90] W. Dobrutz, H. Luo, A. Alavi, Compact numerical solutions to the two-dimensional repulsive hubbard model obtained via nonunitary similarity transformations, *Phys. Rev. B* 99 (2019) 075119. doi:10.1103/PhysRevB.99.075119.
 URL <https://link.aps.org/doi/10.1103/PhysRevB.99.075119>
- [91] I. O. Sokolov, W. Dobrutz, H. Luo, A. Alavi, I. Tavernelli, Orders of magnitude increased accuracy for quantum many-body problems on quantum computers via an exact transcorrelated method, *Phys. Rev. Res.* 5 (2023) 023174.

doi:10.1103/PhysRevResearch.5.023174.

URL <https://link.aps.org/doi/10.1103/PhysRevResearch.5.023174>

- [92] E. Pavarini, E. Koch, S. Zhang (Eds.), Many-Body Methods for Real Materials, Vol. 9 of Schriften des Forschungszentrums Jülich. Modeling and Simulation, Autumn School on Correlated Electrons, Jülich (Germany), 16 Sep 2019 - 20 Sep 2019, Forschungszentrum Jülich GmbH Zentralbibliothek, Verlag, Jülich, 2019.
URL <https://juser.fz-juelich.de/record/864818>
- [93] K. Sugisaki, S. Nakazawa, K. Toyota, K. Sato, D. Shiomi, T. Takui, Quantum Chemistry on Quantum Computers: A Method for Preparation of Multiconfigurational Wave Functions on Quantum Computers without Performing Post-Hartree-Fock Calculations, ACS Central Science 5 (1) (2019) 167–175. doi:10.1021/acscentsci.8b00788.
URL <https://pubs.acs.org/doi/10.1021/acscentsci.8b00788>
- [94] T. Steckmann, T. Keen, A. F. Kemper, E. F. Dumitrescu, Y. Wang, Simulating the Mott transition on a noisy digital quantum computer via Cartan-based fast-forwarding circuits, arXiv:2112.05688 [cond-mat, physics:quant-ph]ArXiv: 2112.05688 (Dec. 2021).
URL <http://arxiv.org/abs/2112.05688>
- [95] D. E. R. Bender, C. F., A natural orbital based energy calculation for helium hydride and lithium hydride, J. Phys. Chem. 70 (1966) 2675–2685. doi: 10.1021/j100880a036.
- [96] N. V. Tkachenko, J. Sud, Y. Zhang, S. Tretiak, P. M. Anisimov, A. T. Arrasmith, P. J. Coles, L. Cincio, P. A. Dub, Correlation-Informed Permutation of Qubits for Reducing Ansatz Depth in the Variational Quantum Eigensolver, PRX Quantum 2 (2) (2021) 020337, publisher: American Physical Society. doi:10.1103/PRXQuantum.2.020337.
URL <https://link.aps.org/doi/10.1103/PRXQuantum.2.020337>
- [97] P. Besserve, T. Ayrál, Unraveling correlated material properties with noisy quantum computers: Natural orbitalized variational quantum eigensolving of extended impurity models within a slave-boson approach, Physical Review B 105 (11) (2022) 115108, publisher: American Physical Society. doi:10.1103/PhysRevB.105.115108.
URL <https://link.aps.org/doi/10.1103/PhysRevB.105.115108>
- [98] H. R. Grimsley, S. E. Economou, E. Barnes, N. J. Mayhall, An adaptive variational algorithm for exact molecular simulations on a quantum computer, Nature Communications 10 (1) (2019) 3007, arXiv: 1812.11173. doi:10.1038/s41467-019-10988-2.
URL <http://arxiv.org/abs/1812.11173>
- [99] P. K. Barkoutsos, J. F. Gonthier, I. Sokolov, N. Moll, G. Salis, A. Fuhrer, M. Ganzhorn, D. J. Egger, M. Troyer, A. Mezzacapo, S. Filipp, I. Tavernelli,

- Quantum algorithms for electronic structure calculations: particle/hole Hamiltonian and optimized wavefunction expansions, *Physical Review A* 98 (2) (2018) 022322, arXiv:1805.04340 [quant-ph]. doi:10.1103/PhysRevA.98.022322.
URL <http://arxiv.org/abs/1805.04340>
- [100] H. L. Tang, V. Shkolnikov, G. S. Barron, H. R. Grimsley, N. J. Mayhall, E. Barnes, S. E. Economou, Qubit-ADAPT-VQE: An Adaptive Algorithm for Constructing Hardware-Efficient Ansätze on a Quantum Processor, *PRX Quantum* 2 (2) (2021) 020310. doi:10.1103/PRXQuantum.2.020310.
URL <https://link.aps.org/doi/10.1103/PRXQuantum.2.020310>
- [101] Y. S. Yordanov, V. Armaos, C. H. W. Barnes, D. R. M. Arvidsson-Shukur, Qubit-excitation-based adaptive variational quantum eigensolver, *Nature News* (Oct 2021).
URL <https://www.nature.com/articles/s42005-021-00730-0#citeas>
- [102] A. Dorda, M. Nuss, W. von der Linden, E. Arrigoni, Auxiliary master equation approach to non-equilibrium correlated impurities, *Physical Review B* 89 (16) (2014) 165105, arXiv:1312.4586 [cond-mat, physics:quant-ph]. doi:10.1103/PhysRevB.89.165105.
URL <http://arxiv.org/abs/1312.4586>
- [103] A. Dorda, M. E. Sorantin, W. von der Linden, E. Arrigoni, Optimized auxiliary representation of a non-Markovian environment by a Lindblad equation, *New Journal of Physics* 19 (6) (2017) 063005, arXiv:1608.04632 [cond-mat, physics:quant-ph]. doi:10.1088/1367-2630/aa6ccc.
URL <http://arxiv.org/abs/1608.04632>
- [104] F. Schwarz, M. Goldstein, A. Dorda, E. Arrigoni, A. Weichselbaum, J. von Delft, Lindblad-Driven Discretized Leads for Non-Equilibrium Steady-State Transport in Quantum Impurity Models: Recovering the Continuum Limit, *Physical Review B* 94 (15) (2016) 155142, arXiv:1604.02050 [cond-mat]. doi:10.1103/PhysRevB.94.155142.
URL <http://arxiv.org/abs/1604.02050>
- [105] N. Koukoulekidis, S. Wang, T. O’Leary, D. Bultrini, L. Cincio, P. Czarnik, A framework of partial error correction for intermediate-scale quantum computers (Jun 2023).
URL <https://arxiv.org/abs/2306.15531>
- [106] L. V. Keldysh, Diagram technique for nonequilibrium processes, *Sov. Phys. JETP* 20 (1965) 1018, [*Zh. Eksp. Theor. Fiz.* **47**, 1515 (1964)].
- [107] J. Schwinger, Brownian Motion of a Quantum Oscillator, *Journal of Mathematical Physics* 2 (3) (2004) 407–432. arXiv:https://pubs.aip.org/aip/jmp/article-pdf/2/3/407/11355292/407_1_online.pdf, doi:10.1063/1.1703727.
URL <https://doi.org/10.1063/1.1703727>

- [108] G. Stefanucci, R. v. Leeuwen, Nonequilibrium many-body theory of quantum systems a modern introduction, Cambridge University Press, 2013.
- [109] M. Lax, Formal theory of quantum fluctuations from a driven state, *Phys. Rev.* 129 (1963) 2342–2348. doi:10.1103/PhysRev.129.2342.
URL <https://link.aps.org/doi/10.1103/PhysRev.129.2342>
- [110] H. Aoki, N. Tsuji, M. Eckstein, M. Kollar, T. Oka, P. Werner, Nonequilibrium dynamical mean-field theory and its applications, *Reviews of Modern Physics* 86 (2) (2014) 779–837, arXiv: 1310.5329. doi:10.1103/RevModPhys.86.779.
URL <http://arxiv.org/abs/1310.5329>
- [111] D. González-Cuadra, D. Bluvstein, M. Kalinowski, R. Kaubruegger, N. Maskara, P. Naldesi, T. V. Zache, A. M. Kaufman, M. D. Lukin, H. Pichler, B. Vermersch, J. Ye, P. Zoller, Fermionic quantum processing with programmable neutral atom arrays, arXiv:2303.06985 [cond-mat, physics:hep-lat, physics:quant-ph] (Mar. 2023).
URL <http://arxiv.org/abs/2303.06985>
- [112] J. P. T. Stenger, G. Ben-Shach, D. Pekker, N. T. Bronn, Simulating spectroscopy experiments with a superconducting quantum computer, *Tech. Rep.* arXiv:2202.12910, arXiv, arXiv:2202.12910 [cond-mat, physics:quant-ph] (Jul. 2022).
URL <http://arxiv.org/abs/2202.12910>
- [113] A. Pocklington, Y.-X. Wang, Y. Yanay, A. A. Clerk, Stabilizing volume-law entangled states of fermions and qubits using local dissipation, *Physical Review B* 105 (14) (2022) L140301, arXiv:2107.14121 [cond-mat, physics:quant-ph]. doi:10.1103/PhysRevB.105.L140301.
URL <http://arxiv.org/abs/2107.14121>
- [114] J. W. Negele, H. Orland, Quantum many-particle systems, Perseus Books, 1998.
- [115] T. Baumgratz, M. Cramer, M. B. Plenio, Quantifying Coherence, *Physical Review Letters* 113 (14) (2014) 140401, arXiv: 1311.0275. doi:10.1103/PhysRevLett.113.140401.
URL <http://arxiv.org/abs/1311.0275>
- [116] N. Lanatà, H. U. R. Strand, X. Dai, B. Hellsing, Efficient implementation of the Gutzwiller variational method, *Physical Review B* 85 (3) (2012) 035133, arXiv: 1108.0180. doi:10.1103/PhysRevB.85.035133.
URL <http://arxiv.org/abs/1108.0180>
- [117] J. Kleinhenz, Nonequilibrium dynamics of strongly correlated systems (2021). doi:10.7302/2859.
URL <http://deepblue.lib.umich.edu/handle/2027.42/169814>

Titre : Algorithmes hybrides quantiques-classiques pour le problème à N corps quantique

Mots clés : matériaux corrélés, ordinateur quantique, théorie du champ moyen dynamique, bruit quantique

Résumé : Les matériaux à fortes corrélations présentent des phases électroniques à haut potentiel applicatif, telles que la supraconductivité à haute température critique. Néanmoins, ces systèmes sont notoirement difficiles à décrire car ils échappent aux méthodes de champ moyen standard.

Cette thèse étudie l'apport du calcul quantique bruité pour l'algorithme phare des fortes corrélations, la théorie du champ moyen dynamique (DMFT). Elle vise à mettre à profit les premiers dispositifs de calcul quantique, malgré leurs imperfections liées à un degré de contrôle expérimental encore limité.

Dans un premier temps, une version améliorée de la méthode variationnelle de préparation de l'état fondamental du modèle d'impureté est proposée. Elle consiste en la réalisation de mises à jour de la base à une particule dans laquelle est décrit le Hamiltonien d'impureté. Ces mises à jour sont entrelacées avec des optimisations variationnelles de l'état, et guidées par la matrice densité à une particule de l'état variationnel optimisé courant. Cet algorithme nous a

permis de réaliser la première implémentation hybride bruitée d'un schéma assimilé à la DMFT avec un système auxiliaire à deux impuretés. Aussi, nous montrons sur plusieurs exemples que cette méthode est capable d'augmenter la capacité d'un circuit variationnel donné à représenter l'état cible. Enfin, nous proposons de combiner les mises à jour de la base à une particule avec un algorithme variationnel dit adaptatif, qui construit le circuit itérativement. Nous montrons que cette approche permet de réduire, à précision donnée sur l'énergie de l'état optimisé, le nombre de portes du circuit.

Dans un second temps, nous proposons de mettre à profit la dissipation qui affecte les qubits afin de diminuer les effets de la troncation du bain sur l'ajustement de l'hybridation du bain à celle de la DMFT. Nous montrons qu'une réduction en termes de sites de bain est bien à portée d'une telle méthode. Cependant, nous faisons l'hypothèse d'un processus dissipatif qui n'est pas réaliste : la méthode doit donc encore être étudiée via un modèle plus proche des conditions expérimentales.

Title : Hybrid quantum-classical algorithms for the quantum many-body problem

Keywords : correlated materials, quantum computing, dynamical mean-field theory, quantum noise

Abstract : Strongly-correlated materials feature electronic phases with high potential for application, such as high-temperature superconductivity. Nevertheless, these systems are notoriously difficult to describe, as they escape standard mean-field methods.

This thesis investigates the possibility to leverage noisy quantum computation within the flagship algorithm for strong correlations, the dynamical mean-field theory (DMFT). It aims to take advantage of the first quantum computing devices, despite their imperfections imputable to a still-limited degree of experimental control.

Firstly, an improved version of the variational method for preparing the ground state of the impurity model is proposed. It consists in carrying out updates of the single-particle basis in which the impurity Hamiltonian is described. These updates are interwoven with variational optimizations of the state, and guided by the one-particle density matrix of the current op-

timized variational state. This algorithm has enabled us to carry out the first noisy hybrid implementation of a DMFT-like scheme with a two-impurity auxiliary system. Also, we show on several examples that this method is capable of increasing the ability of a given variational circuit to represent the target state. Finally, we propose to combine single-particle basis updates with an adaptive variational algorithm, which builds the circuit iteratively. We show that this approach can reduce the number of gates in the circuit for a given precision in the energy of the attained state.

Secondly, we propose to take advantage of the dissipation affecting the qubits to alleviate the effect of bath truncation onto the fit of the DMFT hybridization. We confirm that a reduction in the count of bath sites is within the reach of such a method. However, we make the assumption of a dissipative process which is not realistic: the method therefore still needs to be studied via a model closer to experimental conditions.